

Dottorato di Ricerca in Fisica - XIV ciclo (1998-2001)
Università degli studi di Milano
Dipartimento di Fisica

Dr. Tommaso Lari

DISSERTAZIONE

**Study of silicon pixel sensors for
the ATLAS Detector**

Il tutore

Prof. F. Ragusa

Il coordinatore

Prof. A. Pullia

Space...the final frontier. These are the voyages of the starship "Enterprise". Her ongoing mission: To explore strange, new worlds. To seek out new life forms, and new civilizations. To boldly go where no man has gone before.

Paramount Pictures, *Star Trek: the original series*

There are more things in heaven and earth, Horatio, than are dreamt of in your philosophy.

W. Shakespeare, *Hamlet*, Act I, Scene 5, line 166



Figure 1: Aerial view of CERN and the surrounding region (CERN photograph, reprinted with permission). The 3 rings show the underground position of the accelerators. The smaller one is the Proton Synchrotron (PS), the middle ring is the Super Proton Synchrotron (SPS) with a circumference of 7 km and the largest ring (27 km) is the tunnel which housed the Large Electron Positron collider (LEP) and which will also house the Large Hadron Collider (LHC). Part of the Lake Geneva is visible in the background.

Contents

| | | |
|----------|---|-----------|
| 1 | The ATLAS experiment | 5 |
| 1.1 | General overview | 5 |
| 1.1.1 | Physics motivations and goals | 5 |
| 1.1.2 | Overall detector concept | 6 |
| 1.1.3 | Reference system and definitions | 7 |
| 1.2 | The ATLAS physics programme | 7 |
| 1.2.1 | Standard Model physics | 8 |
| 1.2.2 | Standard Model Higgs boson | 9 |
| 1.2.3 | Supersymmetry | 10 |
| 1.2.4 | Other physics beyond the Standard model | 12 |
| 1.3 | The ATLAS detector | 13 |
| 1.3.1 | The Inner Detector | 13 |
| 1.3.2 | The calorimeters | 17 |
| 1.3.3 | The muon spectrometer | 19 |
| 1.3.4 | Trigger, data acquisition and computing | 19 |
| 2 | The Pixel detector | 21 |
| 2.1 | Basic features of silicon detectors | 21 |
| 2.2 | Radiation damage in silicon detectors | 22 |
| 2.3 | Layout | 26 |
| 2.4 | Modules | 28 |
| 2.5 | The sensor | 30 |
| 2.6 | The front-end electronics | 35 |
| 3 | Test Beam setup and tested devices | 40 |
| 3.1 | Test Beam setup | 40 |
| 3.2 | Data analysis and alignment | 44 |
| 3.3 | Tested devices | 45 |
| 4 | Efficiency and charge collection studies | 49 |
| 4.1 | Charge collection | 49 |
| 4.1.1 | Unirradiated sensors | 49 |
| 4.1.2 | Irradiated sensors | 52 |
| 4.2 | Efficiency | 56 |
| 5 | Measurement of depletion depth | 62 |
| 5.1 | Measurement procedure | 62 |
| 5.2 | Results | 67 |

| | | |
|----------|--|------------|
| 6 | A detailed study of Lorentz angle effects | 72 |
| 6.1 | The Lorentz angle | 72 |
| 6.2 | Measurement of magnetic field | 73 |
| 6.3 | Measurement of Lorentz angle | 75 |
| 6.4 | Interpretation of the measurements of Lorentz angle | 78 |
| 6.4.1 | Charge drift in silicon | 79 |
| 6.4.2 | The Lorentz effect | 83 |
| 6.4.3 | Signal induced on the pixels | 84 |
| 6.4.4 | Computation of the Lorentz angle in the test beam | 85 |
| 6.4.5 | Computation of Lorentz angle in ATLAS | 87 |
| 7 | Spatial resolution analysis | 89 |
| 7.1 | General consideration | 89 |
| 7.2 | Digital and analog reconstruction | 91 |
| 7.3 | Telescope resolution | 94 |
| 7.4 | x-spatial resolution at normal incidence | 97 |
| 7.5 | x-spatial resolution as a function of the angle of incidence | 99 |
| 7.5.1 | Digital resolution | 99 |
| 7.5.2 | Analog resolution | 100 |
| 7.5.3 | Analog resolution without ToT calibration | 102 |
| 7.5.4 | Spatial resolution in the presence of a magnetic field | 103 |
| 7.6 | y-spatial resolution | 104 |
| 7.7 | Conclusions | 105 |
| 8 | ATLAS <i>b</i>-tagging and tracking performance | 106 |
| 8.1 | Simulation and reconstruction software | 106 |
| 8.1.1 | ATLAS detector simulation | 106 |
| 8.1.2 | Reconstruction | 108 |
| 8.2 | Pixel point resolution | 109 |
| 8.2.1 | Angles of incidence and cluster sizes | 109 |
| 8.2.2 | Barrel $R\phi$ spatial resolution | 112 |
| 8.2.3 | Barrel z resolution | 116 |
| 8.2.4 | Disk resolution | 118 |
| 8.3 | Tracking performance | 118 |
| 8.4 | <i>b</i> -tagging performance | 123 |
| 8.4.1 | Jets used for <i>b</i> -tagging studies | 123 |
| 8.4.2 | <i>b</i> -tagging methodology | 125 |
| 8.4.3 | Results | 129 |

Introduction

The need of probing the electroweak symmetry breaking mechanism of the Standard Model and the possible new physics which may be related to it has led to the decision of building the Large Hadron Collider, which will increase by an order of magnitude the energy and luminosity of present colliders.

Two general-purpose particle detectors, ATLAS and CMS, have been approved to operate at the LHC which is scheduled to provide the first proton beams by 2006. Both of them use a silicon pixel detector to provide high-resolution measurements of particle position near the interaction point. This allows the identification of the secondary vertices produced by heavy flavor hadrons and tau decays, which is an essential tool for many physics analyses.

These detectors will have to face extremely high radiation level, given their vicinity to the interaction region and the high collision rate of the LHC.

In the last few years, the ATLAS Pixel collaboration carried on an intense activity of testing and optimizing the various detector components, assessing their radiation hardness and their ability to meet the performance targets. In the contest of this activity a fundamental role was played by the testing of the prototypes with a pion beam at CERN. The prototypes have been studied both before and after having been exposed to radiation doses similar to those expected at the LHC.

Most of this thesis is devoted to the analysis of the test beam data. The first three chapters provide the description of the ATLAS experiment, of the ATLAS Pixel detector, of the test beam setup and of the tested devices. The fourth chapter describes the measurements of charge collection and efficiency of the tested pixel devices. The former affects the detector performances (detection efficiency and spatial resolution) and it is useful to understand the differences between the tested designs. The latter needs to be high; a single pixel efficiency of 97% is required to assure a good efficiency in detecting secondary vertices and discriminating photons from electrons.

The fifth chapter is devoted to the measurement of the depleted thickness of the silicon sensors [1, 2] for different irradiation levels and bias voltages. The depleted zone is the sensitive volume and it needs to be thick enough to assure a good signal over noise ratio. As the radiation damage ultimately decreases the depleted depth at a given bias voltage, and the bias voltage cannot be increased above about 600 V, the requirement of a minimum depleted depth translates in a maximum amount of radiations the sensors can be exposed to. Hence the measurements presented in this chapter investigate the radiation hardness of the pixel sensors.

The sixth chapter presents the measurements of Lorentz angle [1, 3]. This is the angle between the direction of motion of the charge carriers (electrons

and holes) inside the silicon and the electric field (which is normal to the sensor surface). In presence of a magnetic field it may be different from zero because of the $\vec{E} \times \vec{B}$ force. The Lorentz angle affects the number of pixels which share the charge released by the particle. The spatial resolution is also affected, as charge interpolation is only possible when more than a pixel collects the signal.

The seventh chapter describes a study of spatial resolution [1, 4]. Different algorithms for pixel cluster position reconstructed have been investigated in order to achieve the best possible resolution.

The last chapter investigates some consequences of the lessons learned in test beam data analysis for the ATLAS performance. In particular, charge interpolation was used for the first time in the reconstruction of pixel cluster position for simulated data. This allows to obtain a better precision for the pixel hits position, a precision which depends on the value of the Lorentz angle which was found to vary with the applied voltage (chapter 6). Pixel point resolution, track parameters resolution and beauty quark tagging performance were studied for the different pixel cluster reconstruction algorithms and for different values of the pixel bias voltage.

Chapter 1

The ATLAS experiment

1.1 General overview

1.1.1 Physics motivations and goals

ATLAS (**A** **T**oroidal **L**HC **A**pparatu**S**) is a general-purpose detector designed to exploit the full discovery potential of the Large Hadron Collider (LHC). The LHC [5] is a proton-proton collider with 14 TeV centre of mass energy and design luminosity of $10^{34} \text{ cm}^{-2}\text{s}^{-1}$. A first period of running at the lower luminosity of $10^{33} \text{ cm}^{-2}\text{s}^{-1}$ is also foreseen. Beam crossings are 25 ns apart and at design luminosity there are 23 interactions per crossing.

The LHC offers a large range of physics opportunities. The ATLAS Physics programme is described in Section 1.2. The origin of mass at the electroweak scale is a major focus of interest for ATLAS. The detector optimization is therefore guided by physics issues such as sensitivity to the largest possible Higgs mass range. High resolution measurements of electrons, photons and muons, excellent secondary vertex detection for τ leptons and b -quarks, high resolution calorimetry for jets and missing transverse energy are essential to explore the full range of possible Higgs boson masses.

Other important goals are the searches for W- and Z-like objects, for supersymmetric particles, for compositeness of the fundamental fermions, the detailed study of the top quark and investigation of CP violation in B-decays. The ability to cope well with a broad variety of possible physics processes is expected to maximize the detector's potential for the discovery of new, unexpected physics.

Many of the interesting physics questions at the LHC require high luminosity, and so the primary goal is to operate at the higher luminosity with a detector that provides as many signatures as possible. The variety of signatures is considered to be important in the high-rate environment of the LHC in order to achieve robust and redundant physics measurements with the ability of internal cross-checks.

Emphasis is also put on the performance necessary for the physics accessible during the initial lower luminosity running, which despite the poorer statistics has the advantage of cleaner events, with only ~ 2 pp primary interactions per event.

Operating a detector in the high-rate LHC environment requires a very high resistance to radiation damage, posing an unprecedented challenge for all the

subdetectors.

1.1.2 Overall detector concept

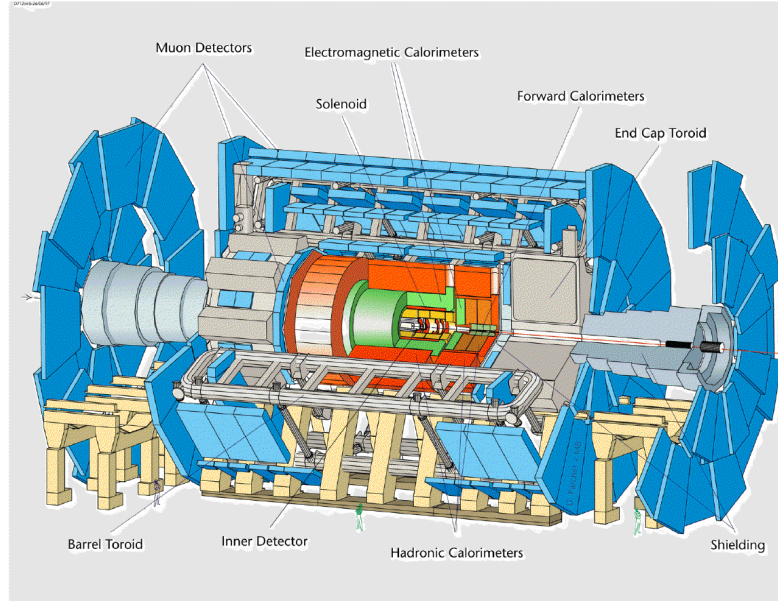


Figure 1.1: Overall layout of the ATLAS detector .

The overall detector layout is shown in Fig. 1.1 [6]. It is designed to cover as much as possible of the solid angle around the collision point.

A **magnetic field** is provided by a thin superconducting solenoid surrounding the inner detector cavity, and large superconducting air-core toroids consisting of independent coils arranged with an eight-fold symmetry outside the calorimeters. The magnetic field allows to measure the transverse momentum (p_T) of charged particles from the curvature of tracks.

The **Inner Detector** is contained within a cylinder of length 7 m and a radius of 1.15 m, in a solenoidal magnetic field of 2 T. It provides efficient tracking at high luminosity for high- p_T lepton momentum measurements, electron and photon identification, τ lepton and heavy flavor jets identification, and full event reconstruction capability at lower luminosity. This is achieved with a combination of high resolution semiconductor pixel and strip detectors in the inner part of the tracking volume, and straw tube tracking detectors with transition radiation capability in its outer part.

Highly granular liquid argon (LAr) electromagnetic (EM) sampling calorimetry, with excellent performance in terms of energy and position resolution, is used for electron and photon identification and measurements. The hadronic calorimeters provide accurate jet and missing transverse energy (E_T^{miss}) measurements. The bulk of the hadronic calorimetry is provided by a novel scintillator-tile calorimeter, which is separated into a large barrel and two smaller extended barrel cylinders, one on each side of the barrel. In the end-caps the LAr technol-

ogy is used. The barrel and forward LAr calorimetry is contained in a cylinder with an outer radius of 2.25 m and extends longitudinally to ± 6.65 m along the beam axis. The outer radius of the scintillator-tile calorimeter is 4.25 m and its half length is 6.10 m.

The calorimeter is surrounded by the **muon spectrometer**. This provides for high precision muon momentum measurements, with the capability to guarantee accurate measurements at the highest luminosity. The air-core toroid system generates a large magnetic field volume with strong bending power within a light and open structure. Multiple scattering is thereby minimized, and excellent muon momentum resolution is achieved with three stations of high precision tracking chambers. The muon instrumentation also includes as a key component trigger chambers with very fast time response. The muon spectrometer defines the overall dimensions of the ATLAS detector. The outer chambers of the barrel are at a radius of about 11 m. The half-length of the barrel toroid coils is 12.5 m, and the third layer of the forward muon chambers, mounted on the cavern wall, is located about 23 m from the interaction point. The overall weight of the ATLAS detector is about 7000 tons.

1.1.3 Reference system and definitions

The beam direction defines the z axis, and the $x-y$ plane is the plane transverse to the beam direction. The azimuthal ϕ axis is measured around the beam axis, and the polar angle θ is the angle from the beam axis. The pseudorapidity is defined as

$$\eta = -\ln \tan(\theta/2) \quad (1.1)$$

The transverse momentum p_T and the transverse energy E_T , as well as the missing transverse energy E_T^{miss} are defined in the xy plane. The distance ΔR in the pseudorapidity-azimuthal angle space is defined as $\Delta R = \sqrt{\Delta^2\eta + \Delta^2\phi}$.

Trajectories of charged particles can be described by five helix parameters in an ideal uniform magnetic field. The helix parametrisation used in ATLAS makes use of $1/p_T$, ϕ , d_0 , $\cot\theta$, z_0 , with all the quantities measured at the point of closest approach to the nominal beam axis. d_0 is the impact parameter in the $x-y$ plane, signed according to the reconstructed angular momentum about the axis. z_0 is the z position of the track at the point of closest approach.

1.2 The ATLAS physics programme

The high energy and luminosity of the LHC offers a large range of physics opportunities [6], from the precise measurement of the properties of known objects to the exploration of the high energy frontier. The desire to probe the origin of the electroweak scale leads to a major focus on the Higgs boson; ATLAS must be sensitive to it over the full range of allowed masses. Other important goals are searches for other phenomena possibly related to the symmetry breaking, such as particles predicted by supersymmetry or technicolour theories, as well as new gauge bosons and evidence for composite quarks and leptons. The investigation of CP violation in B decays and the precision measurements of W and top quark masses and triple gauge boson couplings will also be important components of the ATLAS physics programme.

1.2.1 Standard Model physics

In the initial phase at low luminosity, the experiment will function as a factory for QCD processes, heavy flavor and gauge bosons production. This will allow to perform stringent test of the Standard Model predictions and to improve the precision with which the parameters of the model are known. Deviations from the Standard Model expectations may indicate the occurrence of new physics. Improving the precision on the Standard Model parameters is also essential to evaluate the background in the searches for new phenomena.

QCD studies. The calculation of the production cross-section at the LHC both for interesting physics processes and their backgrounds relies upon a precise knowledge of the distribution of the momentum fraction of the partons inside the proton in the relevant kinematic range. This extends to higher energy scales and smaller fractional momenta of the scattered parton than the range probed at the current accelerators. ATLAS data from Drell-Yan, direct photon, jet and top production will be used to improve the knowledge of parton density functions in the kinematic range of the LHC. The properties of minimum bias events (total cross section, charged particle spectra and jet structure at small transverse energy) also need to be measured to evaluate the background to physics analyses. The jet production cross section will be measured to test QCD predictions and measure the scale dependence of α_s up to several TeV. Charm, bottom and top quark production will also be studied in detail.

Gauge bosons. One of the challenges of the ATLAS experiments will be whether the precision of the W -mass measurement can be improved. The present value from LEP and Tevatron data is 56 MeV [7]. In ATLAS the expected statistical uncertainty [6] will be a few MeV. The very ambitious goal for both theory and experiment is to reduce the individual sources of systematic errors to the level which would allow for the measurement of the W mass with a precision of better than 20 MeV. This would ensure that the precision of the W mass is not the dominant source of errors in testing radiative corrections in the SM prediction for the Higgs mass.

The large rate of gauge boson pair production at the LHC enables ATLAS to provide critical tests of the triple gauge-boson couplings. The gauge cancellations predicted by the Standard Model will be studied and measurements of possible anomalous couplings made. These probe underlying non-standard physics. The most sensitive variables to compare with Standard Model predictions are the transverse momentum spectra of high- p_T photons or reconstructed Z bosons.

Beauty physics. Even at low luminosity, LHC is a beauty factory with 10^{12} $b\bar{b}$ expected per year. The available statistics will be limited only by the rate at which data can be recorded and it will be higher than in any previous accelerator. The proposed B -physics programme is therefore very wide. An important aim of the B -physics work is to test the Standard Model through precision measurements of B hadron decays that together will over-constrain the CKM matrix, possibly giving indirect evidence for new physics. This programme will include the following: precise measurement of CP violation in B -meson decays, which in the Standard Model is due to a single phase in the CKM matrix; precise measurement of the periods of flavor oscillations in B_s^0 as well in B_d^0 mesons, and of relative decay rates; searches for and measurements of very rare decays which are very strongly suppressed in the Standard Model and

where significant enhancements could provide indirect evidence for new physics. At the LHC, the general-purpose experiments ATLAS will face stiff competition from LHCb, which is a dedicated B -Physics experiment. However, even though a dedicated experiment can be better optimized for certain event types, ATLAS will be competitive in several channels. It will thus contribute to the combined precision of B -physics measurements from the LHC.

Top physics. LHC has a large potential for performing high precision top physics measurements with about eight million $t\bar{t}$ pairs expected to be produced for an integrated luminosity of 10 fb^{-1} (one year of data taking at low luminosity). It would allow for the measurement of the top-quark mass with a precision of $\sim 2 \text{ GeV}$, to be compared to the current precision [7] of 5.1 GeV . The single top production should be observable and the high statistics will allow searches for many rare top decays. The precise knowledge of the top-quark mass places strong constraints on the mass of the Standard Model Higgs boson, while a detailed study of its properties may reveal as well new physics.

1.2.2 Standard Model Higgs boson

The $SU(2) \times U(1)$ symmetry group of the Standard Model, which describes the so-called electroweak interaction, is spontaneously broken by the existence of a postulated Higgs field. This leads to the emergence of massive vector bosons, the W and Z , which mediate the weak interaction, while the photon remains massless. One physical degree of freedom remains in the Higgs sector which should manifest itself as a neutral scalar boson H^0 which is presently unobserved.

Although within the model there is no guidance about the Higgs mass itself, some constraints can be delivered from the perturbative calculations within the model requiring the Higgs couplings to remain finite and positive up to an energy scale. If the Higgs mass is in the range of 160 to 170 GeV [8] then the renormalisation-group behaviour of the Standard Model is perturbative and well-behaved up to Planck Scale $\Lambda_{Pl} \sim 10^{19} \text{ GeV}$; for smaller or larger values of m_H new physics must set in below Λ_{Pl} . As the Higgs mass increases, the self couplings and the couplings to the W and Z grow [9, 10]. This feature has a very important consequence. Either the Higgs boson must have a mass less than about 800 GeV, or the dynamics of WW and ZZ interactions with center-of-mass energies of the order of 1 TeV will reveal new structure. It is this simple argument that sets the energy scale that must be reached to guarantee that an experiment will be able to provide information on the nature of electroweak symmetry breaking.

The most stringent limits on the Standard Model Higgs boson mass come from LEP data. A lower limit can be derived from direct search. Indirectly, high precision electroweak data constrain the Higgs boson mass via their sensitivity to loop corrections. The preliminary combined lower limit (at 95% confidence level) of the LEP experiments with the data taken in 2000 with a center-of-mass energy of 209 GeV by the LEP experiments is $m_H > 114 \text{ GeV}$ [11, 12, 14, 13, 15]. An Higgs signal with $m_H = 115 \text{ GeV}$ may also have been seen, the probability that it is a background fluctuation being 3.5% [11]. Electroweak data favor a light Higgs: a global fit leads to $m_H = 76^{+85}_{-47} \text{ GeV}$ [16].

Various detection strategies are envisaged in ATLAS, depending on the Higgs mass (Fig. 1.2). b -tagging is crucial for a light Higgs ($m_H < 120 \text{ GeV}$) when $H \rightarrow b\bar{b}$ is the dominant decay channel. Since this process is affected by a

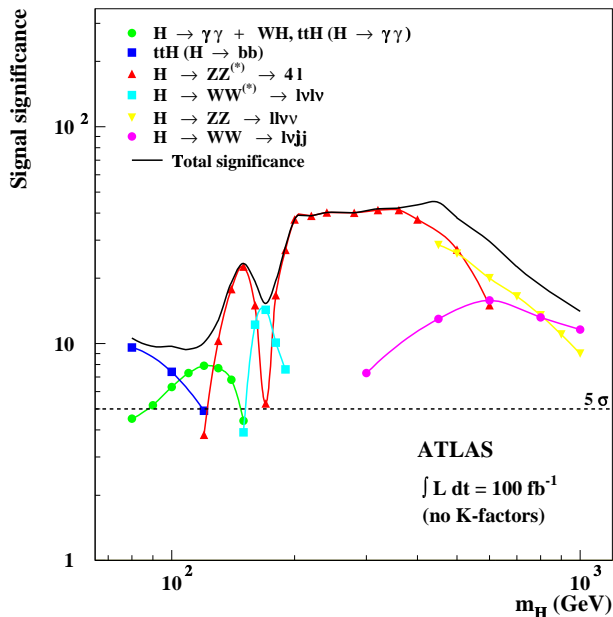


Figure 1.2: ATLAS sensitivity for the discovery of a Standard Model Higgs boson, assuming integrated luminosity of 100 fb^{-1} [6] .

large QCD background, two particular final production and decay processes are looked for: $pp \rightarrow t\bar{t}H \rightarrow l\nu jj\bar{b}\bar{b}\bar{b}\bar{b}$ and $pp \rightarrow WH \rightarrow l\nu b\bar{b}$ where j indicates a generic hadronic jet and l a muon or electron. The signature is thus two or four beauty jets and an high- p_T lepton. The Higgs shows up as a peak in the invariant mass of the tagged beauty jets (Fig. 1.3).

The good reconstruction of photon pairs invariant mass by the electromagnetic calorimeter allows to search for the rare Higgs one-loop decay in two photons for $m_H < 150 \text{ GeV}$. $H \rightarrow ZZ^* \rightarrow 4l$ and $H \rightarrow WW^* \rightarrow l\nu l\nu$ are used for $120 \text{ GeV} < m_H < 180 \text{ GeV}$. When the Higgs mass allows its decay into two real Z bosons, the channel $H \rightarrow ZZ \rightarrow 4l$ provides a very clean and background-free signature. If m_H is larger than about 700 GeV , however, the rate of this channel becomes too small and decays with higher branching ratio ($H \rightarrow ZZ \rightarrow lljj$ and $H \rightarrow WW \rightarrow l\nu jj$) are searched for.

Fig. 1.2 shows the expected statistical significance for the discovery of a Standard Model Higgs as a function of the Higgs mass, after three years of running at low luminosity and one year at high luminosity.

1.2.3 Supersymmetry

The presence of a single elementary scalar boson is unsatisfactory to many theorist, because if the Standard Model is part of some more general theory which has some other larger mass scale (such as the Grand Unification scale or the Planck scale) then a serious fine tuning of parameters is required to avoid radiative corrections to drive the Higgs mass toward the larger scale. There are two ways out of this problem which both involve new physics at the scale of

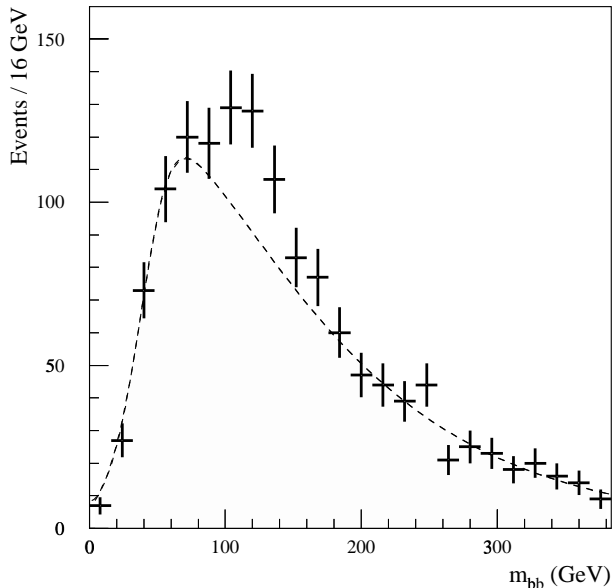


Figure 1.3: Invariant mass distribution of tagged b -jet pairs in fully reconstructed $t\bar{t}H$ signal events with an Higgs boson mass of 120 GeV above the summed background [6] .

1 TeV: new strong dynamics could enter that provides the scale of m_W , or new particles could appear such that the radiative divergences are canceled.

Supersymmetry [17] offers the only presently known mechanism for incorporating gravity in the quantum theory of particle interactions and provides an elegant cancellation mechanism for the divergences, avoiding any fine tuning. Supersymmetric models postulate the existence of superpartners for all the presently observed particles: bosonic superpartners of fermions (squarks and sleptons) and fermionic superpartners of bosons (gluinos and gauginos). There are also multiple Higgs bosons, the neutral h , H , A and the charged H^\pm . There is thus a large spectrum of presently unobserved particles, whose exact masses, couplings and decay chains are calculable in the theory given certain parameters. Unfortunately these parameters are unknown. However, if supersymmetry has anything to do with electroweak symmetry breaking, the masses should be in the region below or of the order of 1 TeV.

Discovering SUSY at the LHC will be straightforward if it exists at the electroweak scale. Copious production of squarks and gluinos can be expected, since the cross section should be as large as a few pb for squarks and gluinos as heavy as 1 TeV. Their cascade decays would lead to a variety of signatures involving multi-jets, leptons, heavy flavors and missing energy. The main challenge would be not to discover SUSY itself, but to determine its nature and determine the underlying SUSY model. In several models the precision measurement of the masses of the SUSY particles and the determination of the model parameters will be possible.

Fig. 1.4 shows the ATLAS sensitivity to the Higgs bosons within the Minimal SuperSymmetric Model with maximal mixing, for an integrated luminosity of

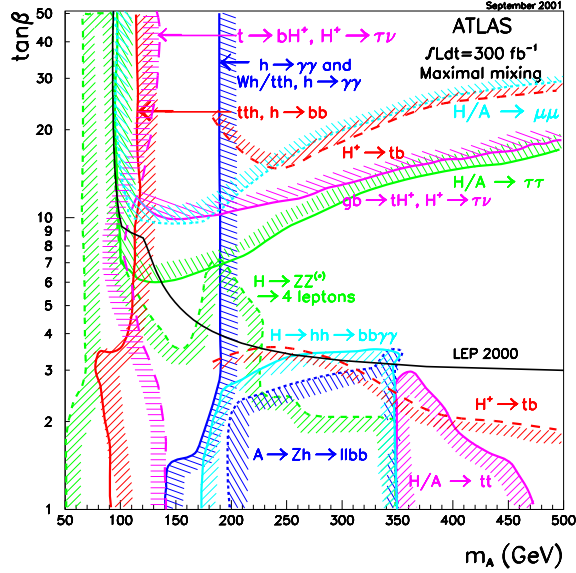


Figure 1.4: ATLAS sensitivity for the discovery of MSSM Higgs bosons (in the case of maximal mixing). The 5σ discovery contour curves are shown in the $(m_A, \tan\beta)$ plane for individual channels and for an integrated luminosity of 300 fb^{-1} . The LEP limit is also shown.

300 fb^{-1} . With these assumptions there are two free parameters, m_A and $\tan\beta$. The sensitivity of various discovery channels is shown as 5σ discovery contour curves in the $(m_A, \tan\beta)$ plane. The LEP final limit is also reported. The h boson behaves like a light Standard Model Higgs boson and it searched for through the $h \rightarrow \gamma\gamma$ and $t\bar{t}h, h \rightarrow b\bar{b}$ channels, the latter allowing discovery over most of the parameter space. However the discovery of one of the heavier Higgs boson would allow an easier measurement of m_A and $\tan\beta$.

1.2.4 Other physics beyond the Standard model

Technicolour models [18] provide for electroweak symmetry breaking introducing new dynamics rather than with an Higgs mechanism. The large top mass and the absence of any observation of flavor changing neutral currents exclude the simplest models, such that an elegant implementation of this idea is lacking. If the dynamics has something to do with electroweak symmetry breaking, new resonances arise in the region below 1 TeV.

There are also other possibilities for new physics that are not necessarily related to the scale of electroweak symmetry breaking. They include:

- **A fourth family** of quark and leptons. This is possible only if the fourth family neutrinos are heavier than about half the mass of the Z , so that they do not contribute to the Z width. Fourth family quarks can be searched directly up to a quark mass of about 700 GeV [6]. They would also enhance the Higgs production and modify the branching ratios of its

decay modes. The possibility of observing the heavy leptons is also under study.

- **Compositeness**, which is suggested by the existence of three families. Excited quarks decay in a jet and a photon, deviations from QCD predictions for jet production, and leptoquarks (particles with both lepton and baryon quantum numbers) will be looked for.
- **New gauge bosons**, arising from new symmetry groups in Standard Model extensions.
- **Right-handed Majorana neutrinos**.
- Dirac **magnetic monopoles** [19], restoring the symmetry of the Maxwell's equations and explaining the quantization of electric charge. They will be searched through their loop contribution to photon-photon scattering, an analysis which is sensible to monopoles up to a mass of several TeV.

1.3 The ATLAS detector

1.3.1 The Inner Detector

The layout of the Inner Detector is shown in Figure 1.5.

The momentum and vertex resolution requirements from physics call for high precision position measurements to be made with fine granularity detectors, given the very large track density expected at the LHC at the highest luminosity (Fig. 1.6). Semiconductor tracking detectors, using silicon microstrip (SCT) [20] and pixel [21] technologies offer these features. The highest granularity is achieved around the vertex region using semiconductor pixel detectors. The total number of precision layers must be limited because of the material they introduce, and because of their high cost. Typically, three pixel layers and eight strip layers (four space point) are crossed by each track. A large number of tracking points (typically 36 per track) is provided by the straw tube tracker (TRT) [20], which provides continuous track-following with much less material per point and at a lower cost. The straw hits at the outer radius contribute significantly to the momentum measurement, since the lower precision per point compared to the silicon is compensated by the large number of measurements and the higher average radius. The relative precision of the different measurements is well matched, so that no single measurement dominates the momentum resolution. This implies that the overall performance is robust. The high density of measurements in the outer part of the tracker is also valuable for the detection of photon conversions and of neutral particles decays. The latter are an important element in the signature of a CP violation in the B system. In addition, the electron identification capabilities of the whole experiment are enhanced by the detection of transition-radiation photons in the xenon-based gas mixture of the straw tubes. The secondary vertex measurement performance, which is the essential tool for heavy flavor and τ tagging, is based on the pixel detector measurements at low radii.

The position of the elements of the Inner Detector will have to be known with a precision better than the intrinsic resolution of the detectors. In the Inner Detector Technical Design Report [20] the goals for the alignment were

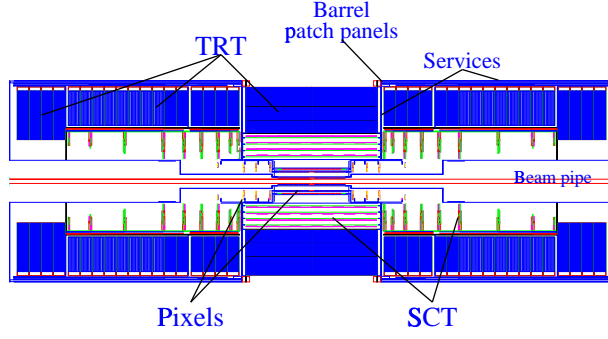


Figure 1.5: Longitudinal view of the ATLAS Inner detector .

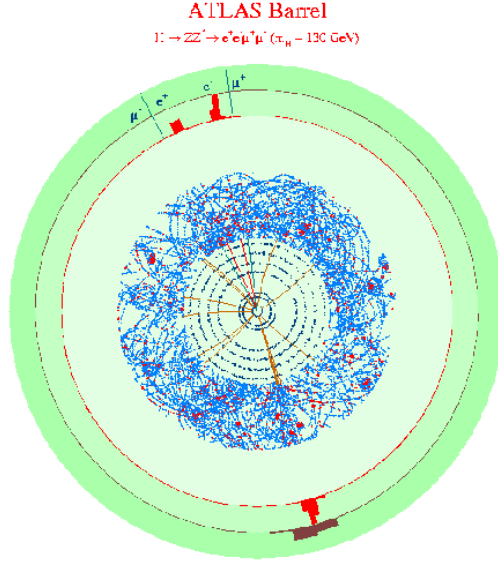


Figure 1.6: Display in the transverse plane of a simulated high- p_T $H \rightarrow ZZ^* \rightarrow e^+e^-\mu^+\mu^-$ decay (Higgs mass = 130 GeV) in the ATLAS barrel Inner Detector and calorimeters at a luminosity of $5 \times 10^{33} \text{ cm}^{-2}\text{s}^{-1}$ [6]. The four leptons and the recoiling jet are visible. Hits in the Inner Detector are shown over the range $|\eta| < 0.7$. High threshold transition radiation hits are drawn as red points. Reconstructed tracks with $p_T > 1$ GeV and $|\eta| < 0.7$ are shown (in yellow). The reconstructed tracks are shown in red for electrons and in blue for the muons. The histograms show the energy deposition in the EM Calorimeter (pale green) and Hadronic Calorimeter (dark green).

such that misalignments should degrade the track parameter resolutions by no more than 20%. This led to requirements that in $R\phi$ the Pixel detectors should be aligned to $\sim 7 \mu\text{m}$ while the SCT detectors should be aligned to $\sim 12 \mu\text{m}$. The desire to measure the W mass to 20 MeV [6] will necessitate knowing the momentum scale of the ID to about 0.02%, which implies an alignment precision on each single module of $\sim 1 \mu\text{m}$ [22] which is a very difficult and ambitious goal.

Initially the Pixel and SCT module positions will be determined from mechanical measurements, an X-rays survey and the frequency scan interferometry which measures a network of lengths in the SCT. This will provide a starting point for the alignment with physics events tracks [6, 22] which will be performed daily.

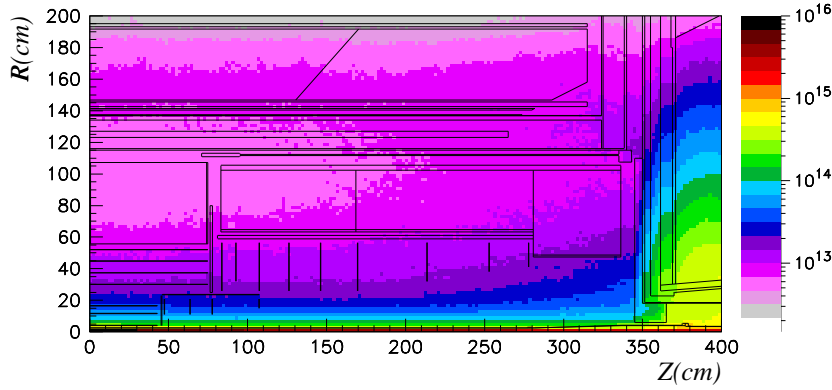


Figure 1.7: Fluence in the ID cavity expressed in units of 1 MeV equivalent neutrons per cm^2 per year.

The inner detector components will have to be resistant to the large expected radiation levels (Fig. 1.7).

The Pixel detector

The Pixel detector is designed to provide three high-resolution points per track as close to the interaction point as possible. It mostly determines the ability to find short-lived particles such as B mesons and τ leptons through the identification of displaced vertices. It also offers a powerful tool for track separation and reconstruction because of the two dimensional segmentation of the sensors.

A detailed description of the ATLAS Pixel detector is given in chapter 2.

The SemiConductor Tracker

The SCT is designed to provide four track points in the intermediate radial range, contributing to the measurement of momentum and impact parameter. The system is an order of magnitude larger in surface area than the previous generations of silicon microstrip detectors, and in addition must face radiation levels which will alter the fundamental characteristics of the silicon wafers themselves.

The barrel SCT uses four double layers of p -on- n silicon microstrip detectors. Each double layer consists of strips aligned in the azimuthal direction and strips

rotated by a 40 mrad stereo angle with respect to the first set. The strips have a 80 μm pitch and are 12 cm long. The readout chain consists of a front-end amplifier and discriminator, followed by a binary pipeline which stores the hits above threshold until the level-1 trigger decision.

The spatial resolution is 16 μm in $R\phi$ and 580 μm in z .

On each side there are nine end-cap wheels, with up to three rings per wheel. The radial range of each disk is adapted to limit the coverage to $|\eta| < 2.5$ by equipping each one with the minimum number of rings and by using the appropriate set of modules.

The SCT as well as the Pixel system require cooling to remove the heat generated by the electronics and detector leakage current. The two detectors are jointly referred to as Precision Tracker.

The Transition Radiation Tracker

The TRT is based on the use of straw detectors, which can operate at the very high rates expected at the LHC by virtue of their small diameter and the isolation of the sense wires within individual gas volumes. Electron identification capability is added by employing xenon gas to detect transition-radiation photons created in a radiator between the straws. This technique is intrinsically radiation hard, and allows a large number of measurements, typically 36, to be made on every track at modest cost. However, the detector must cope with a large occupancy and high counting rates at the LHC design luminosity.

Each straw is 4 mm in diameter and equipped with a 30 μm diameter gold-plated W-Re wire. The barrel contains about 50 000 straws, each divided in two at the centre, in order to reduce the occupancy, and read out at each end. The end-caps contain 320 000 radial straws, with the readout at the outer radius. Each channel provides a drift time measurement, giving a spatial resolution of 170 μm per straw, and two independent thresholds. These allow the detector to discriminate between tracking hits, which pass the lower threshold, and transition radiation hits which pass the higher one. The TRT is operated with a non-flammable gas mixture of 70% Xe, 20% CO₂ and 10% CF₄ with a total volume of 3 m³.

The barrel section is built of individual modules with between 329 and 793 axial straws each, covering the radial range from 56 to 107 cm. The first six radial layers are inactive over the central 80 cm of their length, in order to reduce their occupancy, while providing extra coverage for the crack between the barrel and the end cap sections.

The two end caps each consist of 18 wheels. The 14 wheels nearest to the interaction point cover the radial range from 64 to 103 cm, while the last four wheels extend to an inner radius of 48 cm in order to keep a constant number of crossed straws over the full acceptance. To avoid an unnecessary increase in the number of crossed straws and material at medium rapidity, wheels 7 to 14 have half as many straws per cm in z as the other wheels.

A primary concern in the design of this sub-system has been to obtain a good performance at high occupancy and counting rate. In the barrel, the rate of hits above the lower threshold varies with radius from 6 to 18 MHz, while in the end caps the rate varies with z from 7 to 19 MHz. The maximum rate of hits above the higher transition radiation threshold is 1 MHz. Within a single drift time bin, the occupancy is about one third of that in the entire active time

window. Position accuracies of about $170\text{ }\mu\text{m}$ have been achieved in tests at average straw counting rates of about 12 MHz. At these rates, only about 70% of the straws give correct drift time measurements because of shadowing effects, but the large number of straws per track guarantees a combined measurement accuracy of better than $50\text{ }\mu\text{m}$ at the LHC design luminosity, averaged over all straws and including a systematic error of $\sim 30\text{ }\mu\text{m}$ from alignment.

A good pattern recognition performance is also assured by the continuous tracking. Within the radial space available, the straw spacing has been optimized for tracking at the expense of electron identification, which would be improved by a larger path length through the radiator material and fewer straw detectors. The distribution of the straws over the maximum possible path length enhances the pattern recognition performance, by reducing the effect of loopers and interactions which can saturate small regions of the detector. The TRT provides additional discrimination between electrons and hadrons, with *e.g.* a pion rejection factor at $p_T = 20\text{ GeV}$ varying with η between 20 and 100 at 90% electron efficiency.

1.3.2 The calorimeters

The ATLAS calorimeters are designed to measure the total energy of incident hadrons, photons and electrons. Neutral particles (photons and neutral hadrons) are detected only by the calorimeters. Electromagnetic calorimetry provides for electron and photon identification and the precise measurement of their energy. Hadronic calorimeters measure jet and transverse missing energy.

A view of the ATLAS calorimeters is presented in Figure 1.8 [6]. The system consists of an electromagnetic (EM) calorimeter covering the pseudorapidity region $|\eta| < 3.2$, an hadronic barrel calorimeter, hadronic end-cap calorimeters and forward calorimeters.

The **EM calorimeter** is divided into a barrel part and two end-caps. It is a lead/liquid argon (LAr) detector with accordion-shaped electrodes. The accordion geometry provides complete ϕ symmetry without azimuthal cracks. The thickness of lead in the absorber plates has been optimized as a function of η in terms of EM calorimeter performance in energy resolution. The calorimeter is segmented in η and ϕ to provide for EM showers position measurement. The total number of channels is about 190 000.

The total material seen by an incident particle before the calorimeter front face is 2.3 radiation lengths, and increases with pseudorapidity in the barrel because of the particle angle. Over the pseudorapidity range $|\eta| < 1.8$ a pre-sampler is used to correct for the energy lost by electrons and photons upstream of the calorimeter.

Fig. 1.9 reports the energy resolution as measured in the test beam operation of an EM end-cap module prototype [6].

The ATLAS **hadronic calorimeters** (Fig. 1.8) cover the range $|\eta| < 4.9$ using different techniques best suited for the widely varying requirements and radiation environment over the large η range.

The large hadronic barrel calorimeter is a sampling calorimeter using iron as absorber and scintillating tiles as active material. The scintillating tiles are read out on two opposite sides by wavelength shifting fibres into two separate photomultipliers. The granularity is $\Delta\eta \times \Delta\phi = 0.1 \times 0.1$ and the total number of channels is about 10 000. Each hadronic end-cap calorimeter consists of two

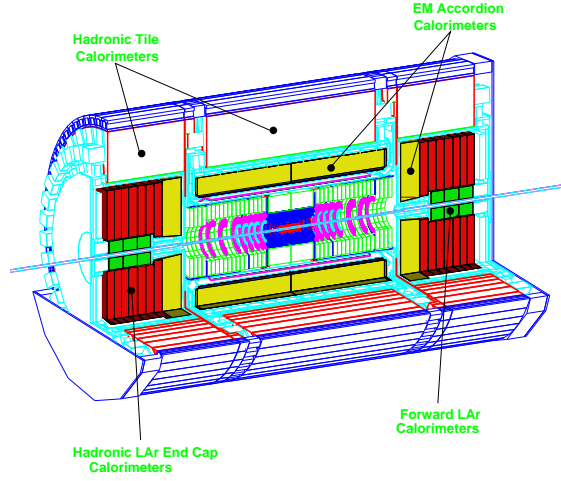


Figure 1.8: Three dimensional cutaway view of the ATLAS calorimeters .

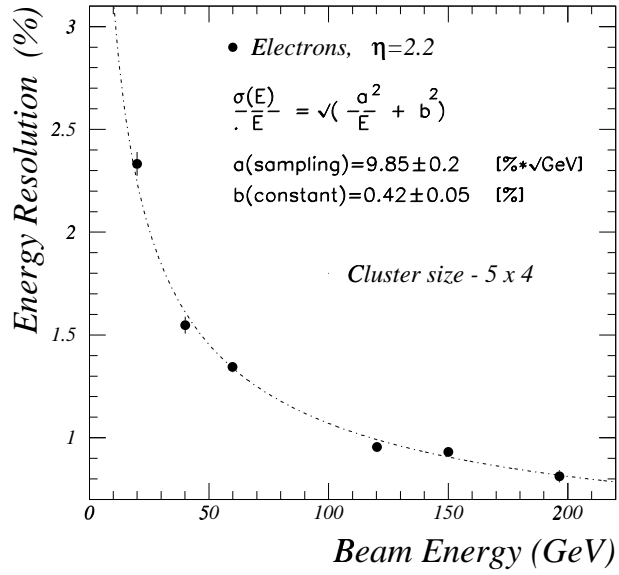


Figure 1.9: Energy resolution of the end-cap module zero as a function of energy at $\eta \sim 2.2$. The best fit is superimposed .

independent wheels, which alternate copper plates with liquid argon sensitive layers. The liquid argon forward calorimeter extends the pseudorapidity coverage up to $|\eta| = 4.9$. It is a particularly challenging detector owing to the high

level of radiation it has to cope with. It is divided into a section made of copper and two made out of tungsten, resulting in a compact high density detector.

An important parameter in the design of the hadronic calorimeter is its thickness: it has to provide good containment for hadronic showers and reduce punch-through into the muon system to a minimum. The total thickness is 11 interaction lengths (λ) at $\eta = 0$, including about 1.5λ from the outer support. This is sufficient to reduce the punch-through well below the irreducible level of prompt or decay muons. Nearly 10λ of active calorimeter are adequate to provide good resolution for high energy jets. Together with the large η coverage, this will also guarantee a good E_T^{miss} measurement, which is important for many physics signatures and in particular for SUSY particle searches.

1.3.3 The muon spectrometer

Among charged particles, only muons are penetrating enough to pass through the calorimeters and reach the external spectrometer. Their momentum is measured from the curvature of tracks in the magnetic field provided by the air-core toroid magnets. Due to the high interaction rate, the detectors must satisfy constraints on parameters such as rate capability and radiation hardness. They must also cope with difficult background conditions resulting from penetrating primary collision products and from radiation backgrounds, mostly neutrons and photons in the 1 MeV range, produced from secondary interactions.

The chambers are arranged such that particles from the interaction point traverse three stations of chambers up to $|\eta| = 2.7$. In the barrel region, the magnetic field is such that the Lorentz force is along z . The chambers are arranged in three cylinders concentric with the beam axis. In the end-cap region the Lorentz force is along R and the chambers are arranged in four disks concentric with the beam axis.

Over most of the η -range a precision measurement along the bending direction is provided by the Monitored Drift Tubes (MDTs). They provide a single wire resolution of about $80 \mu\text{m}$. “Monitored” refers to the optical system monitoring mechanical deformations.

At large pseudorapidities and close to the interaction point, multiwire proportional chambers with cathode strip readout (Cathode Strip Chambers, CSCs) with higher granularity are used instead of MDTs, as they better withstand the demanding rate and background conditions.

The trigger system is composed of Resistive Plate Chambers (RPCs) in the barrel and by multiwire proportional chambers with a small cathode-anode gap, called Thin Gap Chambers (TGCs), in the end-cap regions. They provide bunch crossing identification, which requires a time resolution better than the LHC bunch spacing of 25 ns, they provide a trigger with well defined p_T cutoff, optimized to cope with the background, and they finally measure the second coordinate in the direction orthogonal to that measured by the precision chambers, with a typical resolution of 5-10 mm.

1.3.4 Trigger, data acquisition and computing

Starting from an initial bunch-crossing rate of 40 MHz (interaction rate of $\sim 10^9 \text{ Hz}$ at a luminosity of $10^{34} \text{ cm}^{-2}\text{s}^{-1}$), the rate of events selected by the trigger must be reduced to $\sim 100 \text{ Hz}$ for permanent storage. While this requires

a rejection rate of 10^7 against minimum-bias events, excellent efficiency must be retained for the rare new physics processes, such as Higgs boson decays, which will be searched for in ATLAS. The output data volume will still be very high (about 10^{15} Bytes/year) requiring new methods for data processing and access.

The ATLAS trigger and data-acquisition (DAQ) system is based on three levels of online events selection. Each level has a lower input rate than the previous one, and more time per event to make its decision, so that it can process more event informations and apply more complex algorithms to provide additional rejection power.

The **level-1** trigger makes an initial selection using muon trigger chambers to identify high- p_T muons, and the calorimeters to search for high- p_T electrons and photons, jets, and tau leptons decaying into hadrons, as well as large missing and total transverse energies. The requirements on the level-1 trigger are a maximum rate of 75 kHz, the ability to identify the bunch crossing of interest, and a maximum latency of $2.5\ \mu\text{m}$. The latency is the time taken to form and distribute the trigger decision. During this time, information for all detectors channels has to be kept in pipeline memories. These are generally located in integrated circuits near or on the detector, and it is desirable (for reasons of cost, reliability, and available space) to keep their lengths as short as possible, that is, to minimize the latency.

Events selected by level-1 trigger are read out from the front-end electronics systems into readout drivers and then into readout buffers where they are kept until the level-2 trigger decision.

The **level-2** trigger makes use of region-of-interest information provided by the level-1 trigger. This includes information of position and transverse momentum of candidate objects (high- p_T muons, electrons/ γ , hadrons/ τ , jets), and energy sums (missing- E_T vector and scalar E_T value). Using the region-of-interest information, the level-2 trigger selectively access for the readout buffers only the data that are required to make the level-2 decision. The level-2 trigger makes use of the precision muon chambers, the full calorimeter information and the inner detector data to provide additional rejection power. A latency time of a few ms is allowed to make the decision and reduce the rate to about 1 kHz.

After the level-2, the last stage of the online selection is performed by the Event Filter. It will employ offline algorithms and methods, adapted to the online environment, and use the most up to date calibration and alignment information and the magnetic field map. It will make the final selection of physics events which will be written to mass storage for subsequent full offline analysis; the output rate should be reduced to about 100 Hz, corresponding to an output data rate of about 100 MB/s if the full event data are to be recorded.

Chapter 2

The Pixel detector

2.1 Basic features of silicon detectors

A semiconductor detector is based on a pn junction [23] operated under a large reverse bias voltage. Fig. 2.1 shows a scheme of such a junction, assuming that the doping concentration N_A of the p -side is much larger of the n -side doping concentration N_D . A zone devoid of free charge carriers (electrons or holes) exists around the junction. This region is called *depleted zone* and it is the sensitive volume. Its depth (depletion depth) is inversely proportional to the doping concentration, so that if $N_A \gg N_D$ it extends mainly on the n -side (and vice versa). Fig. 2.1 shows the net charge density, the electric field and the electric potential as a function of the coordinate perpendicular to the pn interface. The total potential change is the bias voltage applied to the junction¹.

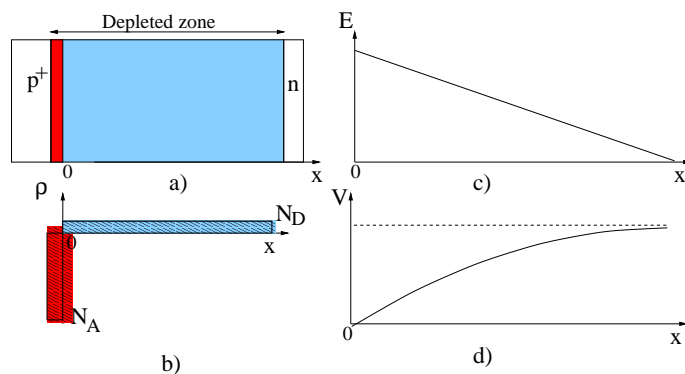


Figure 2.1: Scheme of a pn junction (a), with the charge density (b), the electric field (c) and the potential (d) distributions near the junction. N_A and N_D are the doping concentrations of the p -side and n -side respectively.

If a particle passes through the depleted zone, pairs of conduction electron and holes are created, and they drift toward the electrodes following the electric

¹An intrinsic potential difference is present even if no bias is applied; however it is much smaller than the reverse bias voltages used to operate particle detectors.

field inside the depletion zone. The mean energy required for the production of a pair in silicon is 3.6 eV, so that a minimum ionizing particle creates an average of 27000 pairs in 300 μm of silicon. The pairs are collected on the electrodes in a few ns.

The depleted zone thickness is given by [7]

$$d = \sqrt{\frac{2\epsilon_0\epsilon_{\text{Si}}V_{\text{bias}}}{eN_D}} \quad V_{\text{bias}} < V_{\text{dep}} \quad (2.1)$$

where e is the electron charge, N_D the silicon doping concentration, V_{bias} the applied bias voltage, ϵ_0 the vacuum dielectric constant and $\epsilon_{\text{Si}} = 11.9$ the silicon relative dielectric constant. V_{dep} is the voltage needed to extend the depletion depth to the full silicon thickness. Above this voltage the depletion is equal to the thickness no matter what the bias voltage is.

The depleted depth is proportional to the square root of the bias voltage, if a constant doping concentration is assumed. As the amount of charge collected depends on the sensitive depth, it is desirable to extend it over the whole sensor thickness. The bias voltage needed to deplete the whole silicon sensor thickness is called *depletion voltage*. The sensor thickness of ATLAS silicon detectors (SCT and pixel) is in the range $200 \div 300 \mu\text{m}$. Low doping concentrations (of the order of 10^{12} cm^{-3}) are used for the silicon substrate to reduce the depletion voltage, which is of the order of 100 V before radiation damage.

By segmenting an electrode in pixels, the pixels on which the signal is observed give the position of the passing particle. The spatial resolution is related to the pixel size and can be improved with charge interpolation.

A limit to the precision of the charge measurement comes from the electronic noise level. The major noise sources are related to the detector capacitance and leakage current, and the minimum electronic noise level for a particular detector can only be achieved by specifically designing the electronic readout circuit (input capacitance, shaping time, etc.).

2.2 Radiation damage in silicon detectors

Two different radiation damage effects in silicon detectors [24, 25, 26] have to be distinguished. The first effect is caused by ionization in the passivation layers at the detector surface and it is named surface damage. The other effect is bulk damage, which is caused by the non-ionizing energy loss of penetrating particles and results in crystal defects.

The surface damage results in an increase up to a saturation value of the charge accumulated at the interface between the silicon and the silicon oxide surface layer. The pixels can be electrically shortened by the presence of this conductive layer; a proper choice of the pixel isolation techniques (section 2.5) is needed to keep isolation throughout the radiation lifetime of the sensor.

The bulk damage is mainly caused by neutrons and charged hadrons, as the energy transfer of electrons and photons to crystal atoms is not enough to produce significant damage. The changes of the detector properties due to crystal defects scale with the non-ionizing energy losses. This has been verified by comparing the irradiation induced changes in the detector parameters for different particles and particle energies [28, 29, 30]. Therefore the bulk damage

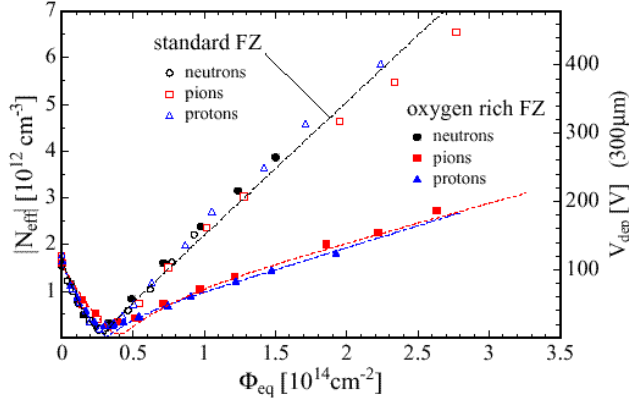


Figure 2.2: Effective impurity concentration as a function of the accumulated 1 MeV neutron equivalent fluence for standard and oxygen enriched silicon irradiated with reactor neutrons (Ljubljana), 23 GeV protons (CERN PS) and 192 MeV pions (PSI). The right scale reports the corresponding full depletion voltage for 300 μm thick sensors. [31]

is characterized in terms of the fluence of 1 MeV neutrons which gives the same non-ionizing energy loss.

The main effects of bulk damage which are relevant for silicon detectors operation are:

- The introduction of acceptor centres which changes the doping concentration with severe consequences for the operating voltage needed for total depletion.
- The creation of recombination/generation centres which leads to a fluence proportional increase of the leakage current.
- The formation of charge carriers trapping centres which affects the charge collection efficiency leading to a reduction in the signal height.

The first effect is the most severe, as the leakage current can be largely reduced by cooling the detectors and trapping has been found to be tolerable (chapter 4).

The effect of radiation on the effective doping concentration and on depletion voltage is shown in Fig. 2.2. Starting from n -type material, the increase in acceptor-like defects leads to a reduction of the effective doping concentration and depletion voltage for low fluences. At higher fluences the conduction type changes from n to p and an increase of the effective doping concentration and depletion voltage is observed. The depletion voltage eventually gets larger than the maximum practical operating voltage, and it is no more possible to fully deplete the sensors.

Fig. 2.2 also shows that radiation hardness of silicon detectors can be substantially improved by deliberately introducing oxygen to the substrate [31]. The improved radiation hardness is observed for detectors exposed to charged

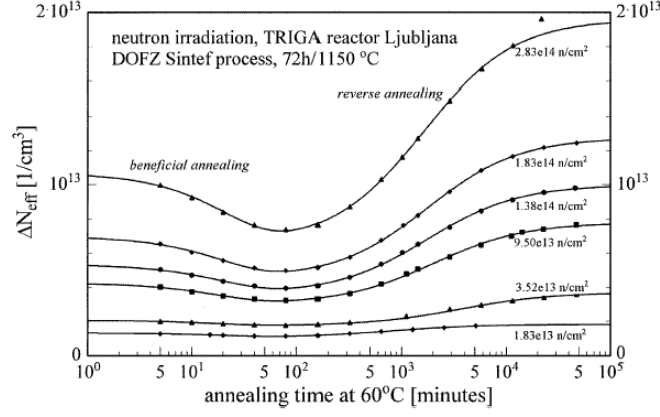


Figure 2.3: Systematic analysis of annealing data [31]. Change of effective doping concentration ΔN_{eff} during isothermal annealing at 60 ° of oxygen enriched silicon detectors irradiated with different neutron fluences.

hadrons (pions or protons) while no difference between standard and oxygenated silicon substrates is observed when the irradiation is made with neutrons. In the LHC both kinds of radiation will be present, the charged hadrons component being dominant for the innermost detector layers (that is, for the Pixel detector). For this reason, oxygenated silicon substrates have been adopted as a baseline for ATLAS Pixel sensors.

The effective doping concentration has a time dependence after irradiation [24, 25], which is caused by the interactions between the radiation-induced defects. This process is called *annealing*.

The damage-induced change in the effective doping concentration with respect to its initial value before irradiation can be described as

$$\Delta N_{\text{eff}}(\Phi_{\text{eq}}, t(T)) = N_A(\Phi_{\text{eq}}, t(T)) + N_C(\Phi_{\text{eq}}) + N_Y(\Phi_{\text{eq}}, t(T)) \quad (2.2)$$

In this equation, T is the temperature, t the time and Φ_{eq} the 1 MeV neutron equivalent fluence. It has been emphasized that the time dependence is subject to the annealing temperature T . ΔN_{eff} consists of three components:

- The short term radiation damage N_A , which decreases with a time constant in the range of days at room temperature. This beneficial annealing is due to recombination of charged impurities. Its time dependence can be described by a sum of exponentials [28]

$$N_A(\Phi_{\text{eq}}, t) = \Phi_{\text{eq}} \sum_j g_{A,j} \exp[-t/\tau_{A,j}(T)] \quad (2.3)$$

Each exponential describes a recombination process with time constant $\tau_{A,j}$ and weight $g_{A,j}$.

- An increase in acceptor states appears about two weeks after irradiation (room temperature). This long-term annealing described by N_Y is caused

by radiation-induced defects which are not electrically active themselves, but when they anneal combine to form a defect which is now electrically active and causes the observed time dependent change. It has been shown to be a second order process and can be suppressed by cooling the detector after irradiation [27]. It can be described with the formula [27, 33]

$$N_Y(\Phi_{\text{eq}}, t) = g_Y \Phi_{\text{eq}} [1 - 1/(1 + t/\tau_Y(T))] \quad (2.4)$$

The contribution of this term is zero for $t = 0$ while for $t = \infty$ it reaches the saturation value $g_Y \Phi_{\text{eq}}$.

- A stable damage part N_C . This depends on fluence only and it is the dominant component after about 10 days at room temperature, when most of beneficial annealing has already taken place and the reverse annealing has just started giving a significant contribution. Its dependence on fluence is similar to that of Fig. 2.2 and can be described by the formula [33, 34]

$$N_C(\Phi_{\text{eq}}) = N_{C0}(1 - \exp(-c\Phi_{\text{eq}})) + g_C \Phi_{\text{eq}} \quad (2.5)$$

For high fluences it increases almost linearly with fluence.

The constants $g_A, \tau_A, g_Y, \tau_Y, N_{C0}, c, g_C$ can be measured experimentally. Updated values for standard and oxygenated silicon can be found in Ref. [31, 35].

Fig. 2.3 [31] shows the effective doping concentration as a function of time for different fluences and for a temperature of 60 °C. The high temperature accelerates the annealing. Having measured the temperature dependence of the time constants [32] one can easily transfer the annealing function obtained at high temperature (for faster measurement) to any given value. With respect to a room temperature measurement this acceleration factor for the reverse annealing is 550 at 60 °C [31].

Oxygenated silicon not only exhibits a permanent damage (that is, a value of g_C) significantly lower than standard silicon for charged hadron irradiation, but also shows a significantly slower reverse annealing (a larger τ_Y). This offers an additional safety margin for detectors kept at room temperature for extended maintenance periods.

In order to minimize the damage due to reverse annealing it is foreseen to cool the detectors during and after operation periods and minimize the warm-up periods to a few days per year.

The increase of radiation induced leakage current with fluence is shown in Fig. 2.4. This results in increased electronics noise and power consumption. The reverse current depends on temperature according to the equation

$$I(T) \propto (kT)^2 e^{-E/2kT} \quad (2.6)$$

where k is the Boltzmann constant and $E = 1.21$ eV. Hence it can be greatly reduced by cooling the detectors.

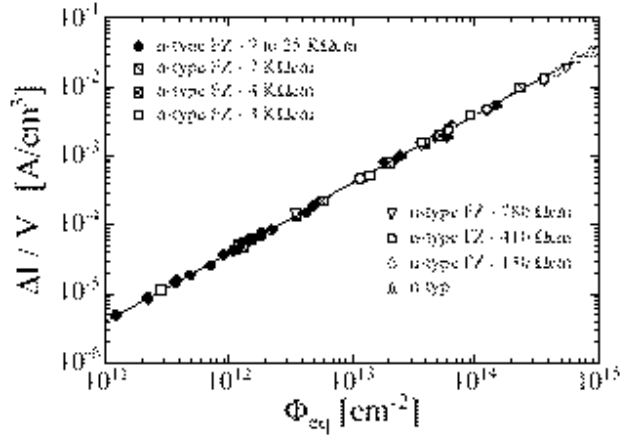


Figure 2.4: Fluence dependence of the leakage current generated per unit volume. Results for detectors produced by various process technologies from different silicon materials are reported. [31]

2.3 Layout

The Pixel Detector is designed to provide a very high granularity, high precision set of measurements as close to the interaction point as possible. The system is designed to provide three precision measurements over the full acceptance, and mostly determines the resolution on the impact parameter and the ability to find short lived particles such as B hadrons and τ leptons. The two dimensional segmentation of the sensors gives space points without any of the ambiguities associated with crossed strip geometries, and allows to reconstruct the z position of the primary interaction vertex (and of the secondary decay vertices as well).

A stereo view of the Pixel Detector is shown in Fig. 2.5. The detector² is composed by three barrel layers and three disks on each side. The barrel layers have average radii of 5.05 cm, 8.85 cm, and 12.25 cm, with an half-length of 40 cm. They are labelled B-Layer, Layer 1 and Layer 2 starting from the innermost one. The B-Layer radius has been chosen as small as possible (given the beam pipe constraints) to maximize the resolution on the impact parameter of tracks. The disks active region extends between radii 8.9 cm and 15.0 cm; the z positions are 49.5 cm, 58.0 cm and 65.0 cm. This geometry provides at least three points per track up to $|\eta| \simeq 2.5$ (Fig. 2.6).

The system is designed to be highly modular, containing approximately 2000 modules, which are identical in the barrel and in the disks. Each module is 62.4 mm long and 21.4 mm wide. The long side of the modules is along the z direction in the barrel and along the radial direction in the disks. Fig. 2.7 shows a cross section of the barrel Pixel Detector in the $R\phi$ plane. The detector modules are tilted in the $R\phi$ plane and the overlaps assure angular coverage for $p_T > 1$ GeV/ c . The tilt angles are 20° for all three layers. This choice is

²Here is described the June 2001 layout known as *Lund layout*, which is significantly different from the older layouts described in Ref. [20, 21, 6].

driven mainly by mechanical clearance constraints. The overlap is present also in the zR plane view. The tilt angle in the zR plane is 1.5° . Similarly the disk modules are mounted on both side of the disk support structure so that coverage is complete (the front and back faces of a disk module are offset in ϕ).

Fig. 2.8 shows the amount of material of the Pixel Detector crossed by a particle as a function of pseudorapidity. The number of radiation lengths seen by a particle before the electromagnetic calorimeter has to be kept as low as possible because it increases electron bremsstrahlung and photon conversions. The bremsstrahlung degrades the electron energy resolution provided by the calorimeter and the momentum resolution provided by the tracking system. In the most extreme cases (very hard and early bremsstrahlung) the electron track is not reconstructed at all and the particle is misidentified as a photon. The conversions reduce the photon detection efficiency and give rise to tracks with large impact parameters, affecting the b -jets tagging performance (chapter 8). The material increases with the absolute value of pseudorapidity because of the increase of the incidence angle in the barrel layers, and because of the services (cables, cooling system, support structures) located at the end of the detector. The asymmetry in the material and the peak at $\eta = 2.5$ are due to the B-Layer services which are placed on the positive η side. The option of having B-Layer services distributed symmetrically is under consideration.

The Pixel Detector is the innermost system, hence it will be exposed to the highest radiation levels (Fig. 1.7). The fluence to which the ATLAS Pixel Detector will be exposed was computed [21] assuming a pp inelastic interaction cross section of $\sigma = 80$ mb and a total of 100 days annual operation. At design luminosity ($10^{34} \text{ cm}^{-2}\text{s}^{-1}$) the B-Layer fluence will be about $\sim 0.3 \times 10^{15} \text{ n}_{\text{eq}}\text{cm}^{-2}/\text{year}$, the Layer 1 fluence will be $\sim 0.1 \times 10^{15} \text{ n}_{\text{eq}}\text{cm}^{-2}/\text{year}$, and the Layer 2 and disks fluence will be $\sim 0.05 \times 10^{15} \text{ n}_{\text{eq}}\text{cm}^{-2}/\text{year}$.

The specifications for the Pixel Detector require all the components to be

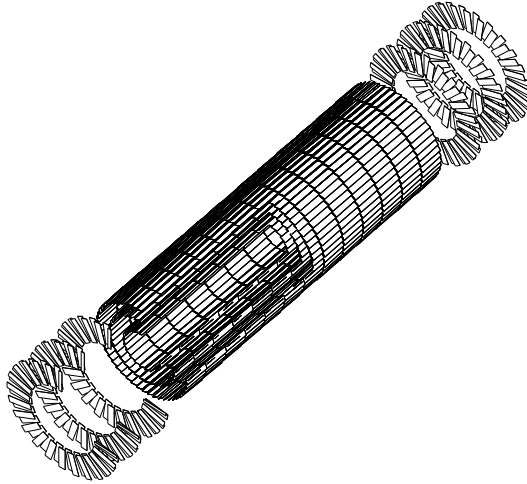


Figure 2.5: Stereo View of the Pixel Detector.

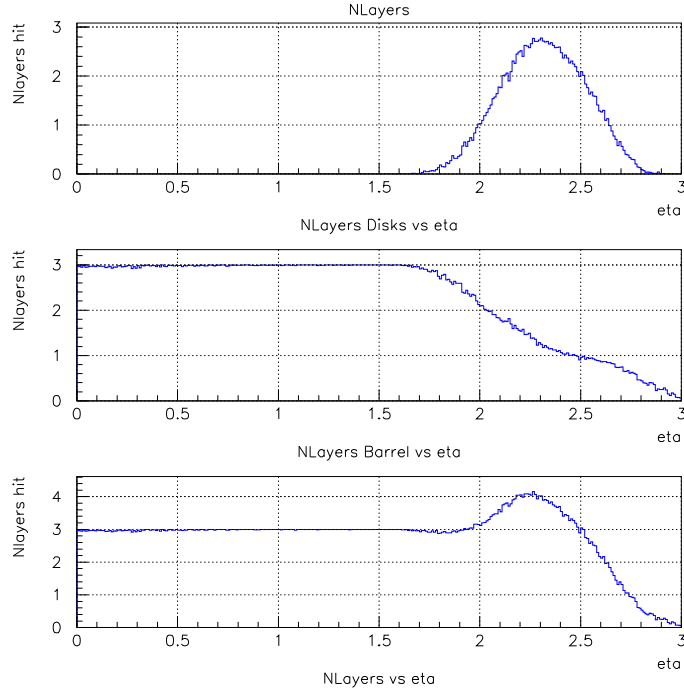


Figure 2.6: Mean number of Pixel layers crossed by 50 GeV muons as a function of pseudorapidity. Vertex spread due to the finite beam size is included.

radiation tolerant up to 10^{15} cm^{-2} fluence and 500 kGrays dose. Hence the B-Layer may need replacement after a few years of operation at design luminosity, while the other layers should be able to operate for the entire foreseen experiment lifetime (3 years at low luminosity plus 7 years at design luminosity) with a safety factor of ~ 1.5 for Layer 1. The safety factor protects the detector from the uncertainties on the pp cross section and the delivered luminosity profile.

The temperature of the Pixel Detector will be kept at 0°C to avoid reverse annealing effects, with only short warm-up periods for maintenance. The cooling system will have to keep that temperature in spite of the heat dissipation which will increase with time due to the increase of operational voltage and leakage current.

2.4 Modules

Each module is composed by a sensitive tile (the sensor), sixteen read out chips, and a flexible hybrid supporting a module controller chip, which performs clock and control operations, the local signal interconnection and power distribution busses and passive components such as temperature sensors, resistors and capacitors. The sensor is placed between the flexible hybrid and the integrated circuits chips. The module is mounted with the Front-End integrated circuits

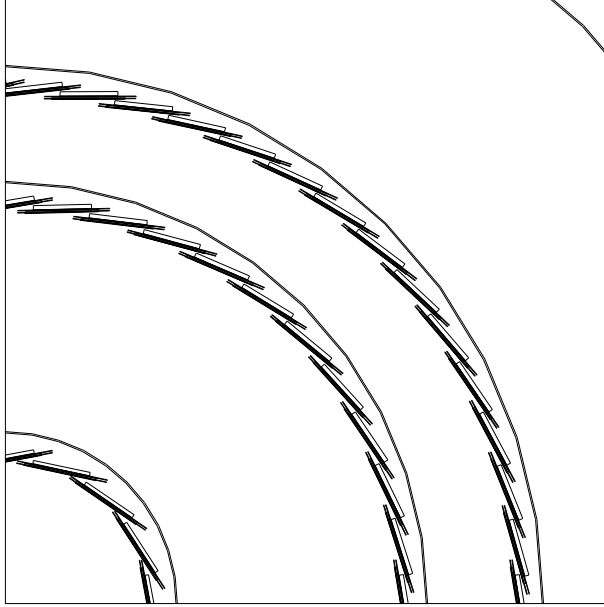


Figure 2.7: Cross section of the barrel Pixel Detector in the $R\phi$ plane.

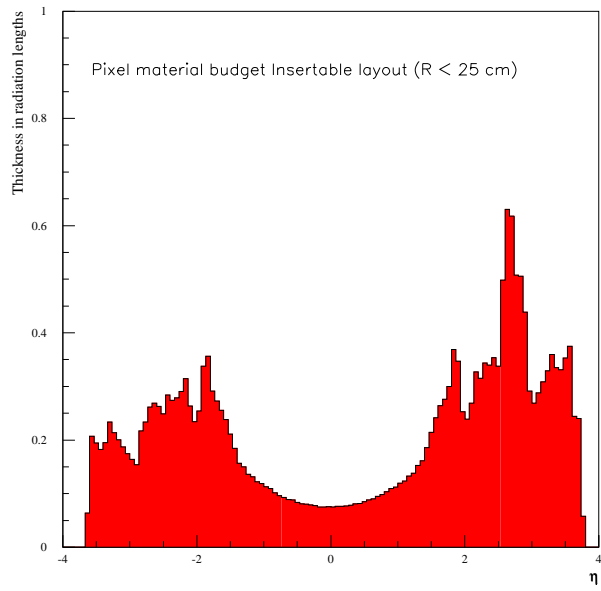
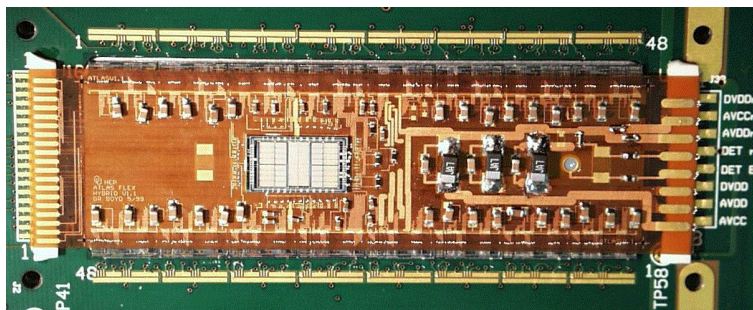


Figure 2.8: Amount of material of the Pixel Detector (in radiation lengths) as a function of pseudorapidity.

The Front-End integrated circuits extend beyond the long sides of the sensor. This gives access to their output pads so that wire bond connections can be used to make contact to the 18.6 mm wide Flex-hybrid glued to the back side of the sensor. Aluminum or copper bus lines route the signals to the Module Controller Chip (MCC) mounted on the Flex-hybrid. The MCC loads configuration data in the front-end chips, provides debugging and test functionalities for the entire module, distributes timing signals, coordinates the read-out from the 16 end-of-column logic circuits, builds the events and handles error conditions. Data are transmitted from the MCC to the Read Out Drivers (ROD) through optical fibers. Optical fibers are also used to bring signals to the module. There are two transmission and one reception fiber per module, all working in a digital mode. The opto-electronics package consists of two Vertical Cavity Surface Emitting Lasers (VCSELs) for outputs and one PIN diode for inputs.



A photograph of a flex is shown in Fig. 2.9. All module components and materials have to be radiation tolerant enough to survive over the operational lifetime of the detector.

A sensor (Fig. 2.10) consists of 328×144 pixel cells (328×192 in the B-Layer) of $50 \text{ } \mu\text{m} \times 400 \text{ } \mu\text{m}$ ($50 \text{ } \mu\text{m} \times 300 \text{ } \mu\text{m}$ in the B-Layer). It is connected to 2×8 read-out chips, each one reading an array of 164×18 pixels (164×24 in the B-Layer). The sensor sensitive area is $16.4 \text{ mm} \times 60.4 \text{ mm}$. The thickness is $250 \text{ } \mu\text{m}$ ($200 \text{ } \mu\text{m}$ in the B-Layer).

30

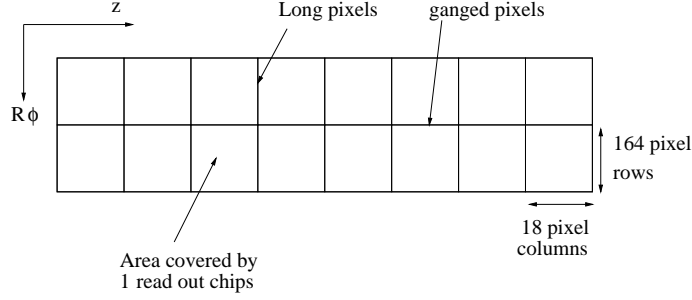


Figure 2.10: Schematic view of a sensor tile of barrel layers 1,2. The area read out by each of the 16 electronic chips is shown. In the B-Layer, the pixel cell size is reduced and the number of columns read out by a chip increases to 24. In the disks, the $R\phi$ coordinate replaces the z one.

obtained for the measurement in the $R\phi$ plane, at the cost of a poorer resolution on the z coordinate of vertices.

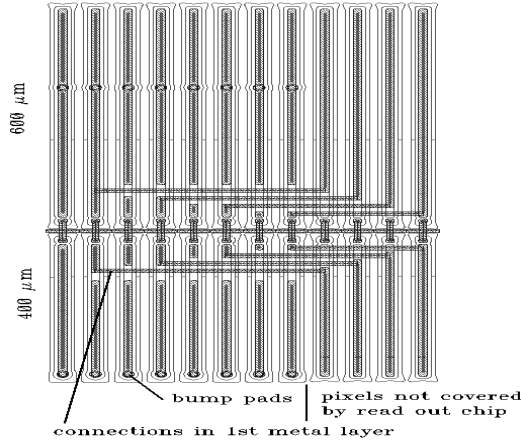


Figure 2.11: Detail of the corner of the sensor region covered by a read out chip, showing how coverage is achieved at chip borders. [20]

A region of width $400 \mu\text{m}$ at the borders between chips is not covered by readout cells. The solution is shown in Fig. 2.11 which shows a detail of the corner of the region covered by a read out chip. Complete coverage in z is achieved by increasing the length of the sensor pixels read out by the first and last column of each chip by $200 \mu\text{m}$. In the $R\phi$ direction, the pixels in the gap (4 rows for each chip) which are not bump-bonded to the electronics are connected to sensor pixels a few row away according to the scheme shown in Fig. 2.11.

A schematic cross section of ATLAS pixel sensors is shown in Fig. 2.12. The pixels are n^+ implants on an n substrate and the junction is initially located on the backside. The sensor must be operated fully depleted, as the undepleted zone on the pixel side would electrically shorten all the pixels. The pixels are

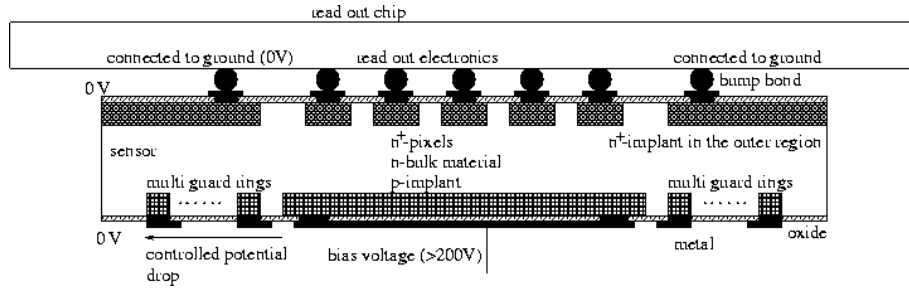


Figure 2.12: Cross section of a pixel sensor connected to a front-end chip.

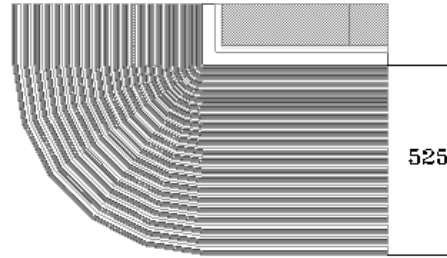


Figure 2.13: Structure in the p-side guard ring region [20].

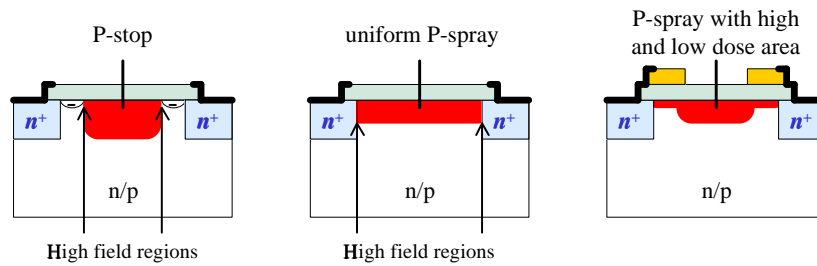


Figure 2.14: Pixel isolation techniques, from left to right: *p-stop*, standard *p-spray*, and moderated *p-spray*.

at ground potential, and a negative potential is applied on the backside. The electric field direction is such that the electrons migrate toward the pixels³. Each pixel is connected to a readout chain in the electronics chip. After type inversion of the substrate induced by radiation damage, the junction moves near the pixel implantation, allowing the detector operation also in partial depletion mode.

Due to the small gap between sensor and electronics (less than 20 μm), even a small potential difference between them could exceed the breakdown field in air of about 1.2 V/ μm and sparks could harm the electronics seriously. The whole outer region of the sensor's n -side is therefore covered by a n^+ implant held at ground externally. A controlled potential drop towards the cutting edge on the p side is ensured by a multiple guard ring structure shown in Fig. 2.13 and described in detail in Ref. [36]. The corners of all structures will be rounded to reduce electric fields.

The pixel implants must be electrically isolated from each other to prevent their being shortened by the electron accumulation layer at the Si-SiO₂ interface. The isolation techniques examined in the prototype program are the p -stop [37] and the p -spray [38] (Fig. 2.14).

The ATLAS prototype p -stop [39, 40] uses an heavily doped ($5.0 \times 10^{13} \text{ cm}^{-3}$) p -type implant (atoll) surrounding individual n^+ cells. On the p -spray devices [39, 40] a layer of p -type material is implanted on the entire n -side surface before other processing, then overcompensated where the n^+ pixel implants are needed. While both techniques provide effective isolation for implants in the low fluence regime, p -spray devices increase their resistance to radiation as their dose increases, due to the fact that developing oxide charge compensates the p -spray type, leading to progressively lower electric fields at $n-p$ boundaries as irradiation proceeds. Consequently the breakdown voltage of p -spray devices is at its minimum prior to irradiation and increases with radiation.

Two configurations of p -spray have been studied, in the first of these the dopant concentration is uniform ($3.5 \times 10^{12} \text{ cm}^{-3}$) over the whole sensor area. The value of the concentration is slightly higher than the saturation value of the surface oxide charge produced by irradiation, so that isolation is maintained regardless of the radiation fluence.

In the other configuration (known as *moderated p-spray*) the p -doping concentration is reduced to $1.5 \times 10^{12} \text{ cm}^{-3}$ in the region surrounding n^+ implants. In this way the capacitance between implants and the electric field at the interface from p -type to n^+ -type are reduced, increasing the breakdown voltage.

The p -stop sensors perform well before irradiation but proved not to be radiation hard [39, 40, 41] and hence are not suited for operation in the ATLAS environment. The moderated p -spray concept was selected; it was preferred against the uniform p -spray isolation because of the higher breakdown voltage before irradiation [40].

The p -spray technique allows the introduction of a bias grid. The bias grid is a network of bus lines, one between every other column pair of pixels. In the final design (Fig. 2.15) an n^+ dot implant integrated in each pixel is connected with the bias grid via a metal line. When voltage is applied to the grid, it reaches each pixel by punchthrough through the corresponding dot. This is useful for sensor testing prior to connection to front-end electronics through

³The SCT detector uses p strips on an n substrate and collects holes.

bump-bonding. The bias grid is implemented every 2nd column, providing an equal potential to every pixel cell during testing; it is inactive during normal operation, but keeps a pixel close to ground potential in the case that a bump may be missing.

Various pixel sensor geometries have been fabricated and studied. They will be described in chapter 3 and their performance discussed all along this thesis.

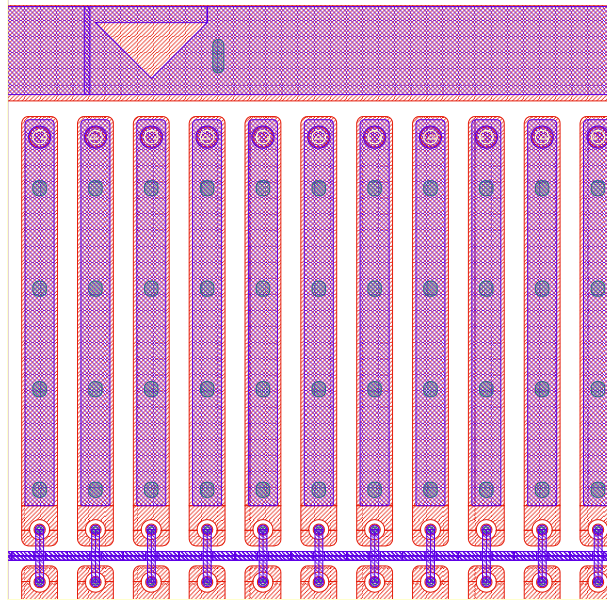


Figure 2.15: The Small Dots (SMD) design. This is the design selected for ATLAS Pixel sensors.

In the final design (Fig. 2.15) each pixel consists of one rectangular n^+ implantation of dimensions $30\text{ }\mu\text{m} \times 382.5\text{ }\mu\text{m}$. The gap between two adjacent pixel is $20\text{ }\mu\text{m}$ in the short pitch direction, $15\text{ }\mu\text{m}$ in the long pitch direction at the pixel side with the bump-pad and $20\text{ }\mu\text{m}$ at the other pixel side where the bias grid is located. The bias-grid connection to each pixel is provided using a round n^+ -implant integrated in the n^+ -pixel implant with $10\text{ }\mu\text{m}$ diameter and $5\text{ }\mu\text{m}$ gap. The bias-dots of all pixels within an adjacent pair of columns are connected via a metal line to the outer n^+ -implantation which surrounds the border of the active sensor area.

The ATLAS sensor will use oxygenated substrates. Fig. 2.16 [31] shows the expected depletion depth of the B-Layer as a function of time since the beginning of LHC operation, assuming that design luminosity will be reached after 3 years. It can be seen that the maximum operation voltage of 600 V would allow to operate standard detectors fully depleted for only 3 years, while oxygenated detectors could be operated fully depleted for almost the full 10 years period. However the B-Layer may still need replacement, as the electronics and the other detector components are only required to resist the dose and fluence which will be reached after the first 5 years.

The advantage of using oxygenated sensors is less pronounced (but still size-

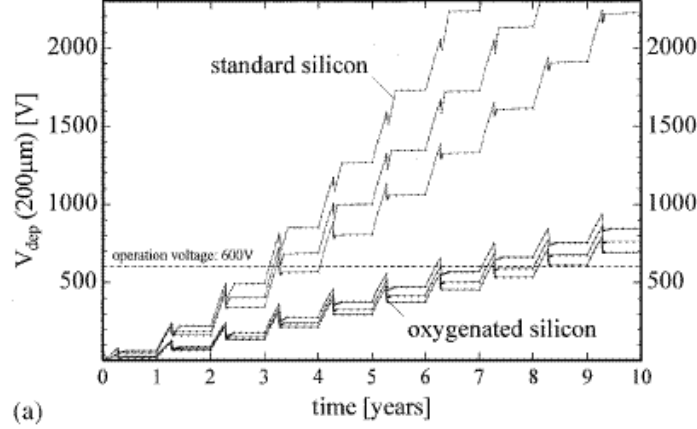


Figure 2.16: Depletion voltage of the B-Layer as a function of time, for not oxygenated and oxygenated sensors [31]. The different curves for each type of sensors differ for the assumed duration of warm-up periods.

able) for the SCT microstrip detectors, as at large radii a significant contribution to the total fluence comes from neutrons rather than from charged hadrons from the interaction point.

2.6 The front-end electronics

The read out integrated circuits provide individual circuits for each sensor pixel element. The readout chips are positioned on the top of the sensor and each readout cell is connected to the sensor pixel via bump-bonding [21] (Fig. 2.12).

The bumping process requires the deposition of metals on the aluminum pads of either the silicon sensor wafers, the integrated circuit wafers or both types of wafers. Then the integrated circuit die has to be mounted onto the silicon sensor substrate. This process is called flip-chip and requires few μm placement precision and the pressure or heat that is needed to form or initiate the bond.

Two processes of bump-bonding have been investigated. In the first, indium bumps are deposited on both (sensor and IC) wafer types. The flip-chip is performed with a moderate heating (Fig. 2.17): the bumps are accurately aligned and then joined under pressure. In the second process, solder bumps are deposited on the electronics wafer with the other one having only thin metal pads. Then the two wafers are joined and electrical connection is obtained reflowing the solder at the fusion temperature of the PbSn alloy.

Two separate front-end chips were produced in the initial phase of the electronics demonstrator program, the FE-A [42, 43] and the FE-B [44]. Although conceived with radiation-hard process in mind they were realized at non-radiation hard foundries. An other difference with the final design was a limited End of Column (EoC) buffer size which allowed some extra circuitry for diagnostic purposes which should not be needed in the final design. The FE-A used some bipolar transistor; a 100% CMOS version, called FE-C was

later produced.

The next version (FE-D) was radiation-hard but still did not meet ATLAS specifications. The final design (FE-I), based on deep submicron technology, is currently being worked out.

The design of the FE-B electronics chips will be discussed in more detail, as the assemblies whose analysis is presented in this thesis make use of it. Many of the concepts implemented in FE-A/C and FE-B prototype chips will be present also in the final design.

The FE-B. Each cell provides amplification and shaping of the input signal. The need of reducing the B-Layer occupancy at high luminosity lead to a design which reduces the cross-talk between pixels. The preamplifier was thus chosen as fast as possible given the available power budget, with a peaking time of about 20 ns with no external load. It is followed by an AC-coupled differential amplifier with a slower peaking time; this suppressed the fast signal induced by the cross-talk. The DC-feedback current determines the return-to-baseline time of the preamplifier which ranges from 100 ns to several μ s. This time can be adjusted by tuning the feedback current to achieve the best dynamic range for the measurement of the time spent by the signal above the threshold. The Time Over Threshold (TOT) provides a 7-bit information which allows to measure the charge collected by the pixel. If more than a pixel collects the charge released in the sensor by the passing particle, charge interpolation can be used for a better reconstruction of the pixel cluster position. The ToT is calibrated by injecting a known charge into every channel, with an accuracy of the order of 10%. An example of calibration plot of a FE-B chip is shown in Fig. 2.19.

The discriminator has two threshold. The fast and low threshold is used

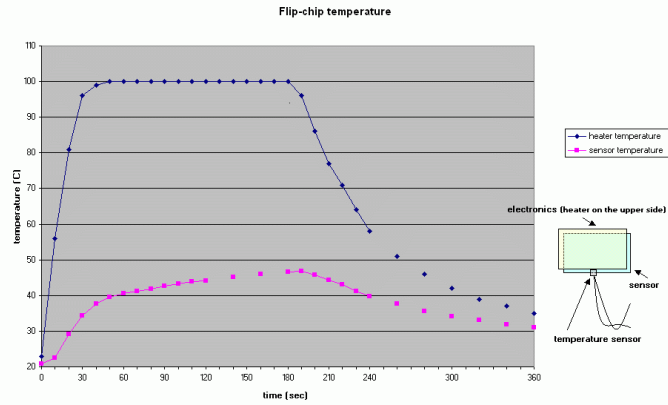


Figure 2.17: Temperature monitoring during the indium flip-chip process. The upper curve is the temperature of the heater, placed on the top of the electronics chip, as a function of time. The lower curve is the temperature measured on the edge of the sensor.

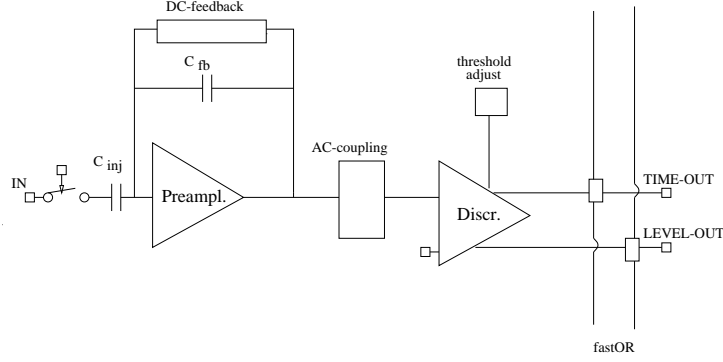


Figure 2.18: Block diagram for the Front End of FEB .

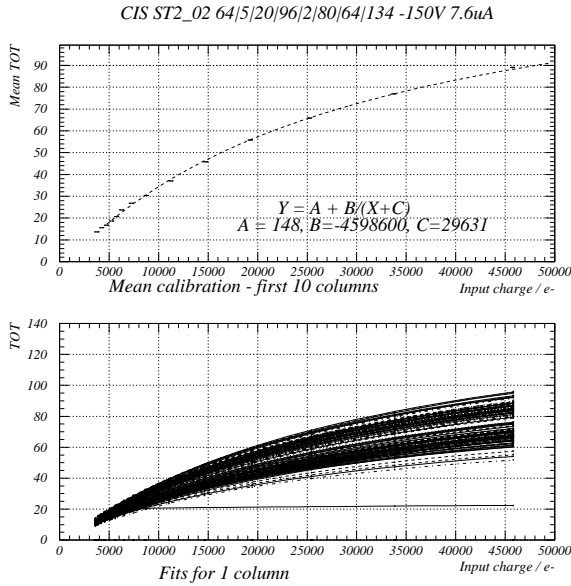


Figure 2.19: Calibrations plots for an ST2 sensor equipped with a FE-B chip, with one of the DAC settings used in the test beam .

for the TOT measurement, providing the times of the leading edges (LE) and trailing edges (TE) of pulses. The slower and higher threshold is used to accept an hit. A 3-bit current-mode DAC is placed in each pixel cell and operates at the level of the differential amplifier baseline to optimize the threshold of individual pixels providing a means of overall threshold dispersion reduction. Figure 2.20 shows an example of threshold and noise distributions of a FE-B chip.

During the operation in the test beam the thresholds of the individual channels were adjusted achieving a threshold dispersion of $120 e^-$ rms. Typical thresholds were around 3000 electrons, lowered to 2000 electrons for the charge collection studies. Typical noises of the not irradiated assemblies were $110 e^-$ for ST1 and ST2, $170 e^-$ for SSG.

Also featured is a global hit-OR (hitbus) which provides for a means of self-triggering operation. A 2880-bit (the number of pixels in a chip) pixel register

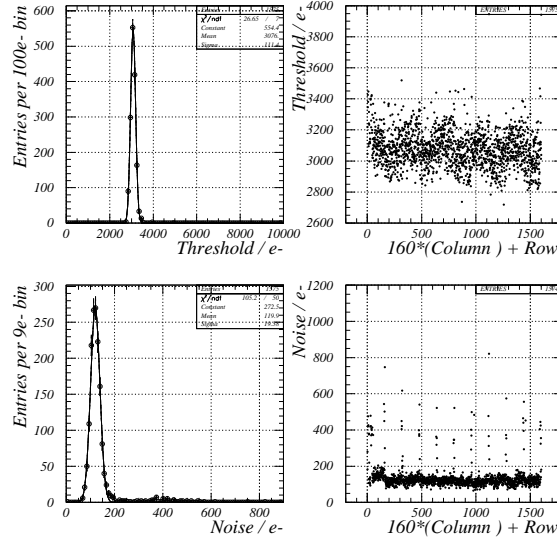


Figure 2.20: Threshold and noise distributions (left) and as a function of channel number (right) for an ST2 sensor equipped with a FE-B chip, with one of the DAC settings used in the test beam .

plus one corresponding latch per channel enable individual pixels to be masked-off for (independently) calibration-strobing and readout.

In FE-B the global time information is distributed throughout the array to every pixel as 7-bit Gray code. When a hit is tagged in a pixel cell the timestamps for the LE and TE are stored locally. Meanwhile a continuous vertical sparse scan operates along the column pairs seeking tagged hits. As soon as such a hit is seen, the geographical and timing information is sent directly to the 20 buffer-sets which are resident at the end of each column pair. Upon receipt of a level-1 trigger, a two dimensional horizontal sparse scan looks through the EoC buffers for hits which match in time. Matching hits are then stacked up in a readout-FIFO for subsequent serial transmission to the Module Controller Chip. The ToT is calculated for each hit as the LE-TE time difference prior to this, resulting in a 7-bit charge field in each 26-bit hit word.

The hit word has the following format: 1 header bit, 4 trigger number bits (these allow to uniquely label up to 16 events stored in the EoC buffer awaiting readout into the MCC), 8 row number or end-of-event/warning bits, 5 column number bits and 8 Time Over Threshold bits (of these, only 7 bits are actually used in the FE-B). For each event, an end-of-event word is always added.

The FE-A/C. The other design has a markedly different readout architecture implementation. In FE-A/C each column-pair is served by an 80-bit 40 MHz shift register to clock LE and TE hit-information towards the EoC circuitry. There the timestamps of the hits are determined from the row number information along with the time of arrival at the EoC. Given the length of the shift registers only one LE or TE from a 4-pixel cell may be introduced for a given BCO. If an hit occurs while the shift register is occupied by an address traveling down, its information is kept until the next available crossing and a

2-bit late-field is used to indicate the required correction to the hit age at the EoC.

The FE-I. The 0.25μ technology used for the FE-I chips allows to fit the more circuitry in less space. The FE-I chips have 64 end-of-column buffers (compared to the 20 buffers of the FE-B) which are enough to cope with the B-Layer occupancy at the LHC design luminosity. A total of 14 configuration bits are available at the pixel level, including 5 bits for threshold tuning and 5 bits for feedback current tuning. One more bit is allocated for the timestamps. As the time is measured in units of the 25 ns bunch crossing, the 8-bits timestamps allow for a level-1 trigger latency of $6.4\mu\text{s}$.

Chapter 3

Test Beam setup and tested devices

Prototypes of ATLAS Pixel modules have been developed and tested with a particle beam in order to assess the performance of different designs in conditions as close as possible to those of the final experiment. This chapter describes the test beam setup, the processing of raw data by the event reconstruction program and the designs of tested devices.

Three kinds of assemblies have been tested:

- Single chips assemblies, consisting of one front-end chip integrated on a $\sim 0.6 \text{ cm}^2$ sensor.
- 16-chip modules, consisting of 16 front-end chips integrated on a $\sim 10 \text{ cm}^2$ sensor (the same size of ATLAS sensor tiles) and a Module Controller Circuit (MCC) integrated outside the module.
- ATLAS modules (as the 16-chips modules, but with the MCC integrated on the module).

This thesis deals with data taken with single chip assemblies in the years 1998-2001.

3.1 Test Beam setup

Test beam studies of ATLAS Pixel detector prototypes have been performed using the H8 beam facility in the North Area at CERN. At this facility 450 GeV protons from the SPS accelerator are delivered to a target to produce secondary beams. Different particles over wide momentum and intensity ranges can be selected; most of the data of Pixel test beams were taken with pion beams of 180 GeV/ c momentum. The beam intensity was $\sim 2 \times 10^4 \text{ cm}^{-2}$ per burst (2 s out of 14 s).

The Marseille telescope (1998-2000) The test beam setup of 1998 included a telescope of four silicon microstrip detector doublets mounted on a table, two downstream and two upstream of a central part which can fit up to three pixel detector under study. A drawing of this setup is shown in Fig. 3.1.

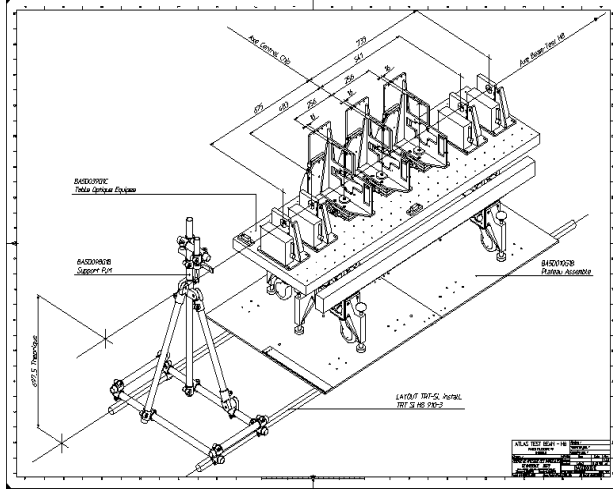


Figure 3.1: Pixel detector test set-up in the CERN H8 area (picture from [21]).

Each microstrip doublet consisted of a pair of silicon microstrip sensors with $50\text{ }\mu\text{m}$ pitch, 384 strips each and mounted in orthogonal directions. They had analogue read-out providing a point resolution of $\sim 3\text{ }\mu\text{m}$.

The following reference system is used for the test beam data: the z axis is along the beam, the x axis horizontally and the y axis vertically. A local reference frame is defined for the pixel detector, with the x_{loc} axis along the short pixel dimension, the y_{loc} axis along the long pixel dimension and the z_{loc} axis along the normal to the pixel plane.

The pixel detectors were mounted on a rotating platform allowing to select the angle between the normal to the pixel plane and the beam axis both in the xz plane and in the yz view. The two angles are called Θ and ϕ respectively.

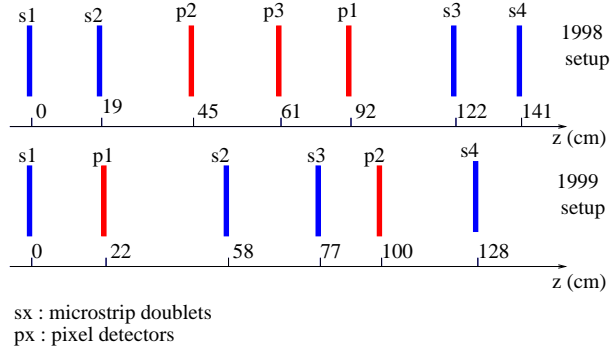


Figure 3.2: Comparison between 1998 and 1999 setups.

In 1999 the setup was changed to improve the position resolution of tracks projected onto the tested devices. Fig. 3.2 compares the position of microstrip

doublets and pixel detectors in 1998 and 1999 setups. In the latter only the first pixel detector can be tilted allowing selection of incidence angle. The 1999 setup was kept also in 2000.

The Bonn telescope (2001) In the test beam of year 2001 a new telescope was implemented. This telescope used double-side strip detectors thus introducing less material than the Marseille telescope which used two orthogonal strip detectors to measure a point of the track. The strip pitch was the same, $50\ \mu\text{m}$, and the spatial resolution was comparable to that of the old telescope. The new telescope offered a trigger rate capability of 7000 Hz to be compared to the old telescope rate of about 300 Hz, because of the shorter dead time due to the faster readout. This was the main motivation to move to the new set-up. The higher trigger rate was achieved introducing module buffering capability and reading only the strip data of interest (that is, the strips over threshold and the nearby ones) instead of reading the signal of all channels as in the old telescope.

Two scintillators and one silicon pin diode ($5\ \text{mm} \times 5\ \text{mm}$ active area) were used for triggering purposes. The beam passage time reference was given by the scintillator, while the diode signal selected tracks known to pass through the pixel array.

A TDC measured the time difference between the trigger and a free-running 40 MHz clock. The TDC information was used to select those particles in time coincidence with the clock and allowed simulation of the LHC operating conditions where all the particles will be synchronized with the 40 MHz clock. Further, for an accepted trigger of beam particle crossing the detector, up to 16 level-1 triggers continuous in time were sent to the front-end chip and were subsequently read out to simulate a sequence of 16 bunch crossings; this allowed to study the timing behaviour of the detector.

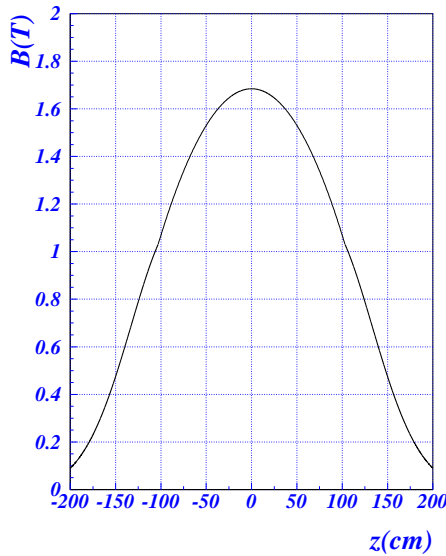


Figure 3.3: Magnetic field profile along the axis of the *Morpurgo* magnet, when operated with the maximum current of 5000 A [45].

The setup was put inside a magnet which provided a magnetic field up to 1.67 T. The magnetic field was along the long direction of the pixels as it will be in the barrel part of the ATLAS Pixel detector. Data both with and without magnetic field were taken. The magnetic field profile along the magnet axis is reported in Fig. 3.3. In the test beam the first and last strip doublets were respectively at about 140 cm and 10 cm from the magnet centre, so the magnetic field varied significantly along the telescope. The determination of the exact telescope position inside the magnet is described in chapter 6.

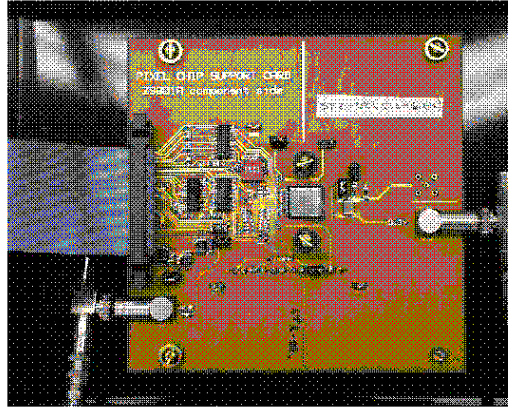


Figure 3.4: Photograph of a single chip board. The chip is the square at the centre of the board.

The single-chip assemblies, 16-chip and ATLAS modules were mounted on different boards which had a common interface to the read-out system. These cards also provided mechanical support and heat sinking for the modules, the bias voltage and power connections, the line decoupling capacitors, and load resistors. Data transmission used copper lines instead of optical fibers. The board for single chips is shown in Fig. 3.4.

Pixel assemblies with irradiated sensors were kept at a temperature of -9°C to reduce annealing effects (section 2.2).

The read-out chain for all prototypes consisted of three elements, which are briefly described below:

- A DSP interface: a VME module which provided 32 data lines and 12 address lines and controlled the lower level boards described below.
- A Pixel Low Level Card (PLLC) which provided the interface to DSP for serial command processing in the front-end and module control chips. It performed data decoding for the returned serial data stream, hardware histogramming capabilities for fast scans of thresholds, timewalk and charge gain, and strobe/trigger generation capabilities.
- A Pixel Control Card which provided I/V supply and monitoring under external control, 12-bit DAC for front-end chip control, differential drivers/receivers for digital signals from the PLLC and for LVDS from

the support card, clock regeneration and re-synchronization of fast signals with the 40 MHz clock, including strobe delay fine adjustment.

3.2 Data analysis and alignment

Test beam raw data are processed by a program [46] which performs event reconstruction and alignment.

The reconstruction program looks for and masks strips with too many hits (hot strips). Then it reconstructs the clusters in the eight strip planes. The position of the clusters with more than one strip is determined by the two adjacent strips with the highest charge¹. The position of these strips is interpolated using their charges with an algorithm [47] which corrects the nonlinearities in the strip response requiring a uniform distribution of the tracks across each strip.

The strip hits are fitted with a parabola (in presence of magnetic field) or with a straight line (when no field is present). The parabola is a very good approximation of the circumference followed by the pions in the magnetic field. The first of the neglected terms is of the order of L^4/R^3 where L is the telescope length and R is the curvature radius. With $L = 1.4$ m and $R = p/eB \simeq 400$ m (p is the beam momentum) this term is $0.06 \mu\text{m}$. For each strip plane the residuals between the hits and the fitted track extrapolated to that plane are computed. The strip planes and the pixel detectors are then aligned with an analytical algorithm which minimizes in both views (xz and yz) the residuals and their dependence on the track transversal position and angle. The first strip is used as reference plane; the distance between the first and last strip plane is also fixed, providing the length scale for the system. First the strip planes are aligned (and tilt angle determined) with respect to the first plane. The pixel chips are then aligned relative to the strips. There is a residual unknown variable: the angle between the x and y strips of the first strip doublet. This is solved using the pixel detector which by construction measures two orthogonal coordinates.

The events which have one and only one track reconstructed in both views are kept.

A number of additional requirements were applied in the analysis presented in the following chapters. Tracks were required to extrapolate into a fiducial region inside the pixel sensor. This was defined as the region within $40 \mu\text{m}$ from the edge of the pixel sensor for perpendicular tracks or at least $40 + t \times \tan \alpha \mu\text{m}$ where t is the sensor thickness and α the incidence angle (such that $\alpha = 0^\circ$ is normal incidence).

In addition, only events with track reconstruction χ^2 -probability value of more than 0.02 in both views were kept. Pixel clusters were constructed in the following way:

- all pixel hits were considered independent of track extrapolations;
- all adjacent hits were clustered together.

For irradiated sensors at large incident angles, the clustering algorithm allowed for the presence of not-hit pixels within a cluster.

¹If the two strips with highest charge are not adjacent only the strip with maximum charge is considered.

The cluster position was then evaluated as described in chapter 7.

To associate a cluster to a beam particle track the residual between track extrapolation and mean cluster position was required to be less than $100\text{ }\mu\text{m}$ in the short pixel dimension and $800\text{ }\mu\text{m}$ in the long pixel dimension. Clusters and events that passed all the above requirements were used in the measurements reported in this thesis².

3.3 Tested devices

The first test beams at CERN were performed in 1997. The analysis of the data collected in 1997 and April 1998 is discussed in [21]. This thesis presents the analysis of most of the data taken with single chip sensors in the years 1998-2001.

Sensor designs

A detailed description of the ATLAS pixel sensors have been made in section 2.5; here only the differences between the designs of the tested sensors are discussed.

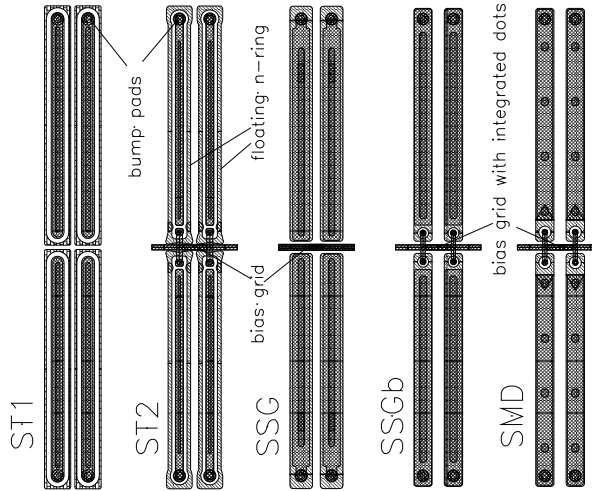


Figure 3.5: Tested sensor design options [40].

The tested sensors incorporated various geometries (Fig. 3.5) developed to study and thus optimize the performance in terms of interpixel capacitance, cross-talk, noise, efficiency and intrinsic resolution.

The **Single Tile 1 (ST1)**³ design uses *p-stop* isolation, while all the other designs use *p-spray* isolation. The p^+ -type isolation rings surround the n^+ -pixel implants. No bias grid is present.

²In the efficiency measurements also events with no pixel hits or an hit far from extrapolation point are considered.

³The name is because this design was implemented also in some of the sensor tiles, the size of an ATLAS module, bump-bonded to an array of 8×2 FE chips.

In the **Single Tile 2 (ST2)** design *p-spray* isolation is used, but there are n^+ -type ring-like structures around each pixel to reduce inter-pixel capacitance. A bias grid is also present.

Single Small Gap (SSG) uses *p-spray* isolation but does not include any intermediate n^+ structures. Neighbouring pixels merely have small gaps between them. A bias grid is implemented.

ST1, ST2 and SSG sensors were tested in 1998. The ST1 design performed well before irradiation, but the *p-stop* technique proved not to be radiation-hard [40, 41], while the *p-spray* one was. ST2 sensors had a charge collection inefficiency related to the presence of the n^+ rings. SSG sensors had performances similar to those of the ST1 design for what concerns charge collection (chapter 4) and they were also resistant to radiation so they were selected as baseline, after some modification in the bias grid region (SSGb design, tested in 1999) to further improve charge collection efficiency (section 4.1). In a subsequent sensor production this SSGb design was labeled SMD (SMall Dots).

The ATLAS Pixel sensors baseline implement the SMD design [40], which has been described in some detail in section 2.5 and it is shown in Fig. 2.15.

Two variations of the SMD design, called NOD (NO Dots), and LAD (Large Dots) were tested in 2000 and 2001. They are shown in Fig. 3.6 and 3.7 respectively. The NOD design has no integrated dots, and the bias reaches the implant directly from the neighbouring bus line. The LAD design has dots with a diameter of $15\ \mu\text{m}$ (to be compared with the $10\ \mu\text{m}$ dot diameter of the SMD design).

A bricked design was also studied. In this design the $400\ \mu\text{m}$ long pixel cells in adjacent columns are staggered by $200\ \mu\text{m}$ in the long direction of the cell. This design allows to improve the resolution in the long direction of the pixel cell (section 7.6).

When results on the radiation hardness of oxygenated silicon became available [31] some SMD, LAD and NOD sensors were fabricated using this technique to decrease the depletion voltage after irradiation. Oxygenated wafers with concentrations ranging from $2 \times 10^{17}\ \text{cm}^{-3}$ to $4 \times 10^{17}\ \text{cm}^{-3}$ were examined. The oxygen enhancement was achieved by immersing the wafer for 24 hours in a $1150\ ^\circ\text{C}$ oxygen atmosphere prior to processing. Standard and oxygenated SMD, LAD and NOD sensors were tested in the test beams of 2000 and 2001.

The substrates of all the sensors whose analysis is discussed in this thesis had $\langle 111 \rangle$ crystal orientation.

Irradiated sensors

In order to characterize irradiated sensors with pixel readout electronics, indium bumps were deposited on some single chip sensors which were then exposed to fluences comparable to those expected at the LHC. The irradiations were performed using the $300\ \text{MeV}/c$ pion beam at PSI and the $55\ \text{MeV}/c$ proton beam at LBNL. After irradiating these devices, they were flip chipped to the front end electronics. Since indium bumps need only a limited heating (Fig. 2.17) for flip chipping, this process was used to limit the annealing process.

ST1 and ST2 sensors were irradiated to 0.5×10^{15} and $10^{15}\ \text{neqcm}^{-2}$ fluence and studied in the test beams of 1998 and 1999. ST1 sensors, which had *p-stop* isolation produced high noise even at low bias voltages [40, 41], while devices

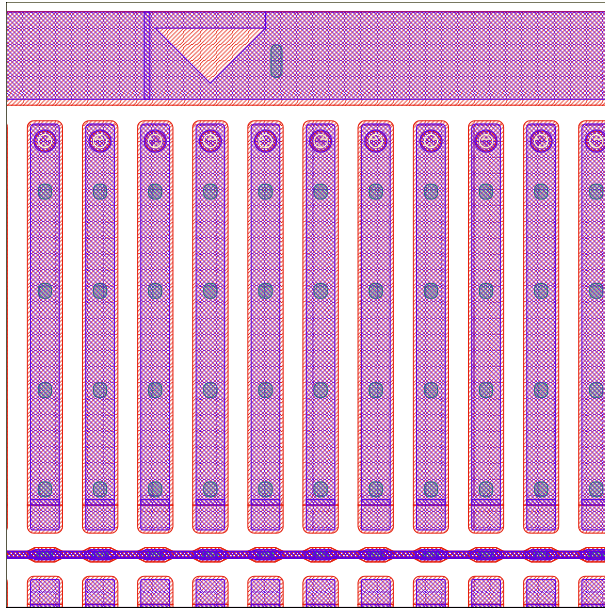


Figure 3.6: Layout of the NOD (NO Dots) design.

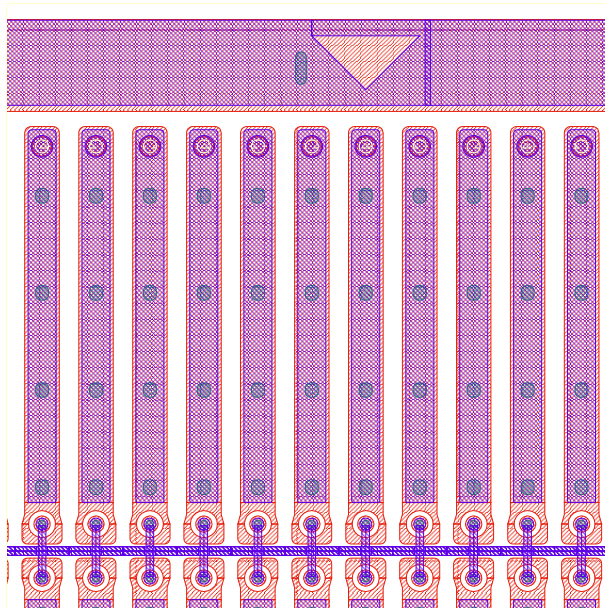


Figure 3.7: Layout of the LAD (Large Dots) design.

with *p-spray* isolation performed well at voltages of up to 600 V, so the *p-spray* technique was chosen and used in all following sensor designs.

In year 2000 and 2001 sensors exploiting the new designs (SMD, NOD and LAD), with oxygenated and not oxygenated substrates and irradiated to various fluences were studied. A list of the tested devices is reported in table 3.1.

Data taken in these two years were affected by electronics readout problems because of a large cross-coupling from the digital circuitry to the analogue front-end through the detector substrate. This problem was not so severe in the previous years, when the bump-bonding was made by an other firm. The problems have been understood and are not expected to be present for devices with the final rad-hard electronics chip, which will be available for the 2002 test beam.

Table 3.1 lists the devices whose analysis is presented in the following chapters. A complete list of the devices tested on beam can be found on the web [48].

| Sensor | Oxy | Fluence ($\text{n}_{\text{eq}}\text{cm}^{-2}$) | Thickness (μm) | years |
|---------|-----|--|-----------------------------|-----------|
| ST1 | No | 0 | 280 | 1998 |
| ST2 | No | 0 | 280 | 1998 |
| SSG | No | 0 | 280 | 1998 |
| bricked | No | 0 | 280 | 1998 |
| ST2 | No | 0.5×10^{15} | 280 | 1998,1999 |
| ST2 | No | 10^{15} | 280 | 1998,1999 |
| SSG1b | No | 0 | 200 | 1999 |
| NOD | Yes | 0.32×10^{15} | 250 | 2000 |
| SMD | No | 0.32×10^{15} | 250 | 2000 |
| SMD | Yes | 0.32×10^{15} | 250 | 2000 |
| SMD | No | 0.56×10^{15} | 250 | 2000 |
| SMD | Yes | 0.56×10^{15} | 250 | 2000,2001 |
| SMD | Yes | 10^{15} | 250 | 2000,2001 |
| LAD | Yes | 0.3×10^{15} | 250 | 2001 |
| SMD | Yes | 0.5×10^{15} | 250 | 2001 |

Table 3.1: Properties of the devices studied. The *Oxy* column indicates whether a sensor is fabricated with oxygenated silicon substrate. The ST1 sensor had p-stop isolation, all the others had p-spray isolation. The crystal orientation is $\langle 111 \rangle$ for all the devices.

Most of the irradiated sensors were kept at low temperature to suppress annealing. The oxygenated sensor irradiated to $0.3 \times 10^{15} \text{ n}_{\text{eq}}\text{cm}^{-2}$ was exposed for 37 days at room temperature (25 °C) before the test beam measurements. Similarly, the oxygenated sensor irradiated to $0.5 \times 10^{15} \text{ n}_{\text{eq}}\text{cm}^{-2}$ was exposed for about 90 days at the same temperature before the test beam.

Chapter 4

Efficiency and charge collection studies

4.1 Charge collection

A uniform and efficient collection of the charge released by the passing particles in the silicon sensors is important to ensure good pixel performances. The presence of regions of the pixel cell with reduced charge collection results in a poorer efficiency and spatial resolution [49, 50].

The ability of the front-end electronics to measure the charge collected by every pixel cell using the Time Over Threshold technique and the tracking of particles by the microstrip telescope gave the possibility to measure the charge collected as a function of the impact point of traversing particles relative to the center of a pair of pixel cells. This analysis allowed to study the charge collection properties of sensors with different designs (Fig. 3.5), spot the regions with a lower charge collection and relate them to specific features of the design, which could then be optimized.

It was also possible to study the effects of radiation damage on the charge collection properties.

4.1.1 Unirradiated sensors

Data with the beam perpendicular to the sensor plane were considered. For a particle crossing the detector near the pixel centre all the charge is collected on a single pixel, otherwise the charge is shared between several adjacent pixels; in this case the sum of pulse heights is calculated and defined as cluster pulse height.

The upper part of Fig. 4.1 shows the average cluster charge as a function of positions x and y inside a pair of pixel cells. For every bin in the x - y plane the average of the cluster charge is evaluated and plotted. The coordinate axes are parallel to the short ($50\ \mu\text{m}$) and the long ($400\ \mu\text{m}$) edges of the pixels, respectively, and are centered in x at the center of a single pixel and in y between two adjacent pixels belonging to a column pair. The data shown in Fig. 4.1 are for a $280\ \mu\text{m}$ thick sensor from the first prototype using *p-spray* isolation (ST2 sensor). The plot on the middle of the figure show the profile of

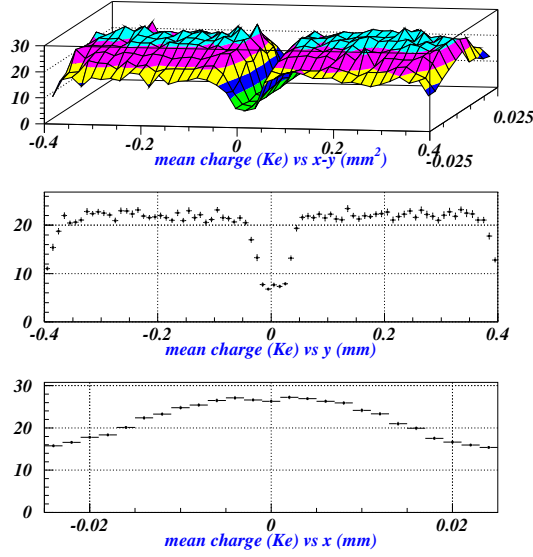


Figure 4.1: Average charge collected as a function of the position inside a pair of pixel cells for a 280 μm thick ST2 sensor.

the averaged cluster charge along the y axis (long pixel edge) calculated using only particles crossing the pixel cells within $\pm 20 \mu\text{m}$ from the centre of the pixel along the short edge. Similarly the bottom plot shows the profile of the average cluster charge along the x axis (short pixel edge) calculated using only particles crossing the pixel cells within $\pm 150 \mu\text{m}$ from the center of the pixel along the long edge.

The average charge collected at the center of the pixel was 28000 electrons, with an error of a few thousand electrons due to the uncertainty in the absolute scale provided by the calibrations. This indicates a good charge collection efficiency at the centre of the pixel: the average number of electron/hole pairs generated by a minimum ionizing particle in 280 μm of silicon is 25000.

Regions with reduced charge collection were observed at the edges of the pixels in both x and y . A possible explanation [49, 50] of this is that the n^+ implant ring that surrounds the main pixel implant (and which was introduced to minimize inter-pixel capacitance) did not float as it should, due to the presence of a current path not evident in the two-dimensional simulations used to optimize the design. It consequently collected signal charge of which part was then lost due to capacitive coupling to parasitic nodes, as the bias grid. At the end of each pixel that is directly adjacent to the bias grid, two charge loss effects combined: the capacitive effect described above and a direct loss to the implanted bias grid. In this region a relatively large amount of charge loss is visible, extending approximately $\pm 50 \mu\text{m}$ into the pixel region in the y direction; this loss profile correspond roughly to the geometry of the bias structure.

Fig. 4.2 reports a similar plot with the charge collection measurement for a 280 μm thick sensor of the first prototype production using p -stop isolation

(ST1 design). In this kind of sensor there is no floating n^+ implant ring and no bias grid. As can be seen from the figure the charge collected is rather uniform; only a small loss is visible at the edge of the pixels where the p -stop implants are located.

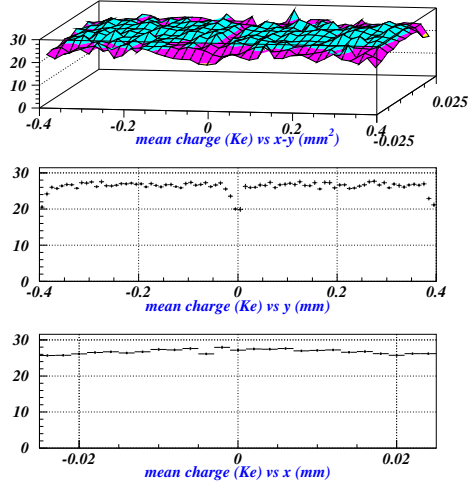


Figure 4.2: Average charge collected as a function of the position inside a pair of pixel cells for a 280 μm thick ST1 sensor.

Although the p -stop design behaves better at this stage, however it did not survive to the radiation damage after an exposure to a fluence of $10^{15} \text{ n}_{\text{eq}}\text{cm}^{-2}$; in fact it was not possible to operate p -stop sensors after irradiation due to very high leakage currents already at very low bias voltages [40, 41].

Charge Collection vs. Position

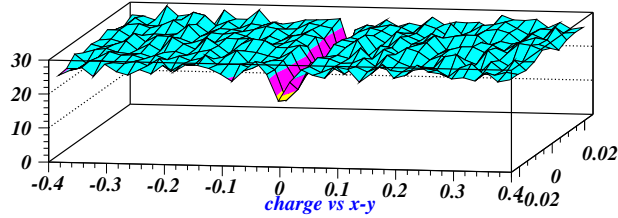


Figure 4.3: Average charge collected as a function of the position inside a pair of pixel cells for a 280 μm thick SSG sensor.

Fig. 4.3 shows the charge collection as a function of position for a 280 μm thick sensor using p -spray isolation and the SSG layout. This design is similar to the ST2 layout, with the same isolation technique, but without the n^+ floating

ring implants. It can be seen that the charge loss along the border of the pixel cells in the short (x) direction is no longer present. The charge collection is good also at the borders between columns without the bias grid ($y = \pm 400 \mu\text{m}$). There is still a charge loss effect in the region of the bias grid ($y = 0$), but it is smaller than in the ST2 sensors.

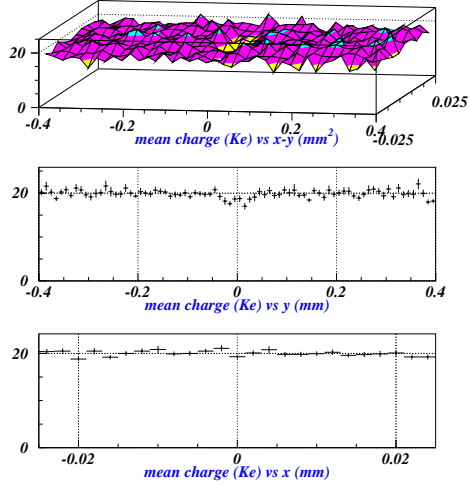


Figure 4.4: Average charge collected as a function of the position inside a pair of pixel cells for a $200 \mu\text{m}$ thick SSGb sensor.

The SSG design was adopted as a baseline and was further modified [40] in the region of the bias grid to reduce also charge loss related to the bias grid. Fig. 4.4 shows the charge collection map for a $200 \mu\text{m}$ thick SSGb sensor. Regions with poor charge collection are not seen anymore. In particular no charge loss is present at the boundaries of the pixel cell and only a very small effect is still present in the region of the bias grid. The mean value of charge collected is smaller than in the previous plots because of the reduced thickness of the sensor.

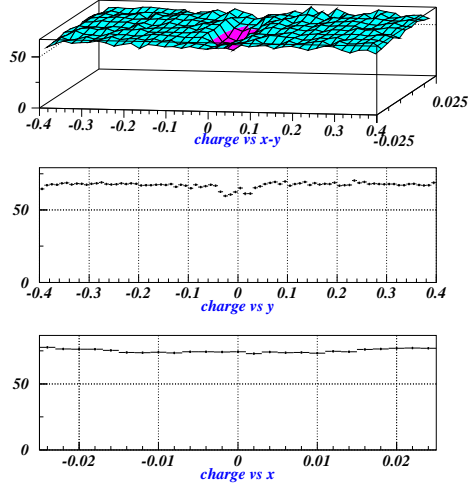
Fig. 4.5 shows the charge collection for a sensor implementing the final design (SMD) selected for ATLAS, which is basically the same as the SSGb design. It was a $250 \mu\text{m}$ thick sensor with oxygenated substrate. While all other sensors had the size of a single Front-End electronics chip this had the size of an ATLAS module and was bump-bonded to 16 Front-End B electronics chips. No calibration of the Time Over Threshold was applied; the average cluster raw ToT is plotted as a function of position. As expected the charge collection uniformity was excellent as for the SSGb sensors, with only a very small deficit in the region of the bias grid.

4.1.2 Irradiated sensors

Fig. 4.6 shows the mean cluster charge for an ST2 sensor irradiated to the fluence of $10^{15} \text{ n}_{\text{eq}}\text{cm}^{-2}$ and operated at 600 V reverse bias. As will be shown in

ATLAS Pixel Testbeam - August 2001

CiS-Preproduction+FEB+IZM
Charge collection inside Pixels



Atlas Pixel testbeam - August 2001

Milano

Figure 4.5: Average charge collected as a function of the position inside a pair of pixel cells for a 250 μm thick oxygenated SMD sensor.

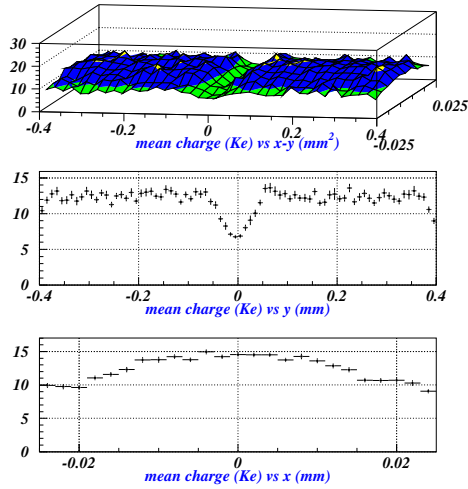


Figure 4.6: Average charge collected as a function of the position inside a pair of pixel cells for an irradiated ST2 sensor.

CIS ST2

Thresholds: 2 Ke 2.8 Ke 2.2 Ke

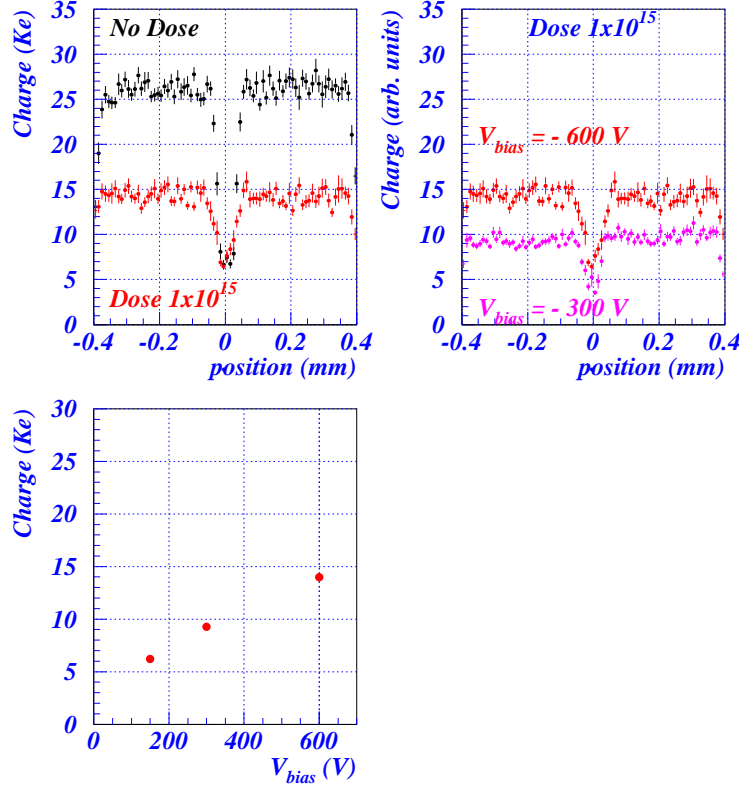


Figure 4.7: Upper plots: average charge collected as a function of position along the long pixel side y . The upper left plot compares the charge collected by an unirradiated ST2 sensor and by an ST2 sensor irradiated to $10^{15}\text{ n}_{eq}\text{cm}^{-2}$ and operated at 600 V. The upper right plot compares the charge collected by the irradiated sensor at two different bias voltages. The bottom plots reports the average charge collected at the center of the pixel as a function of bias voltage for the irradiated sensor.

section 5.2 in this conditions the depleted depth of the sensor is reduced to about $190\text{ }\mu\text{m}$. The charge losses at the edge of the pixels cells were similar to the unirradiated ST2 sensor. Comparing the bottom plots of Fig. 4.1 and Fig. 4.6 we measure an averaged collected charge at the centre of the pixel (far from the regions where charge losses are large) of 28000 electrons before irradiation and 15000 after irradiation. Most of this difference is due to the different thickness of the depleted zone. Dividing the charge collected at the centre of the pixel with the thickness of the depleted region shows that the unirradiated sensor collected $100\text{ e}^{-}/\mu\text{m}$ while the sensor irradiated to $10^{15}\text{ n}_{eq}\text{cm}^{-2}$ collected $80\text{ e}^{-}/\mu\text{m}$.

Given the uncertainties on the charge calibrations (of the order of 10%) and on the depletion depth the difference is hardly significant, but it is apparent that any charge loss due to radiation-induced trapping is not so dramatic to prevent the operation of irradiated detectors.

The upper left plot of Fig. 4.7 compares directly the charge collected by the unirradiated and irradiated sensors. The upper right plot shows that if the bias voltage of the irradiated sensor was reduced from 600 V to 300 V there was a further decrease of the charge collected. This resulted in a strong loss of efficiency (section 4.2) and it is the consequence of the reduction of the depletion depth (section 5.2) to about 110 μm . Finally, the lower plot reports the average charge collected at the center of the pixel as a function of bias voltage.

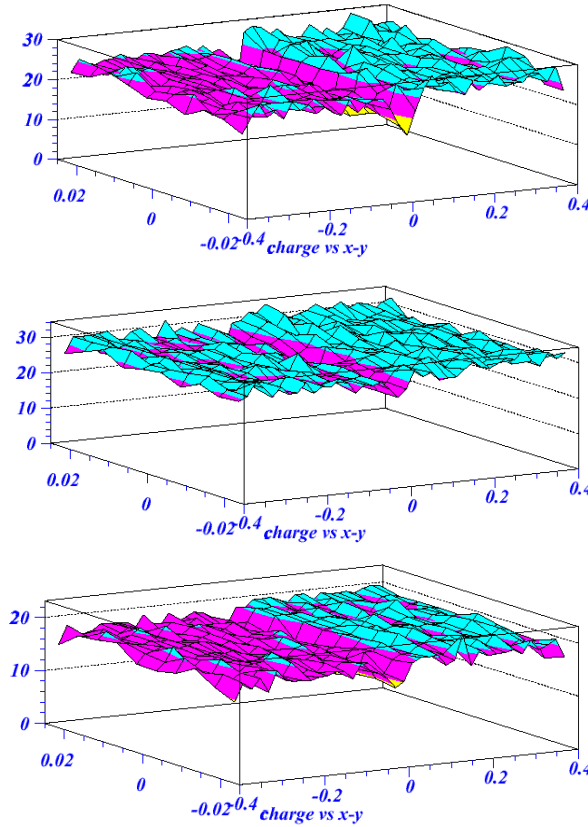


Figure 4.8: Average charge collected as a function of the position inside a pair of pixel cells for 250 μm thick oxygenated irradiated sensors. The upper plot is for an NOD sensor irradiated to $0.32 \times 10^{15} \text{ n}_{\text{eq}}\text{cm}^{-2}$, the middle plot for an SMD sensor irradiated to $0.32 \times 10^{15} \text{ n}_{\text{eq}}\text{cm}^{-2}$ and the lower plot for a SMD sensor irradiated to $0.56 \times 10^{15} \text{ n}_{\text{eq}}\text{cm}^{-2}$.

SMD and NOD sensors, both oxygenated and not oxygenated, were irradiated to $0.32 \times 10^{15} \text{ n}_{\text{eq}}\text{cm}^{-2}$ (SMD and NOD) and $0.56 \times 10^{15} \text{ n}_{\text{eq}}\text{cm}^{-2}$ (SMD only) and tested in 2000. The calibrations showed a Time Over Threshold value which saturates for relatively low charge inputs, so these data were not suited

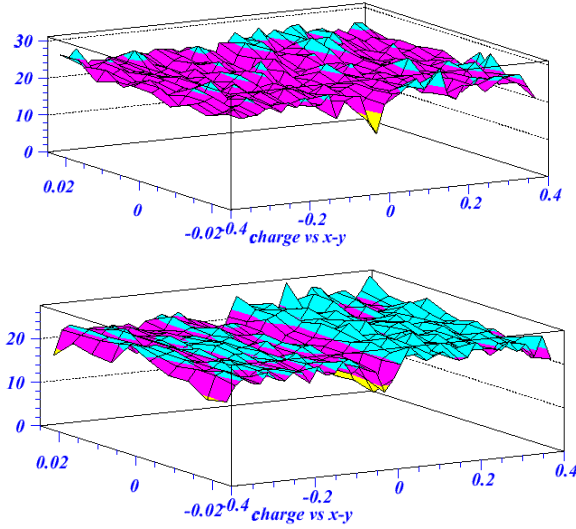


Figure 4.9: Average charge collected as a function of the position inside a pair of pixel cells for 250 μm thick not oxygenated irradiated sensors. The upper plot is for an SMD sensor irradiated to $0.32 \times 10^{15} \text{ n}_{\text{eq}}\text{cm}^{-2}$, the lower plot for an SMD sensor irradiated to $0.56 \times 10^{15} \text{ n}_{\text{eq}}\text{cm}^{-2}$.

for a precise measurement of the charge trapping; however they provided a test of the uniformity of charge collection in irradiated sensors using the new layouts. Fig. 4.8 and Fig. 4.9 shows the average Time Over Threshold as a function of position for these sensors. The SMD design showed the usual good charge collection uniformity with very small losses near the bias grid, as before irradiation. The NOD sensors (Fig. 3.6) differed from the SMD ones in not having the integrated dots in the pixel end near the bias grid. They did not show a charge collection more uniform in the bias grid region, however, so the SMD design was kept as the production layout for ATLAS pixel sensors. The use of an oxygen enriched substrate did not appear to affect the charge collection properties.

The following conclusions can be drawn from the charge collection analysis:

1. The *p-spray* isolation technique is suitable to build sensors that meet the radiation hardness requirements for ATLAS. In particular it has been shown that about 15000 electrons were collected by a detector with a depleted depth of 190 μm .
2. The original design with the floating ring was modified by removing the n^+ implant; the resulting design exhibits excellent performances of charge collection uniformity both before and after irradiation. This last issue will affect also the efficiency of the sensor, subject of the next section.

4.2 Efficiency

An efficiency of 97% is the goal for the ATLAS Pixel detector specified in the Technical Design Report [21]. With a 40 MHz bunch crossing rate expected at

LHC, the charge collected by pixels must be detected in a time window of 25 ns. Efficiency losses can be due to dead pixels because of bump-bonding failures, to a pulse height below threshold, or to the *time walk*. The latter is the time needed by the signal to reach the discriminator threshold, which is longer for smaller input charges. If the charge collected by a pixel is just above threshold it is possible that the time walk is large enough to cause the hit to be assigned to a bunch crossing different from the correct one.

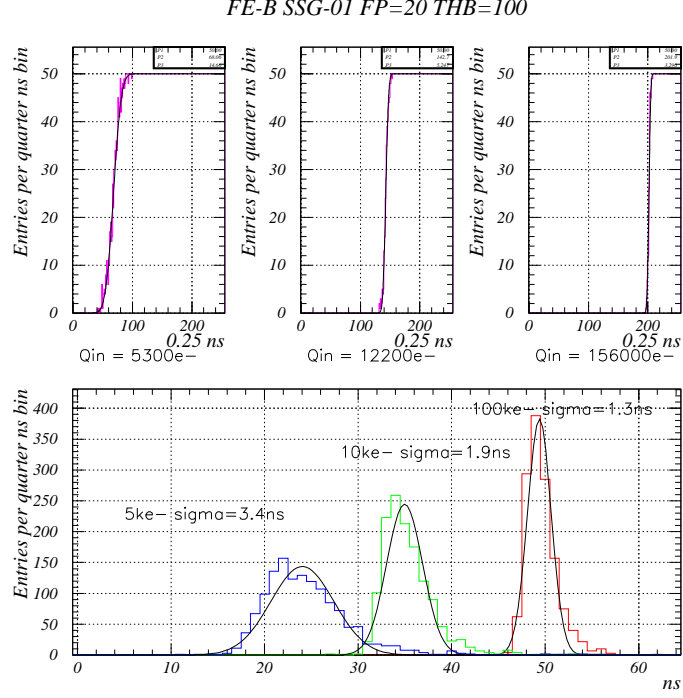


Figure 4.10: Timewalk performance of a FEB chip bump bonded to an SSG sensor . The upper plots show for three different values of injected charge the integral time distribution of hits. The lower plot show the time distribution of hits for three values of injected charge.

Fig. 4.10 shows the timewalk performance of a FE-B chip bump-bonded to an SSG sensor. The lower plot show the time distribution of hits for input charges of 5 000 electrons (blue histogram), 10 000 electrons (yellow histogram) and 100 000 electrons¹ (red histogram). If the trigger time window of 25 ns width is chosen between 30 ns and 55 ns in order to accept the hits with 100 000 electrons, nearly all the hits resulting from the injection of 5 000 electrons are lost.

¹This is a quite high value compared to the average charge released by minimum ionizing particles with normal incidence. Large energy losses are however possible, because of the high energy tail of the Landau distribution, and the time distribution of the hits is not very sensitive to the charge for high charge values.

To measure the efficiency, data were taken with the beam perpendicular to the sensor plane. The intersection of the trajectory of a beam particle with the plane of the pixel detector was calculated and required to occur in a fiducial region inside the pixel chip (at least $40\text{ }\mu\text{m}$ from the edges of the detector). Events were then divided in four classes:

- no hit was found (*missing hits*);
- a hit was found near the extrapolated point (within $150\text{ }\mu\text{m}$ in the x direction) in the expected bunch crossing (*good hits*);
- a hit was found near the extrapolated point but not in the expected bunch crossing (*timing losses*);
- a hit was found far from the extrapolated point (*tracking losses*);

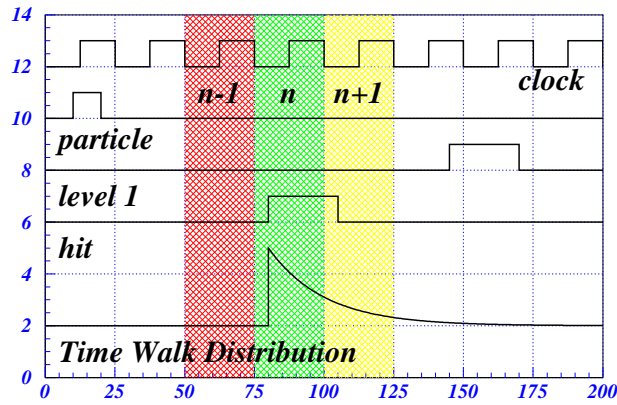


Figure 4.11: Definition of the bunch crossings for the measure of efficiency.

In ATLAS the clock will be synchronized with the bunch crossings in order to achieve the best in-time efficiency. In the H8 beam the particles were distributed uniformly in time and the pixel assemblies were operated with asynchronous clock (with respect to the particles). Hence the fraction of good hits was studied [50] as a function of the time between the arrival time of the particle and the leading edge of the clock. By considering three consecutive bunch crossings (Fig. 4.11) the time difference spanned 75 ns and by convention it was plotted between 0 and 75 ns.

The efficiency as a function of time for an unirradiated ST2 sensor is plotted in Fig. 4.12. The efficiency for each time bin was calculated as the ratio of the number of measured clusters within the position cut from the expected hit position (predicted using the silicon strip telescope) and the number of expected hits. A region of flat efficiency (98.8%) was observed, extending for about 9 ns. This maximum efficiency is the efficiency which can be obtained with a proper synchronization between the arrival time of the particles and the clock and it meets ATLAS specifications. The width of the time window in which the maximum efficiency is achieved sets the requirements on the synchronization precision.

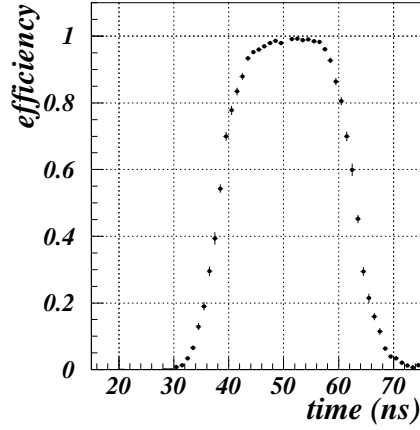


Figure 4.12: Efficiency vs time for an unirradiated ST2 sensor

| Design | ST1 | ST2 | SSG | SSGb | ST2 | ST2 | ST2* | ST2 |
|--|------|------|------|------|--------------------|-----------|-----------|-----------|
| Fluence ($\text{n}_{\text{eq}}\text{cm}^{-2}$) | 0 | 0 | 0 | 0 | 5×10^{14} | 10^{15} | 10^{15} | 10^{15} |
| Bias (V) | 150 | 150 | 150 | 150 | 600 | 600 | 600 | 300 |
| Thickness (μm) | 280 | 280 | 280 | 200 | 280 | 280 | 280 | 280 |
| Depletion (μm) | 280 | 280 | 280 | 200 | 261 | 189 | 189 | 111 |
| Threshold (ke^-) | 3.1 | 3.1 | 3.4 | 3.0 | 2.5 | 3.1 | 3.1 | 2.3 |
| Efficiency (%) | 99.6 | 98.8 | 99.3 | 99.1 | 97.5 | 95.3 | 98.4 | 87.9 |
| Losses (%) | | | | | | | | |
| hit losses | 0.1 | 0.4 | 0.2 | 0.4 | 1.3 | 2.2 | 0.4 | 6.1 |
| tracking | 0.2 | 0.2 | 0.2 | 0.1 | 0.4 | 0.1 | 0.0 | 0.1 |
| timing losses | 0.1 | 0.6 | 0.3 | 0.4 | 0.8 | 2.4 | 1.2 | 5.9 |

* With position cut, see text.

Table 4.1: Efficiencies measurement summary table.

The efficiency losses were mostly due to missing hits and timing losses (table 4.1). The positions of the track extrapolation for missing hits were located at the border of the pixel. The timing losses also occurred when the particle crossed the sensor near the pixel border and were correlated with low pulse heights.

It can be concluded that the inefficiency was caused by the combination of charge sharing between pixel and poor charge collection of the ST2 design near the pixel edges when the particles crossed the sensor in the region between two pixel implants. The low pulse height either resulted in a signal which did not reach the threshold (hit losses) or in a large time walk so that the hit was associated to the wrong bunch crossing (timing losses).

The efficiency was higher for the pixel assemblies with sensors which showed little or no charge losses near the pixel borders or the bias grid. The unirradiated ST1, SSG and SSGb sensors had peak efficiencies in excess of 99%, extending for 11, 15 and 16 ns respectively. Fig. 4.13 shows the efficiency as a function of

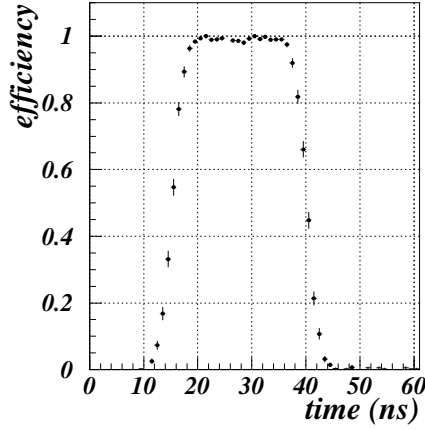


Figure 4.13: Efficiency vs time for an unirradiated SSGb sensor

time for the SSGb sensor.

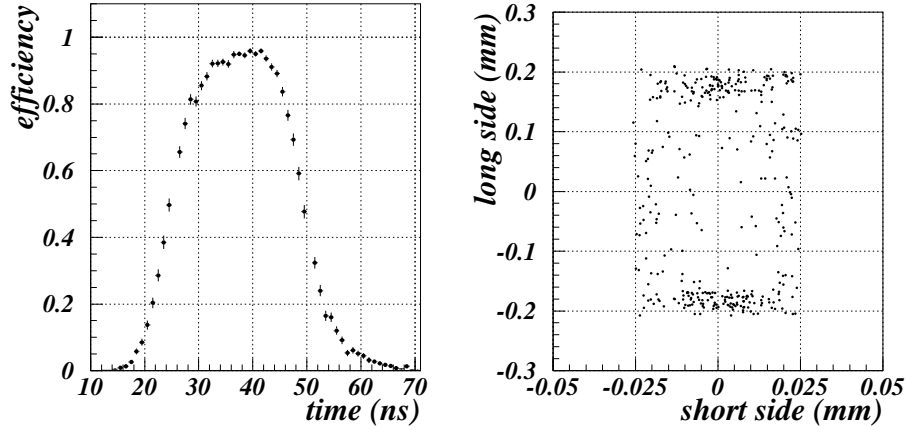


Figure 4.14: Left: efficiency vs time for an ST2 sensor irradiated to $10^{15} \text{ n}_{\text{eq}}\text{cm}^{-2}$. Right: position of the missing hits within the pixel cell, for the same sensor.

The ST2 sensors collected less charge after irradiation to $10^{15} \text{ n}_{\text{eq}}\text{cm}^{-2}$ because of partial depletion. As a consequence, the efficiency losses near the pixel borders increased. A peak efficiency of 95.3% was obtained when the sensor was operated at 600 V. The region of almost constant efficiency was reduced to approximately 5 ns (Fig. 4.14). The track positions for the missing hits were clearly correlated with the regions of reduced charge collection efficiency at the edge of the pixel (Fig. 4.14).

When the bias voltage was reduced to 300 V (this, according to the results of Chapter 5, corresponds to a depletion depth value of $111 \mu\text{m}$) the efficiency

dropped to 87.9%. This demonstrates the need for operating irradiated sensors at an high enough voltage in order to achieve a depletion depth of the order of 200 μm .

An ST2 sensor irradiated to $5 \times 10^{14} \text{ n}_{\text{eq}}\text{cm}^{-2}$ and operated at 600 V had also been tested. Under these operating conditions the device was nearly fully depleted and it showed an efficiency intermediate between that of the unirradiated sensor and that of the sensor irradiated to the higher fluence.

An estimate of the efficiency for the irradiated *p-spray* design without the charge loss problem was obtained requiring that the beam particles crossed the pixel in a region within $\pm 10 \mu\text{m}$ and $\pm 150 \mu\text{m}$ from the center of the pixel cell along the short and the long dimension, respectively. A flat top of approximately 9 ns and an efficiency of 98.4% were obtained. The results are summarized in the column of table 4.1 marked with the star.

Test beam operation of irradiated devices with the new p-spray designs (SMD and NOD) occurred in 2000 and 2001. The inefficiency of these assemblies was however quite high (from 6% up to 30%) because of the electronics readout problems described in section 3.3. The final electronics is not expected to be affected by these problems, and since the charge collection of the final sensor design is very good (section 4.1) and full depletion is obtained even after high radiation fluences (section 5.2) we are confident that even after irradiation the detectors will have a very good efficiency.

Chapter 5

Measurement of depletion depth

The choice of n^+/n silicon allowed the ATLAS Pixel sensors to operate in partial depletion mode after the radiation-induced type inversion. The depletion depth of a pixel silicon sensor as a function of fluence and bias voltage is an important parameter, as it determines the amount of charge collected, with consequences on the efficiency and spatial resolution of the devices. The need for an high efficiency leads to the requirement of a depletion depth well above $100\text{ }\mu\text{m}$ (chapter 4). Given that the maximum allowed operating voltage is 600 V [21] this leads to a limit to the fluence the sensors can be exposed to. In order to achieve the best efficiency and spatial resolution, full depletion is preferred.

A measurement of depletion depth allows a deeper understanding of the performance of the detectors after irradiation and it determines the bias voltage needed to achieve full depletion as a function of fluence. It also turned out that depletion depth and bias voltage are the most important parameters in the model that explains the measurements of Lorentz angle (chapter 6). A proper simulation of the ATLAS detector response needs the knowledge of the Lorentz angle value, which in turn will depend on depletion depth and bias voltage.

This chapter describes the method which has been developed to measure the depletion depth and the results of the measurements with test beam data.

5.1 Measurement procedure

A particle crossing the detector produces a cluster of hits consisting of the pixel cells that collect a significant fraction of the charge released in the subtended segment of the track (Fig. 5.1). For any given angle of incidence different from zero, the cluster width depends on the thickness of the depleted zone; a larger depletion depth results in larger clusters. This offers the possibility of measuring the depletion depth using the cluster size or some observable related to it.

To perform measurements of the depletion-zone depth, data were taken¹

¹Usually no magnetic field was present; however for an ST2 sensor irradiated to $0.5 \times 10^{15}\text{ n}_{\text{eq}}\text{cm}^{-2}$ and operated at 150 V only data with magnetic field were available. This did not affect the measurement, except that the effective angle to be used in the procedure described below was the incident angle plus the Lorentz angle (see Chapter 6 for a discussion

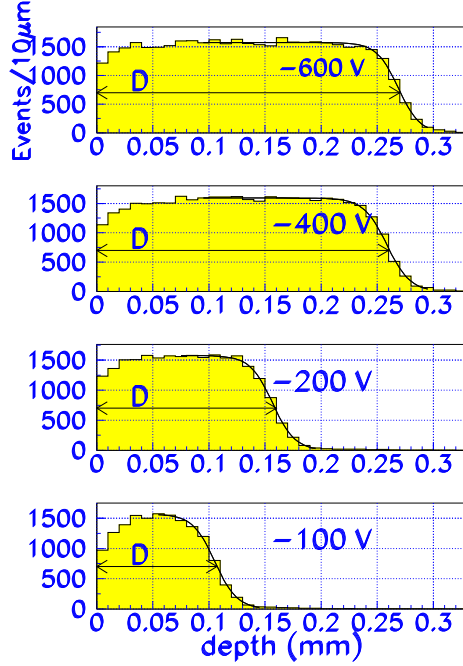


Figure 5.2: Distribution of the track-segment depth for sensors irradiated to a fluence of $0.5 \times 10^{15} \text{ n}_{\text{eq}}\text{cm}^{-2}$ for four different bias voltages. The correction for misalignments (see text) has already been included.

on the position of x_0 results in a systematic error $\Delta x / \tan \alpha$ on D.

The entrance position of the track x_0 is related to the centre of the charge release in the depleted region by

$$x_0 = x_c - d/2 \tan \alpha \quad (5.1)$$

where d is the depleted depth. x_c is determined by the alignment procedure described in section 3.2 by requiring that the mean residual between x_c and the centre of the cluster is zero. We will allow for the existence of a possible systematic error δx in the alignment and denote with x'_c the reconstructed position of the charge release in the silicon ($x'_c - x_c = \delta x$). Eq. 5.1 cannot be used because d is not known *a priori*. Hence the reconstruction program compute the entrance point as

$$x'_0 = x'_c - t/2 \tan \alpha \quad (5.2)$$

where t is the nominal thickness. This introduces the systematic error

$$\Delta x = x'_0 - x_0 = \delta x + \frac{d-t}{2} \tan \alpha \quad (5.3)$$

on the position of the entrance point of the beam particle. For a partially depleted sensor $\Delta x \neq 0$ even if no systematic error affects the reconstruction of the position of the center of the cluster, that is, if $\delta x = 0$.

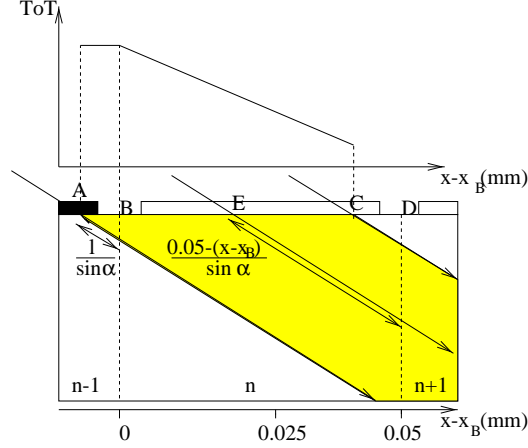


Figure 5.3: Position of the entry point of tracks that hit pixel n but not pixel $n-1$. The expected shape of the Time over Threshold of the first hit pixel as a function of the incident track position is drafted above.

This residual misalignment Δx was determined looking at the charge collected on the first pixel in the cluster. Referring to Fig. 5.3 pixel n is the first hit pixel only when the true impact position of the track is between the points A and C . If it is on the right of C , the pixel does not collect enough charge to reach the electronics threshold. If it is on the left of A , pixel $n-1$ collects enough charge to reach the threshold, so that pixel n is no longer the first hit pixel. The segment length $AB = CD = l$ is related to the electronics threshold. If the impact position is just on the left of C , the charge collected by pixel n is quite low, in fact barely above threshold. Moving the impact point to the left the charge collected by the pixel increases, as sketched in the upper part of Fig. 5.3, because of the larger pathlength of the particle under the pixel. It reaches a saturation value as $x_0 = x_B$: moving the impact position further to the left, toward point A , it does not vary because the pathlength under the pixel is the same². The position of the knee is the true position of the edge of the pixel and allows to calculate the systematic alignment correction Δx .

In Fig. 5.4 the ToT of the first pixel as a function of the distance of the reconstructed impact point x'_0 from the pixel center is plotted for an unirradiated (left) and irradiated (right) sensor. The histogram for the unirradiated sensor is fitted with the function sketched in the upper part of Fig. 5.3, that is,

$$y(x) = a + b(x - x_B)\theta(x - x_B) \quad (5.4)$$

where θ is the step function and a, b, x_B are the free parameters. This fit yields the position of the knee, x_B . As positions are measured relative to the centre of the pixel, $x_B = -25 \mu\text{m} + \Delta x$. For the unirradiated sensor of Fig. 5.4 $\Delta x = 1.2 \pm 1.8 \mu\text{m}$. This is compatible with zero, which is what expected from Eq. 5.3 for a fully depleted sensor ($d \simeq t$) if there is no systematic error in the alignment ($\delta x = 0$).

²This assumes that the *exit* position of the track from the depleted zone is always under pixel $n+1$ or further on the right. This is always true for incidence angles of 20° or 30° .

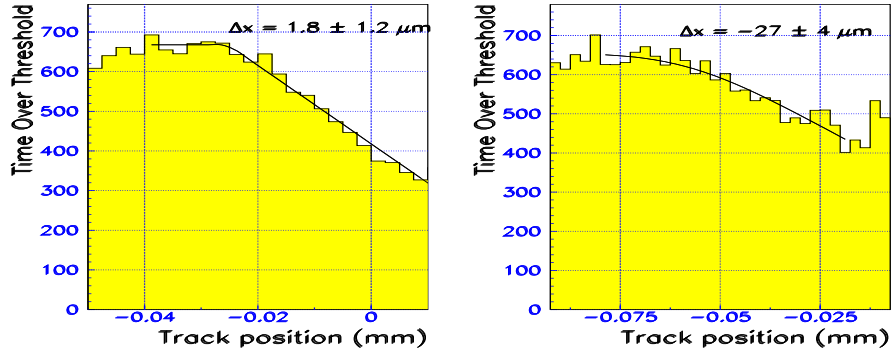


Figure 5.4: ToT of the first hit pixel as a function of track position relative to pixel center for an unirradiated (left) and an irradiated (right) sensor. The fitting functions are superimposed and the position of the knee is indicated.

The distribution of the Time Over Threshold versus position for the sensor irradiated to $10^{15} \text{ n}_{\text{eq}}\text{cm}^{-2}$ shows a larger smearing (Fig. 5.4) than the same distribution for the unirradiated sensor. The smearing has two sources: the finite telescope spatial resolution and the ToT resolution. The telescope resolution is about the same for the two sensors, but the smearing produced by the ToT resolution is much larger for the irradiated sensor. This can be understood as follows. For the unirradiated detectors, an adjustable feedback current is used to tune the discharge time of the sensor capacitance and optimize ToT resolution (section 2.6). But for sensors irradiated to $10^{15} \text{ n}_{\text{eq}}\text{cm}^{-2}$, the leakage current dominates over the adjustable feedback current, resulting in a short signal and a worse ToT resolution. Also, the charge collected is smaller (because of partial depletion) and the electronic threshold is higher. This results in a less drastic decrease of ToT level than for unirradiated sensors.

For the irradiated sensor a gaussian smearing was added to the function of eq. 5.4 to improve the convergence of the fit to the distribution of ToT versus position. The alignment correction is found to be $\Delta x = -26.5 \pm 4 \mu\text{m}$. It is different from zero, as expected for partially depleted sensors. In fact, using the measured depletion of $189 \pm 12 \mu\text{m}$ (table 5.1) Eq. 5.3 is satisfied within errors with $\delta x = 0$. For the sensor irradiated to $5 \times 10^{14} \text{ n}_{\text{eq}}\text{cm}^{-2}$ the ToT distributions behaviour is half way between that of unirradiated sensors and of sensors irradiated to $10^{15} \text{ n}_{\text{eq}}\text{cm}^{-2}$. For these sensors the fit can still be made without the gaussian smearing and the error on Δx is between 2 and 3 μm .

Once Δx has been determined, the position of the entrance point x_0 can be determined correctly ($x_0 \rightarrow x_0 - \Delta x$) and D can be calculated without this systematics ($D = D' - \Delta x / \tan \alpha$ if D' is the value found before the correction).

Correction for threshold effects. The second correction deals with the effect of the threshold on the definition of the maximum observed depth, D. Referring again to Fig. 5.1 it can be seen that the maximum measured value of D occurs when the charge collected by the last pixel is just above threshold. In this case the correction to the depth D is

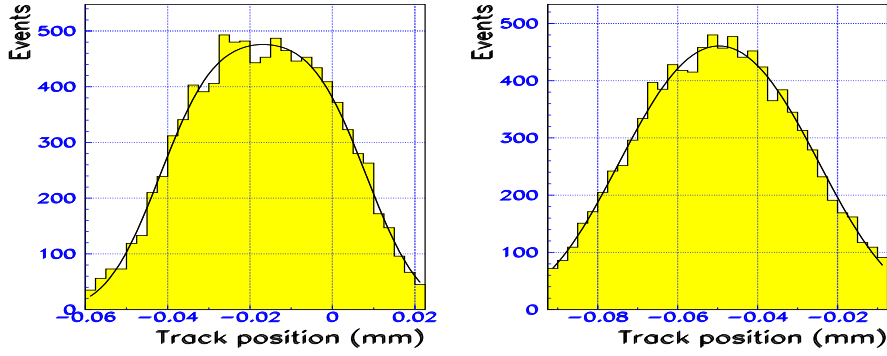


Figure 5.5: Distribution of track positions relative to the center of the first hit pixel for an unirradiated (left) and an irradiated (right) sensor. The distribution is fitted with a $50 \mu\text{m}$ square convoluted with a gaussian.

$$D - d = (p/2 - l)/\tan \alpha \quad (5.5)$$

where D is the maximum depth of track segments, d is the depletion depth, p is the pixel size and l , defined above, the projected length of the track segment corresponding to the threshold. To measure l , the distribution of the hits of pixel n as a function of the distance of the impact point of the beam particle x_0 from its center (Fig. 5.5) was used. The mean value is not zero since pixel n was hit also when x_0 was on pixel $n - 1$ (Fig. 5.3). The measured mean value is the value of l .

This correction was small. With the thresholds used in the test beam typical values of l were between $20 \mu\text{m}$ and $25 \mu\text{m}$, so that the correction $D - d$ was between 0 and $10 \mu\text{m}$.

5.2 Results

The consistency of the method was checked with fully depleted unirradiated sensors, for which the measured depletion depth should be equal to the nominal thickness. The measured depletion depth value were: $288 \pm 6 \mu\text{m}$ for an unirradiated $280 \mu\text{m}$ thick sensor and $190 \pm 7 \mu\text{m}$ for an unirradiated sensor which was nominally $200 \mu\text{m}$ thick. The errors are the statistical errors coming from the fits. The dominant error comes from the fit of the distribution of the ToT versus position with eq. 5.4 which yields the alignment correction Δx . For both sensors a depletion depth value consistent with the true thickness was found, giving confidence that the procedure outlined in the previous section was able to correctly measure the depletion depth with a systematic error smaller than $10 \mu\text{m}$.

Table 5.1 summarizes the results of the measurements made on ST2 sensors irradiated with two different fluences. These measurements are also reported in Fig. 5.6. The table also shows results for unirradiated sensors of the ST2 and SSGb types. All ST2 sensors were $280 \mu\text{m}$ thick while the SSGb sensor was

| Fluence [n/cm^2] | Thickness [μm] | Bias [V] | Depletion [μm] | $N_{\text{eff}}[10^{12}\text{cm}^{-3}]$ |
|-----------------------------|-----------------------------|----------|-----------------------------|---|
| 0 | 200 | 150 | 190 ± 7 | |
| 0 | 280 | 150 | 288 ± 6 | |
| 0.5×10^{15} | 280 | 600 | 261 ± 8 | 11.6 ± 0.7 |
| 0.5×10^{15} | 280 | 400 | 252 ± 10 | 8.3 ± 0.7 |
| 0.5×10^{15} | 280 | 200 | 147 ± 7 | 12.2 ± 1.2 |
| 0.5×10^{15} | 280 | 150 | 123 ± 11 | 13.1 ± 2.3 |
| 0.5×10^{15} | 280 | 100 | 100 ± 7 | 13.2 ± 1.8 |
| 10^{15} (1998) | 280 | 600 | 189 ± 12 | 22.1 ± 2.8 |
| 10^{15} (1999) | 280 | 600 | 217 ± 13 | 16.8 ± 2.0 |
| 10^{15} (1999) | 280 | 300 | 111 ± 10 | 32 ± 6 |

Table 5.1: Depletion depth measurements results for data taken in years 1998 and 1999.

200 μm thick. They were fabricated on standard silicon.

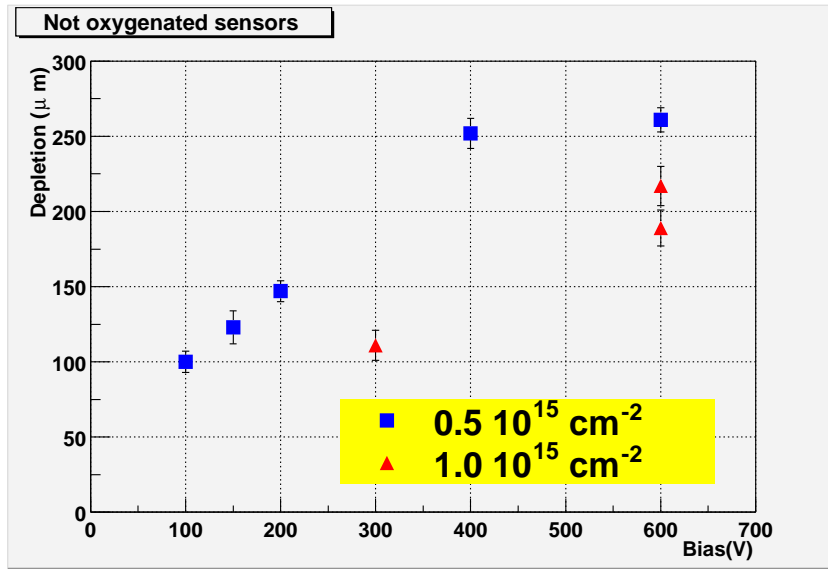


Figure 5.6: Depletion depth as a function of applied bias voltage for 280 μm thick sensors with standard silicon substrate, irradiated to two different fluences.

These results show that after a fluence of $1 \times 10^{15} \text{ n}_{\text{eq}}\text{cm}^{-2}$ an ST2 sensor had a depletion depth of about 200 μm at 600 V. The two values reported in Table 5.1 refer to the same sensor, evaluated at one year distance. The precision of the data is not sufficient to conclude that the depletion depth had actually increased. There may have been such an effect however due to annealing (section 2.2) as detectors were exposed to short periods at room temperature during handling operations. The same sensor, operated at 300 V, has a much smaller depletion depth ($111 \pm 10 \mu\text{m}$). This results in a strong loss of efficiency (section 4.2) showing that this sensor must be operated at 600 V to satisfy ATLAS requirements.

After a fluence of $0.5 \times 10^{15} \text{ n}_{\text{eq}}\text{cm}^{-2}$ the same design was almost fully depleted at 600 V. In fact, depletion depth is nearly the same at 400 V and 600 V

and the value at 600 V is only 19 μm below the nominal thickness value of 280 μm . This discrepancy is hardly significant (slightly more than two standard deviations) and it may also be due to an actual thickness slightly below the nominal value, so that it is possible that the sensor reaches full depletion just above 400 V.

The table also reports the value of effective doping concentration extracted from measured bias voltage and depletion depth. It was computed in the following way (valid when the bias voltage is below the full depletion voltage):

$$N_{\text{eff}} = \frac{2\epsilon_0\epsilon_{Si}V_{\text{bias}}}{ed^2} \quad (5.6)$$

This formula gives the average effective doping concentration in the depleted region. A uniform concentration is expected to yield a value of N_{eff} which does not depend on the bias voltage, or, equivalently, a depletion depth proportional to the square root of the bias voltage. The data show some indication of a violation of this scaling law (Fig. 5.7): the measured value of the effective doping concentration is higher at low bias voltages, when only the region near the pixels is depleted. For the sensor irradiated to the highest fluence (1999 data) the effective doping concentration at 600 V is about 2.4 standard deviations below the value found at 300 V. The bias voltage scan performed on the sensor irradiated to the lower fluence also shows an effective doping concentration which is lower at 400 V than at low bias voltages. The difference between the value at 200 V and the value at 400 V is 2.8 standard deviations. The value of N_{eff} at 600 V should be taken with care, as the sensor may be already fully depleted and Eq. 5.6 is not valid if V_{bias} is larger than the depletion voltage.

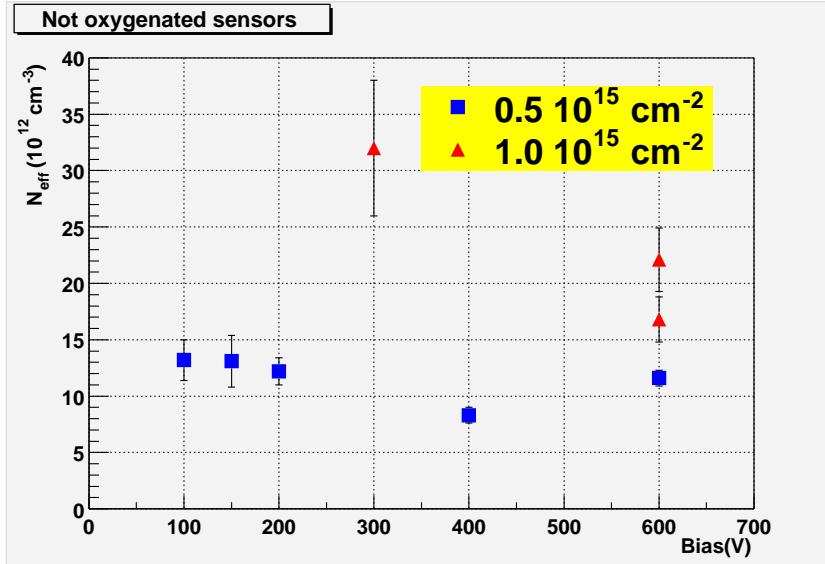


Figure 5.7: Mean effective doping concentration in the depleted zone, computed according to eq. 5.6, for 280 μm thick sensors with standard silicon substrate, irradiated to two different fluences.

It is interesting to compare the results of table 5.1 with the expectations for standard silicon sensors. For high fluences the stable radiation damage component of the effective doping concentration (eq. 2.5) can be approximated as $N_C = g_C \Phi$. Using the value $g_C = 1.9 \times 10^{-2} \text{ cm}^{-1}$ [31] N_C is predicted to be $9.5 \times 10^{12} \text{ cm}^{-3}$ for the detectors irradiated to $0.5 \times 10^{15} \text{ n}_{\text{eq}}\text{cm}^{-2}$ and $19 \times 10^{12} \text{ cm}^{-3}$ for the detectors irradiated to $10^{15} \text{ n}_{\text{eq}}\text{cm}^{-2}$. However, the actual value of N_{eff} may be higher as a significant short term radiation damage component may be present. This contribution from this component depends on the status of advancement of the annealing processes (Fig. 2.3). The exposure of the sensor to ambient temperature during handling operations or to higher temperatures during the flip-chip process (Fig. 2.17) is subject to some uncertainties, but it is not expected to be enough for the long term damage component to give a significant contribution.

Within these uncertainties the depletion values found and the corresponding effective doping concentrations are consistent with expectations.

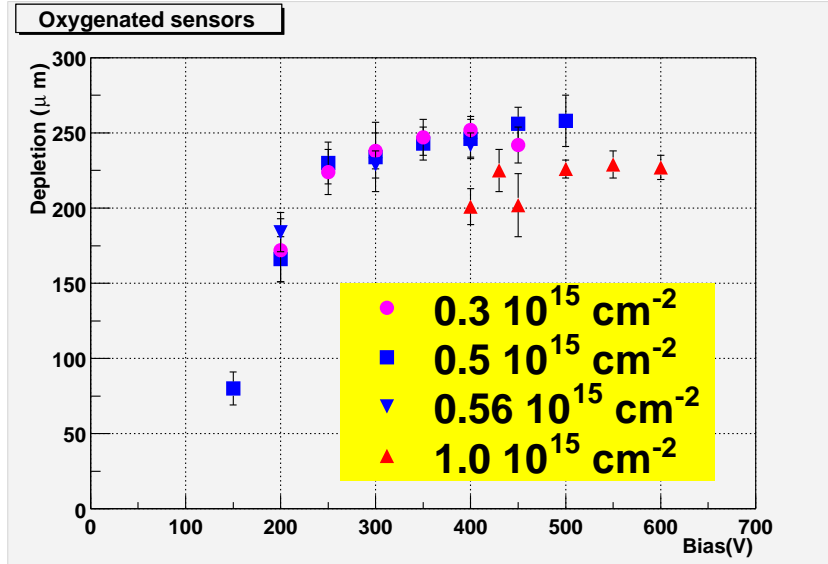


Figure 5.8: Depletion depth as a function of applied bias voltage for 250 μm thick sensors with oxygenated substrate, irradiated to various fluences. The points may be affected by systematic errors and should be considered lower limits for the depletion depth.

The data from the 2000 and 2001 test beams were affected by electronics readout problems which produced a high pixel inefficiency (section 3.3). This inefficiency reduced the cluster sizes, so that the depletion depth values measured may be affected by a systematic error which is difficult to evaluate; they should be considered lower limits on the depletion depth. Fig. 5.8 reports the results of the measurement of depletion depth made in 2000 and 2001 on 250 μm thick sensors with oxygenated substrate. The sensor irradiated to the lowest fluence used the LAD design, while all the other sensors featured the SMD design. The sensors irradiated to $0.56 \times 10^{15} \text{ n}_{\text{eq}}\text{cm}^{-2}$ and $1.0 \times 10^{15} \text{ n}_{\text{eq}}\text{cm}^{-2}$ fluence were al-

ways kept at low temperature. The sensor exposed to $0.5 \times 10^{15} \text{ n}_{\text{eq}}\text{cm}^{-2}$ fluence experienced a period of three months at 25°C and the sensor irradiated to the lowest fluence was stored at 25°C for 37 days.

The device irradiated to the highest fluence shows a depletion depth which does not depend on bias voltage. This suggests that it is already fully depleted at 400 V, even if the measured value is smaller than the sensor thickness. Not oxygenated sensors irradiated to the same fluence did not reach full depletion even at 600 V.

The oxygenated devices irradiated to the lower fluences (0.3, 0.5 and $0.56 \times 10^{15} \text{ n}_{\text{eq}}\text{cm}^{-2}$) appear to be fully depleted, or almost so, for a bias voltage as low as 250 V.

The depletion depth measurements with oxygenated sensors confirm that such devices can be operated fully depleted for the entire detector lifetime.

Chapter 6

A detailed study of Lorentz angle effects

6.1 The Lorentz angle

In the presence of an electric field E and a magnetic field B the charge carriers, generated by a passing particle within silicon, drift along a direction at an angle Θ_L (Lorentz angle) with respect to the electric field direction (due to the $\vec{E} \times \vec{B}$ effect).

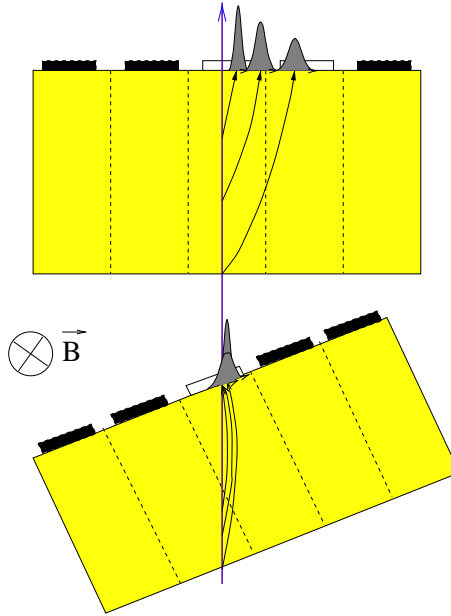


Figure 6.1: Drift of charge carriers under the influence of a magnetic field. The upper figure shows a perpendicular particle, in the lower the incident particle crosses the sensor at the Lorentz angle.

Fig. 6.1 shows schematically how this effect affects the response of a silicon pixel detector. The mean number of pixels above threshold (cluster size) is a minimum for an incidence angle equal to the Lorentz angle, instead of for normal incidence as it would be in absence of magnetic field. The angular response of the detector is modified. The occupancy and spatial resolution are changed, the change being a shift of the angular dependence by an amount equal to the Lorentz angle.

In ATLAS high- p_T particles will cross a Pixel layer at a mean angle Θ_T , where Θ_T is the tilt angle of the layer (Fig. 2.7). The response of the detector will be similar to that in absence of magnetic field for an incidence angle equal to $\Theta_T - \Theta_L$. The knowledge of Θ_L is needed for a correct simulation of the detector response during ATLAS operation. In principle it is also needed to choose the tilt angle in order to get the best performances; however the choice of Θ_T is strongly constrained by the limited space available.

This chapter describes the measurement of the Lorentz angle with test beam data and their interpretation in terms of a model for charge drift in silicon. An unexpected dependence of the Lorentz angle on the electric field inside the sensor is found. The prediction of the model for the Lorentz angle in ATLAS operating conditions is discussed in the last section. The effects of Lorentz angle variation with bias voltage on tracking and b-tagging performances are the argument of Chapter 8.

6.2 Measurement of magnetic field

Since the Lorentz angle depends on the magnetic field (section 6.4) the value of B is needed for the measurements of Lorentz angle to have a meaning. The magnetic field profile along the beam inside the magnet is reported in Fig. 3.3. As the field value had a strong dependence on the beam axis coordinate z , the position of the telescope inside the magnet is needed to determine the magnetic field value for the pixel assemblies under test.

Since the position of the telescope with respect to the magnetic field was not known with the precision needed for the measurement of the Lorentz angle, it was measured from the data. Since the momentum of the beam particles is precisely known, there is a one to one correspondence between beam particle's radius of curvature and the telescope position. This function is computed as follows: for every possible telescope position the expected radius of curvature is computed tracing the beam particle inside the known magnetic field, evaluating the intersection points with the strip planes and fitting the coordinates of the points using a parabola. The results of this calculation are shown in Fig. 6.2 for 2 different telescope setups (1998 and 1999 setups). For every run, the position of the telescope is then evaluated by measuring the radius of curvature (Fig. 6.3) and using the function of Fig. 6.2. The reconstructed position for the 3 sets of runs used for the Lorentz angle measurement are pictorially shown in Fig. 6.4 where the magnetic field profile is also shown. The procedure above allowed us to know the intensity of the magnetic field at the position of the pixel detector under test. The error on the telescope position was estimated to be about 5 cm, arising from the spread of curvature values within each run set and the uncertainty on the telescope total length (about 1%).

For runs 3700-3777 (August 1998) the magnetic field was 1.48 ± 0.02 T on

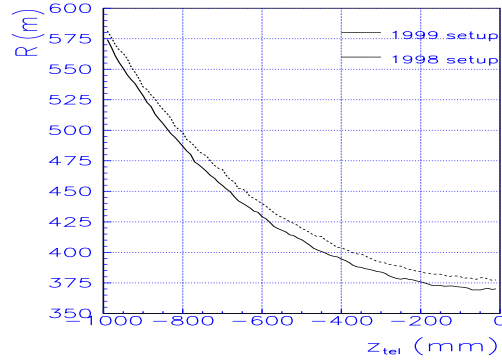


Figure 6.2: Expected radius of curvature of the tracks reconstructed by the silicon microstrip telescope as a function of the telescope center position. The curves were computed from magnetic field profile and telescope microstrip relative positions.

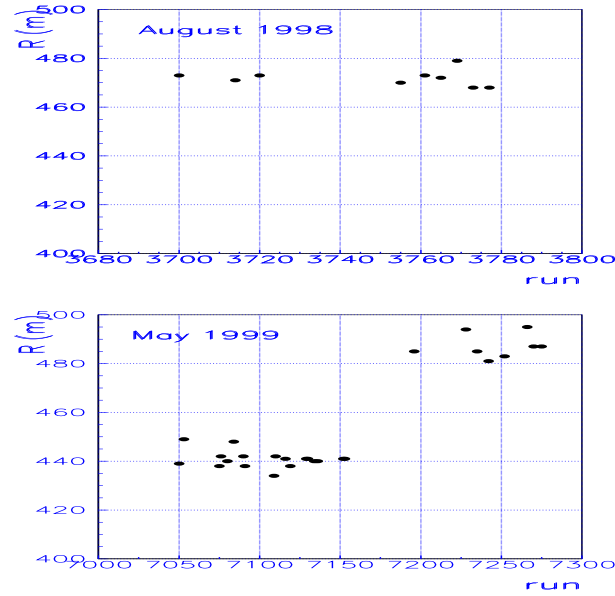


Figure 6.3: Measured radius of curvature of the tracks reconstructed by the silicon microstrip telescope as a function of run number, for the runs used in the measurements of Lorentz angle.

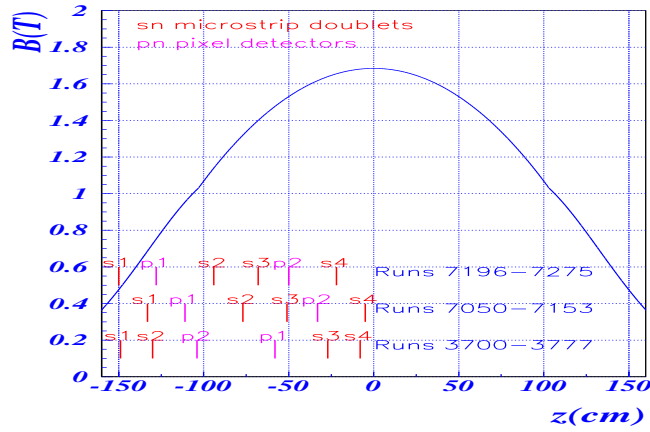


Figure 6.4: Reconstructed telescope position for the three run sets used in the Lorentz angle measurement. p1 and p2 are the pixel detectors. s1, s2, s3 and s4 are the microstrip doublets. The magnetic field profile is superimposed.

pixel detector 1 (an unirradiated sensor) and 1.01 ± 0.05 T on pixel detector 2 (a sensor irradiated to $10^{15} \text{ n}_{\text{eq}}\text{cm}^{-2}$). In 1999 only the pixel detector holder number 1 was used. The magnetic field was 0.95 ± 0.05 T for runs 7050-7153 and 0.74 ± 0.05 T for runs 7196-7275¹. The errors are derived from the uncertainty on the telescope position.

6.3 Measurement of Lorentz angle

The Lorentz angle for irradiated and unirradiated sensors was determined by measuring the mean cluster size as a function of the angle of the incident beam particles. The cluster size is minimum when the incident angle is equal to the Lorentz angle, as shown schematically in Fig. 6.1. This allowed to extract the Lorentz angle value from the data.

For each angle, two measurements were performed in sequence. Data were taken with magnetic field off and with magnetic field on. The cluster size was measured using only the minimal cuts described in section 3.2 in order to avoid biases. The dominant uncertainty on the mean cluster size was systematic. It was conservatively taken as half of the maximum difference between pairs of mean cluster sizes measured at opposite angles for data taken without the magnetic field. This amounted to 0.03. In fact, with no magnetic field any difference in mean cluster sizes at opposite angles is attributable to alignment uncertainties.

The mean cluster size as a function of the angle for an unirradiated sensor operated at 150 V is shown in Fig. 6.5 for $B = 0$ T and $B = 1.48$ T. The angular shift in the detector response is evident.

The minimum was extracted by fitting the mean cluster size with a parabola. A more complicated function of the angle was also investigated to fit the data.

¹The detectors under test were changed between these two sets of runs.

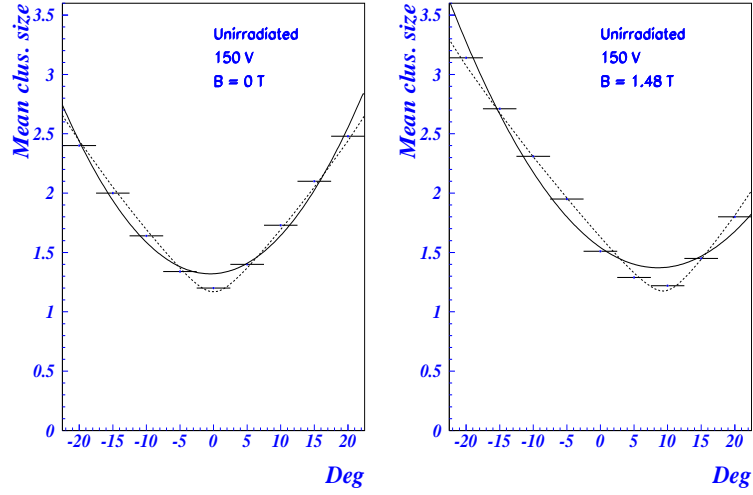


Figure 6.5: Mean cluster size as a function of the track angle of incidence for an unirradiated sensor, without magnetic field (left) and with a magnetic field of 1.48 T (right). The solid line corresponds to the parabola fit. Model prediction is superimposed (dashed line).

It was based on a simple model of charge drift in silicon with five variable parameters, including the Lorentz angle. The agreement with the data was improved but the values of Lorentz angle were nearly equal to those obtained with the parabola fit, hence the simpler parabola function was used. The fit is shown in the figures as a solid curve, while the dashed curve is the theoretical prediction obtained with the model described in section 6.4.

Data taken without magnetic field were used to check systematic errors caused by the angular positioning of the sensor. In this case the minimum was expected at 0° and any deviation from this value was used to correct the measurement; the value of the correction was finally quoted as a systematic error.

The Lorentz angle for the unirradiated sensor was measured to be $9.0 \pm 0.4 \pm 0.5^\circ$, where the former error comes from the fit (containing the statistical and systematic error on mean cluster size described above) and the latter from the subtraction of the value found for data without magnetic field.

In Fig. 6.6 data for a sensor irradiated to $0.5 \times 10^{15} \text{ n}_{\text{eq}}\text{cm}^{-2}$ are shown. The left plot reports the measurement on data taken with an operating voltage of 600 V and no magnetic field. The central plot is for data with a magnetic field of 0.95 T and the same operating voltage of 600 V. The Lorentz angle was found to be $2.6 \pm 0.2 \pm 0.3^\circ$.

An angular scan was also made with the same sensor operated at 150 V but only with the magnetic field. The results are reported in the right plot of Fig. 6.6. In fact for each value of the tilt angle three measurements were made in sequence: with a bias voltage of 600 V and no magnetic field, with a bias voltage of 600 V and a magnetic field of 0.95 T, with a bias voltage of 150 V

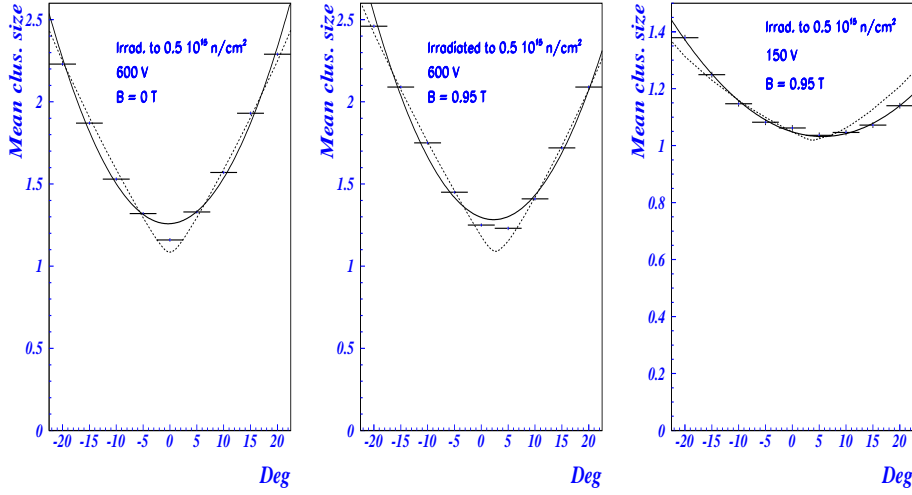


Figure 6.6: Mean cluster size as a function of the track angle of incidence for a sensor irradiated to $0.5 \times 10^{15} \text{ n}_{\text{eq}}\text{cm}^{-2}$. The left plot is for data without magnetic field and a bias voltage of 600 V, the central plot for $B=0.95 \text{ T}$ and $V_{\text{bias}} = 600 \text{ V}$, the right plot for $B=0.95 \text{ T}$ and $V_{\text{bias}} = 150 \text{ V}$. The solid line corresponds to the parabola fit. Model prediction is superimposed (dashed line).

and a magnetic field of 0.95 T. Data taken at 600 V and no magnetic field were used to correct the alignment systematics for both the data taken at 600 V and 150 V. The Lorentz angle value found at 150 V was $5.9 \pm 1.0 \pm 0.3^\circ$. It is considerably higher than the value found for the same sensor and same magnetic field when operated at 600 V.

Note also the different vertical scale of the three plots of Fig. 6.6. When the sensor was operated at 150 V the mean cluster sizes were considerably smaller than those found for an operating voltage of 600 V, because the depleted depth was much smaller (section 5.2).

In Fig. 6.7 data for a sensor irradiated to $10^{15} \text{ n}_{\text{eq}}\text{cm}^{-2}$ and operated at 600 V bias voltage are reported. The magnetic field was 1.01 T. The Lorentz angle value was found to be $3.1 \pm 0.4 \pm 0.6^\circ$. One year later the measurement was repeated on the same sensor operated at the same voltage, with a magnetic field of 0.74 T. A value of $2.7 \pm 0.4 \pm 0.4^\circ$ was found. Using the relation $\Theta_L \simeq \tan \Theta_L \propto B$ (eq. 6.4.2 of section 6.4) this value correspond to $3.6 \pm 0.5 \pm 0.5^\circ$ for $B=1.01 \text{ T}$ so it is in agreement with the measurement of the previous year.

Results of Lorentz angle measurements are summarized in table 6.1. All the sensors used standard silicon substrates and implemented the ST2 design. The measurements show an unexpected variation of the Lorentz angle, even when the differences of magnetic field were taken into account. A model of charge drift in silicon was developed to provide an explanation to the measured Lorentz angle values. It is described in the next section.

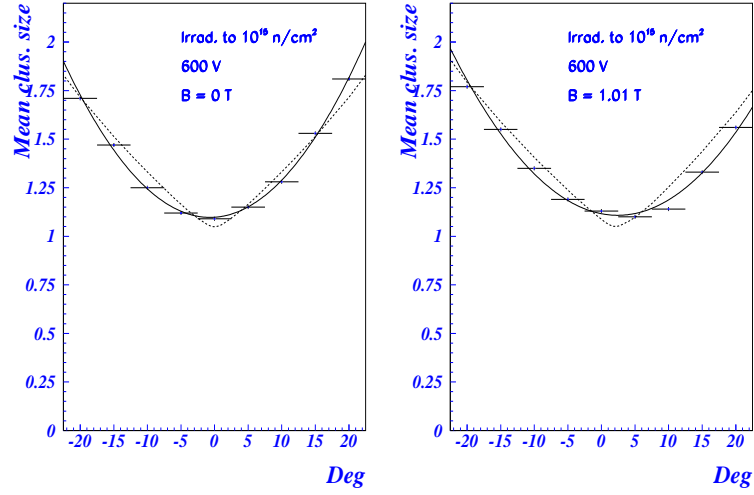


Figure 6.7: Mean cluster size as a function of the track angle of incidence for a sensor irradiated to $10^{15} \text{ n}_{\text{eq}}\text{cm}^{-2}$, without magnetic field (left) and with a magnetic field of 1.01 T (right). The solid line corresponds to the parabola fit. Model prediction is superimposed (dashed line).

| $\Phi [\text{n}_{\text{eq}}\text{cm}^{-2}]$ | 0 | 0.5×10^{15} | 0.5×10^{15} | 1×10^{15} ('98) | 1×10^{15} ('99) |
|---|-----------------------|-----------------------|-----------------------|--------------------------|--------------------------|
| Bias [V] | 150 | 150 | 600 | 600 | 600 |
| T [$^{\circ}\text{K}$] | ~ 300 | 264 | 264 | 264 | 264 |
| d [μm] | 288 ± 6 | 123 ± 11 | 261 ± 8 | 189 ± 12 | 217 ± 13 |
| B [T] | 1.48 ± 0.02 | 0.95 ± 0.05 | 0.95 ± 0.05 | 1.01 ± 0.05 | 0.74 ± 0.05 |
| Θ_L (meas.) [$^{\circ}$] | $9.0 \pm 0.4 \pm 0.5$ | $5.9 \pm 1.0 \pm 0.3$ | $2.6 \pm 0.2 \pm 0.3$ | $3.1 \pm 0.4 \pm 0.6$ | $2.7 \pm 0.4 \pm 0.4$ |
| Θ_L (th.) [$^{\circ}$] | 9.3 ± 0.4 | 3.7 ± 0.5 | 2.7 ± 0.2 | 2.1 ± 0.2 | 1.8 ± 0.2 |

Table 6.1: Lorentz angle measurement results. The theoretical predictions obtained with the model described in section 6.4 are also reported.

6.4 Interpretation of the measurements of Lorentz angle

The values of Lorentz angle we measured using test beam data were compared with the predictions of a model [1] that evaluates the charge drift in silicon and computes the mean cluster multiplicity as a function of the incidence angle using the properties of the detectors under study (temperature, magnetic field, bias voltage, depletion depth, geometry, thresholds).

6.4.1 Charge drift in silicon

The properties of charge drift in silicon² are important to understand and compute Lorentz effects. The motion of electrons and holes in presence of an electric field will be discussed first, then the effects produced by the Lorentz force will be considered.

Drift mobility

For low electric fields, holes and electrons drift with an average velocity proportional to the field strength:

$$v_d = \mu_d E \quad (6.1)$$

The constant of proportionality μ_d is called **drift mobility**. It is the most important parameter which enters the computation of the Lorentz angle, hence it will be discussed in some detail. The mobility is related to the mean free time between collisions of the charge carriers with the lattice by the relation

$$\mu_d = \frac{e\tau}{m^*} \quad (6.2)$$

This relation can be derived assuming that the charge carriers move as in vacuum (with effective mass m^*) between collisions and have zero average velocity after each collision; in this conditions the average velocity is $\frac{qE}{m^*}\tau$ which yields the above relation. The collisions are due to deviations of the crystal from a perfect geometrical lattice. These deviations can occur either because of the presence of extraneous or misplaced atoms (impurities) or because of the thermal vibrations. The crystal vibration quanta are called phonons. The charge carriers interacts with charged impurity centers and with phonons. The scattering against phonons increases with temperature, while the scattering against impurity centers increases with the doping concentration and decreases with temperature. The ATLAS silicon pixel detectors substrates have a low doping concentration in order to achieve full depletion at reasonably low bias voltages, while the operating temperature is of the order of room temperature. In this conditions the phonon scattering dominates over charged impurity scattering and it is in fact the only significant scattering mechanism. Hence the mobility decreases with temperature, but it is independent of doping concentration up to concentrations much higher than those of our sensors.

The mobility dependence on the impurity concentration and temperature is shown in Fig. 6.8. The typical doping level of our detectors is of the order of 10^{12} cm^{-3} . The irradiation increases the effective doping concentration which however remains below $4 \times 10^{13} \text{ cm}^{-3}$ (Fig. 5.7) even for the sensors irradiated to $10^{15} \text{ n}_{\text{eq}}\text{cm}^{-2}$, safely below the level at which the scattering over impurities begins to play a role and the mobility decreases.

The variation of mobility with temperature, on the contrary, is significant. At room temperature there is an 8% change in the mobility for every 10 degrees change in temperature. The room temperature mobility is about $1500 \text{ V}^{-1}\text{cm}^2\text{s}^{-1}$ for the electrons and $450 \text{ V}^{-1}\text{cm}^2\text{s}^{-1}$ for the holes, which have an higher effective mass.

²For a discussion of the properties of charge carriers in silicon Ref. [23, 51] are useful. For a review of drift velocity and diffusivity measurements see [52, 53].

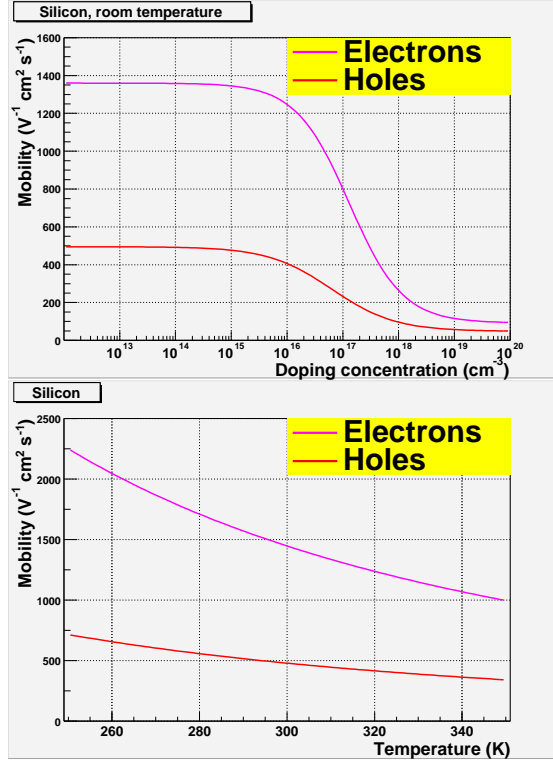


Figure 6.8: Above: low field mobility as a function of impurity concentration in silicon at room temperature. Below: low field mobility as a function of temperature in high purity silicon. The curves are computed according to the experimental data parametrisations given in [52].

When the fields are sufficiently large the linear relation between drift velocity and electric field is lost, resulting in a field-dependent mobility. Fig. 6.9 shows the room-temperature drift velocity versus the electric field for electrons and holes in high purity silicon. Saturation occurs at high fields. The saturation velocity is about 10^7 cm/s for both electrons and holes, in contrast to the low field regime where electrons had a three-fold larger mobility than holes. The transition from the linear regime to saturation occurs at higher fields for holes than for electrons.

The electric field in the pixel sensors is of the order of $1 \text{ V}/\mu\text{m}$ which is in the intermediate region between the linear regime and saturation. The mobility can thus be significantly smaller than the low-field value. The following parametrisation [52] describes the drift mobility as a function of temperature and electric field assuming a low impurity concentration:

$$\mu_d = \frac{v_s/E_c}{[1 + (E/E_c)^\beta]^{1/\beta}} \quad (6.3)$$

This parametrisation should be used for $T > 250 \text{ }^\circ\text{K}$ and it also describes the drift mobility when the electric field is along the $\langle 111 \rangle$ crystallographic

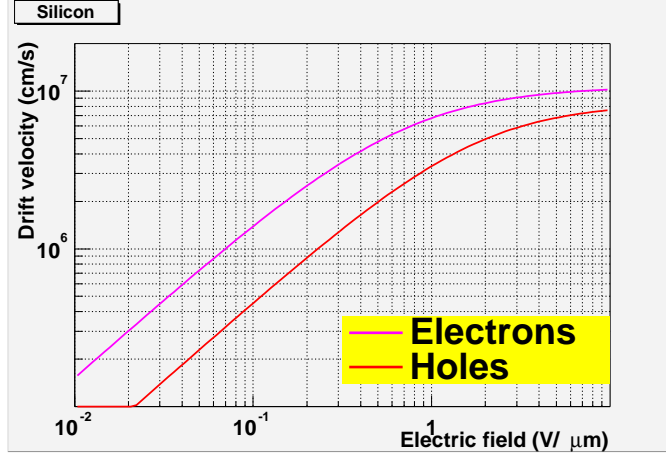


Figure 6.9: Room-temperature drift velocity for electrons and holes in high-purity silicon. Based on the experimental data parametrisations given in [52].

| | Electrons | Holes |
|--------------------------|---|---|
| $v_s (\text{cm s}^{-1})$ | $1.16 \cdot 10^7 \cdot (T/273)^{-0.87}$ | $0.88 \cdot 10^7 \cdot (T/273)^{-0.52}$ |
| $E_c (\text{V cm}^{-1})$ | $6030 \cdot (T/273)^{1.55}$ | $15350 \cdot (T/273)^{1.68}$ |
| β | $1.04 \cdot (T/273)^{0.66}$ | $1.19 \cdot (T/273)^{0.17}$ |

direction. This was the case for the sensors used in the measurements of Lorentz angle. The low-field drift mobility does not depend on the direction but at high electric fields it is slightly different when \vec{E} is along the $\langle 100 \rangle$ or the $\langle 110 \rangle$ direction [52, 53]; this is the consequence of the anisotropy of the silicon crystal energy bands.

The parameters of the formula have all a simple physical meaning. v_s is the saturation velocity. It decreases with temperature, but less strongly than the low-field mobility. E_c provides the electric field scale at which transition from the linear regime to saturation occurs. At 273 °K it is 0.6 V/μm for electrons and 1.5 V/μm for holes, and it increases with temperature. β describes the rapidity of the transition between the two regimes. An high value of β indicates a sharp transition. It is nearly one, especially for electrons. This is interesting, as for $\beta = 1$ the equation of motion is analytically integrable. The low-field mobility is $\mu_0 = v_s/E_c$.

An alternative parametrisation is provided in Ref. [25].

The irradiated sensors have higher electric fields than before irradiation, because they are operated at higher bias voltages and/or have a smaller depletion depth. They must also be cooled, and in the test beam they are operated at lower temperature than unirradiated detectors (see table 6.1). Fig. 6.10 shows the mobility as a function of electric field for the two temperatures used in the test beam, $T = 264$ °K for irradiated sensors and $T = 300$ °K for the unirradiated one. The markers show the electron mobility corresponding to the mean electric field and the temperature of the tested devices.

In ATLAS the temperature of the Pixel detector will be 273 °K. The bias

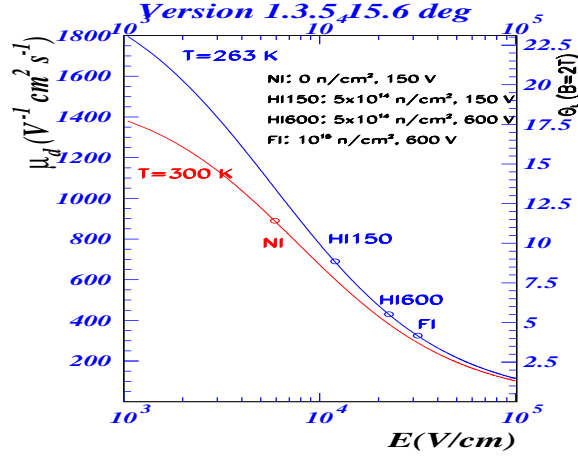


Figure 6.10: Drift mobility of holes and electrons as a function of electric field for absolute temperatures 264 °K and 300 °K . The points corresponding to the mean electric field and temperature of the detectors under test are also reported. On the right scale Lorentz angle at 2 T (foreseen running conditions in ATLAS) predicted by the model.

voltage will be raised as irradiation will proceed, resulting in a gradually smaller mobility. In the next section it will be shown that the Lorentz angle is almost proportional to the drift mobility, and on the right scale of Fig. 6.10 it is shown the Lorentz angle for a magnetic field of 2 T perpendicular to the electric field (ATLAS barrel conditions).

Diffusion

As the charge released by a particle drifts toward the electrodes, it experiences a lateral spread. This is why the mean cluster size is larger than one even when the incident angle is equal to the Lorentz angle. This effect will also enter in the spatial resolution discussion of chapter 7. The lateral spread of the charge is proportional to the square root of the time. The charge profile is a gaussian whose standard deviation is [23]

$$\sigma = \sqrt{2Dt} \quad (6.4)$$

D is called *diffusivity*. When the charge carriers are in thermal equilibrium with the crystal, which is true for low electric fields, the Einstein relation holds:

$$D = \frac{kT}{q} \mu \quad (6.5)$$

When the electric field increases above the region of constant mobility, the charge carriers are no longer in thermal equilibrium with the crystal, but this relation still describes the data provided that the field-dependent mobility and an electron effective temperature corresponding to the mean carrier energy are used instead of the low-field mobility and the thermal kinetic energy. The

dependence of diffusivity on the electric field is moderate, as the increase of the effective electron temperature compensates the decrease of mobility in eq. 6.5.

6.4.2 The Lorentz effect

In presence of magnetic field perpendicular to the electric one the charge carriers are subject to the Lorentz force $e\vec{v}_d \times \vec{B}$. This results in a mean velocity along the Lorentz force direction $v_L = \frac{ev_d B}{m^*} \tau$. The resulting Lorentz angle is

$$\tan \Theta_L = \frac{v_L}{v_d} = \frac{eB}{m^*} \tau = \mu_d B$$

If τ is not a constant, but it depends on the carrier energy, a bit more care is needed in dividing factors out and a numerical factor arises

$$\tan \Theta_L = \mu_H B = r \mu_d B \quad (6.6)$$

where

$$r = \frac{\langle \tau^2 \rangle}{\langle \tau \rangle^2} = \frac{\int \tau(\mathcal{E})^2 \rho(\mathcal{E}) d\mathcal{E}}{[\int \tau(\mathcal{E}) \rho(\mathcal{E}) d\mathcal{E}]^2} \quad (6.7)$$

This result is obtained also with a proper quantum mechanical treatment [51]. μ_H is called Hall mobility. The ratio r between Hall and drift mobility depends on the details of the scattering mechanism. It is called Hall scattering factor, it is a pure number and its value is about 1.

The charge carrier energy distribution $\rho(\mathcal{E})$ in a semiconductor is the Boltzmann distribution. If the energy dependence on momentum $\mathcal{E}(\vec{p})$ is isotropic, $\tau \sim \mathcal{E}^{3/2}$ for ionized impurity scattering and $\tau \sim \mathcal{E}^{-1/2}$ for phonon scattering [23]. The latter is dominant for ATLAS Pixel sensors. Using equation 6.7, $r = 3\pi/8 = 1.18$ is found for phonon scattering in isotropic semiconductors.

However, in silicon the carrier energy depends also on the momentum direction relative to the crystal orientation, and the computation of r is much more difficult. A review of theoretical predictions and experimental data can be found in Ref. [54] and [53]. The value of r can be measured experimentally using the Hall effect [23, 54].

For low magnetic fields ($\mu B \ll 1$) $r = 1.15$ for electrons and $r = 0.7$ for holes at room temperature. There is a weak dependence on temperature; the following parametrisation describes the dependence of r on temperature near 300 ° K

$$\begin{aligned} r &= 1.13 + 0.0008 \cdot (T - 273) \quad \text{for electrons} \\ r &= 0.72 - 0.0005 \cdot (T - 273) \quad \text{for holes} \end{aligned} \quad (6.8)$$

The Hall scattering factor dependence on impurity concentration is negligible at the doping levels of high energy physics detectors. In the high magnetic field limit, $r = 1$. The low field condition is equivalent to a Lorentz angle much less than unity; the maximum value we measured in the test beam was indeed only 157 mrad.

The Hall scattering factor is nearly constant, but the mobility has a very significant dependence on both temperature and electric field. The Lorentz angle is proportional to the mobility (neglecting the small difference between

Θ_L and $\tan \Theta_L$). In the irradiated detectors the bias voltage must be increased to achieve the same depletion depth, and the mobility strongly decreases in spite of the smaller temperature (Fig. 6.10). Hence the Lorentz angle is also smaller, as observed.

In order to obtain a quantitative prediction for the Lorentz angle, two difficulties must be addressed:

- The Lorentz angle is different for holes and electrons, as there is up to a factor of three between electron and hole mobilities. The next section discusses the formation of their signal on the pixel electrodes. It shows that even if the induced current receives contributions from the motion of both charge carriers inside silicon, only the electron motion needs to be taken in consideration to compute the signal at the preamplifier output.
- The electric field near a pn junction is not constant (Fig. 2.1). As a consequence of the electric field variation, the Lorentz angle changes from point to point inside the detector and the charge carriers drift along curved paths (Fig. 6.1). In section 6.4.4 the effective Lorentz angle, defined as the angle at which the cluster size is minimum, is computed and compared to the test beam measurements.

6.4.3 Signal induced on the pixels

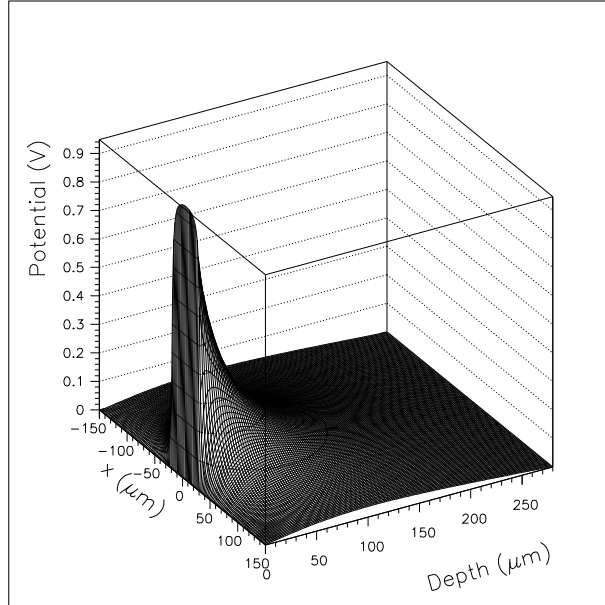


Figure 6.11: Ramo potential for a 50 μm pitch strip detector.

The contribution of a charge moving inside silicon to the signal on an electrode can be computed as follows [55]. A fictitious potential (*Ramo potential*) is computed applying $V_0 = 1$ V on the electrode under investigation and 0 V on any other electrode. This potential is shown in Fig. 6.11 for 50 μm strips (a

good approximation for ATLAS pixels). The contribution of a moving charge to the current on the pixel is

$$i(t) = q\vec{v}_d(t) \cdot \vec{\nabla}(V/V_0) \quad (6.9)$$

where V is the Ramo potential and the gradient is computed at the charge location. Both electrons and holes give a contribution to this current. The integral of the current (that is, the total charge collected) induced by an electron-hole pair generated at the point X is

$$\begin{aligned} Q(t) &= \frac{+e}{V_0} \int \vec{\nabla}(V) \cdot \vec{v}_h dt_h + \frac{-e}{V_0} \int \vec{\nabla}(V) \cdot \vec{v}_e dt_e = \\ &= \frac{+e}{V_0} \int_X^Y \vec{\nabla}(V) \cdot \vec{ds}_h + \frac{-e}{V_0} \int_X^Z \vec{\nabla}(V) \cdot \vec{ds}_e = \\ &= e(V_Y - V_X + V_X - V_Z)/V_0 \end{aligned}$$

where Y is the arrival point of the hole (which is always the backplane) and Z the arrival point of the electron. V_X cancels out, $V_Y = 0$ and V_Z is 0 if the electron is collected by another pixel and equal to V_0 if the electron is collected by the pixel under consideration. The result is that the integral of the current on the pixel is the number of electrons collected by the pixel. Pixels which collect no charge also have transients but the integral of the current is zero.

The peak amplitude at the output of the preamplifier depends on the integral of the current if the response time is much larger than the drift time of the charges. A very fast electronics is sensitive to the transients.

It is apparent from Fig. 6.11 that the contribution of a charge to the signal on the pixel is significant only for the charges moving in a quite limited region around the pixel (within $\sim 50 \mu\text{m}$). The time needed by an electron to reach this region can be estimated using a constant drift velocity as $d/v_d = d/\mu_d E = d^2/\mu_d V_{\text{bias}}$ where d is the depletion depth. The time needed by holes to exit the region near the pixels where their contribution to the signal is significant is $50 \mu\text{m}/v_d$. Both times are a few nanoseconds. If the electric field profile and the drift velocity as a function of electric field are used a similar result is obtained. The peaking time of the preamplifier is about 25 ns, which means that the pulse height depends on the integral of the signal.

As a result, the charge collected by a pixel can be computed as the number of electrons collected by the pixel, ignoring the holes, and the response of the detector can be computed using the drift properties of the electrons only.

6.4.4 Computation of the Lorentz angle in the test beam

Neglecting the electric field variation, the Lorentz angle can be computed directly with eq. 6.3 and eq. 6.6 using the parametrisations for the electrons and the mean electric field V_{bias}/d .

A more sophisticated computation was also developed, which computes the mean cluster size as function of angle evaluating the charge drift in silicon and taking in account the electric field profile inside the sensor, diffusion and threshold effects. The angle at which the cluster size is minimum is the model prediction of the Lorentz angle value.

To compute the cluster multiplicity the ionization charge was transported from the track to the pixel plane according to the drift trajectory obtained integrating numerically

$$\frac{dx}{dz} = \tan \Theta_L = r(T) \mu_d(T, E(z)) B$$

where x is the coordinate along the short direction of the pixels (the direction of the Lorentz force) and z is the coordinate perpendicular to the pixel plane (the direction of the electric force). The parametrisations of $r(T)$ and $\mu_d(T, E)$ were those presented in section 6.4.1 and 6.4.2.

The electric field profile $E(z)$ near a pn junction is shown in Fig. 2.1. The electric field is maximum at the pn interface. If the effective doping concentration is assumed to be uniform, the electric field varies linearly with position. With this assumption the electric field of irradiated sensors, which have a p-type conductivity and are not completely depleted, varies linearly from $2 \cdot V/d$ near the pixel (where the $n - p$ junction is located) to zero at the limit of depleted zone. In unirradiated devices which are over-depleted, the electric field varies linearly from $(V - V_d)/d$ near the pixels to $(V + V_d)/d$ at the junction located on the backside (where $V = 150$ V was the applied bias). The full depletion voltage V_d was determined to be 105 V for the not irradiated sensor [39].

Diffusion is also taken into account. For every point of the track, the diffusion of the generated electrons is related to the time needed to reach the pixels by eq. 6.4. The time can be computed numerically as

$$t = \int \frac{dz}{v_d(T, E(z))} = \int \frac{dz}{\mu_d(T, E(z)) E(z)}$$

Since the diffusivity coefficient of eq. 6.4 has only a weak dependence on the electric field [52] a value of $25 \text{ cm}^2 \text{ s}^{-1}$ (independently of E) was used.

Finally, to define hit pixels, a threshold is applied on the charge collected by every pixel.

The model parameters (bias voltage, depletion voltage, depletion depth, diffusivity, threshold, temperature, magnetic field) were all but one measured quantities. The only fit parameter was the threshold³. This was determined using data with no magnetic field present.

The model does not take in consideration energy loss fluctuations, the threshold dispersion, or delta rays. The uncertainty on the values obtained for the predicted Lorentz angle (Table 6.1) was estimated by varying the input depletion depths, the magnetic field and the mobility within their errors. The uncertainty on the parametrisation of the mobility was about 5% [52]. Other potential sources of errors proved to be negligible. The results obtained with the model described were within a fraction of degree of those obtained with eq. 6.3, 6.6 using the mean electric field V/d in the depleted region.

The prediction of the model for the cluster multiplicity are reported in Fig. 6.5, 6.6, 6.7 as dashed lines. The agreement with experimental data is satisfactory. The experimental and predicted Lorentz angle were compared in Fig. 6.12 and in Table 6.1. Taking into account the variation of the magnetic field, it is apparent that for irradiated sensors the Lorentz angle is smaller mostly because of the larger electric field.

³It was necessary to fit the threshold instead of using the value obtained by electronic calibration of the front end electronics because the sensors used for the measurements had a non uniform charge collection with losses along the edges of the pixel cells (section 4.1). This necessitated the extraction of an *effective* threshold from the data (which was about 20% higher than the real one).

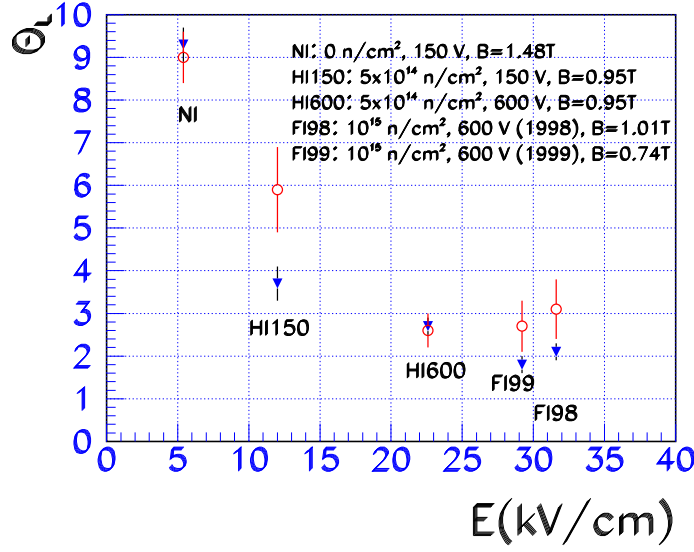


Figure 6.12: Lorentz angle measurement results. The dots are the experimental results, triangles are the expected values given by the model as a function of the mean electric field.

6.4.5 Computation of Lorentz angle in ATLAS

A prediction for the value of Lorentz angle in ATLAS was derived from eq. 6.3 and 6.6 with mean electric field and temperature as input parameters.

The silicon strips of the SCT detector are *p*-type implants on a *n*-doped substrate. Hence they collect the holes. As the hole mobility is much smaller than the electron one, the resulting Lorentz angle is much smaller. Hence the variation of Lorentz angle with bias voltage will have a much more significant impact on the detector response for the Pixel detector than for the SCT.

In fig. 6.13 the predicted Lorentz angle as a function of bias voltage is reported for Pixel and SCT sensors.

Bias voltages between 80 V and 600 V have been considered for the Pixels, and between 80 and 350 V for the SCT sensors. The bias will increase with time for both, to achieve full depletion despite radiation damage. The curves reported in the figure were computed using an electric field equal to the ratio between bias voltage and sensor thickness. This is the mean electric field inside the sensors if they are fully depleted. The thickness values are 200 μm for the Pixel B-Layer, 250 μm for Pixel Layers 1 and 2, 260 and 285 μm for SCT. Due to the different thickness, different Pixel layers have not the same Lorentz angle value for the same bias. The difference between the 260 μm and 285 μm thick layers of the SCT is negligible.

Finally, a temperature of 273 $^{\circ}\text{K}$ was assumed. An operating temperature of 264 $^{\circ}\text{K}$ would result in a slightly higher Lorentz angle, the difference being 0.2 $^{\circ}$ at 600 V and 0.6 $^{\circ}$ at 100 V for the Pixels, and negligible for the SCT.

It is evident that Lorentz angle dependence on bias voltage and thickness for

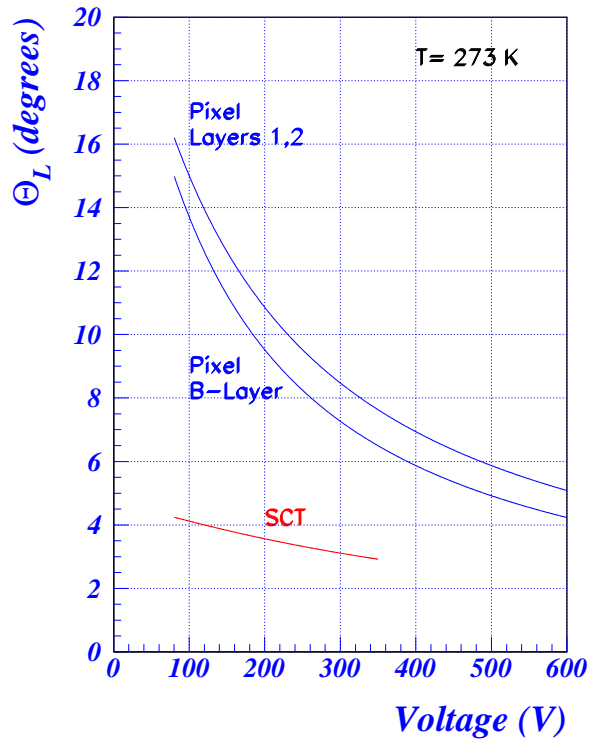


Figure 6.13: Lorentz angle in ATLAS silicon sensors as a function of applied bias voltage. Full depletion and $T = 273 \text{ }^{\circ}\text{K}$ are assumed.

the Pixel detector is quite large. Cluster multiplicity will depend on the Lorentz angle value. All the quantities which depends on cluster multiplicity, as spatial resolution and pixel occupancy, will be affected as well. As a consequence, the detector performances are expected to be a function of module bias.

The effect of the bias voltage on tracking and b -tagging performances is discussed in chapter 8.

Chapter 7

Spatial resolution analysis

7.1 General consideration

Spatial resolution is a key feature of the Pixel Detector, which has been conceived to provide three high precision track points at small radii. The spatial resolution it provides strongly contributes to the resolution on the impact parameter of tracks.

The order of magnitude of the Pixel spatial resolution is determined by the cell size. The choice between analog and digital readout, and the degree of charge sharing between adjacent pixels are also very important. The charge sharing is affected by intrinsic sensor properties (as inter pixel capacitance and pixel capacitance to the backplane), operational parameters (such as reverse bias operating voltage and radiation damage) and by parameters related to electronic readout (threshold, crosstalk, charge resolution etc.). A substantial role is also played by diffusion, by the incident particle track angle and by the Lorentz effects.

If there is no charge sharing between adjacent pixels, and all the charge carriers locally generated around the incident particle are collected on a single pixel (single hit clusters) then the spatial resolution is $\sigma = p/\sqrt{12}$, where p is the pitch. This is 14 μm in the short pixel direction, and 115 μm in the long pixel direction (for 400 μm pixels). If the ionization charge is collected on neighbouring pixels (two or more pixel clusters) charge interpolation becomes possible, which allows for improved resolution.

Much of the effort of test beam studies was devoted to resolution along the short (x) pixel direction. This was studied as a function of the incident track angle in the xz plane. The angle in the yz plane between incident particle tracks and the normal to the sensor plane was zero, so that only a small fraction of pixel clusters interested more than a column. The multi-column events were excluded from the analysis, so that the study of resolution was reduced to a one-dimensional problem. Unirradiated and irradiated sensors of various designs were studied.

Most of the results presented in this chapter use data taken without magnetic field. A study of the spatial resolution made with data taken with magnetic field is presented in section 7.5.4. As expected, the magnetic field changes the dependence of the resolution on the incidence angle shifting it by an amount

equal to the Lorentz angle.

| sensor | | 0° | 5° | 10° | 15° | 20° | 30° |
|--|----------|-------------|-------------|-------------|-------------|-------------|-------------|
| ST2 280 μm thick | % 1 hit | 76.8 | 64.6 | 36.6 | 6.8 | 3.2 | 1.8 |
| | % 2 hits | 20.9 | 33.9 | 61.3 | 85.3 | 49.8 | 3.3 |
| | % 3 hits | 1.2 | 0.9 | 1.3 | 7.0 | 44.7 | 39.2 |
| | % 4 hits | 0.5 | 0.3 | 0.4 | 0.4 | 1.3 | 53.3 |
| ST1 280 μm thick | % 1 hit | 67.5 | 40.7 | 9.6 | 0.2 | 0.0 | 0.2 |
| | % 2 hits | 29.5 | 55.6 | 84.8 | 68.7 | 21.0 | 0.1 |
| | % 3 hits | 1.7 | 1.9 | 3.3 | 28.1 | 74.3 | 10.8 |
| | % 4 hits | 0.6 | 1.0 | 1.2 | 1.7 | 2.8 | 82.2 |
| SSG 280 μm thick | % 1 hit | 66.7 | 41.2 | 5.9 | 1.3 | 0.7 | 0.2 |
| | % 2 hits | 30.4 | 55.0 | 87.3 | 61.3 | 21.2 | 0.6 |
| | % 3 hits | 1.6 | 2.0 | 4.3 | 34.2 | 73.7 | 14.8 |
| | % 4 hits | 0.6 | 0.8 | 1.3 | 1.9 | 2.4 | 78.5 |
| ST2 280 μm thick $10^{15} \text{ n}_{\text{eq}}\text{cm}^{-2}$ | % 1 hit | 90.6 | 87.3 | 74.1 | 52.5 | 30.4 | 6.4 |
| | % 2 hits | 8.4 | 11.7 | 25.0 | 46.0 | 66.9 | 65.4 |
| | % 3 hits | 0.6 | 0.6 | 0.4 | 1.0 | 2.2 | 26.2 |
| | % 4 hits | 0.2 | 0.2 | 0.2 | 0.3 | 0.4 | 1.1 |
| ST2 280 μm thick $0.5 \times 10^{15} \text{ n}_{\text{eq}}\text{cm}^{-2}$ | % 1 hit | 83.6 | 66.6 | 42.7 | 11.0 | 2.4 | 2.0 |
| | % 2 hits | 14.5 | 31.7 | 55.1 | 83.1 | 63.3 | 5.9 |
| | % 3 hits | 1.3 | 1.1 | 1.4 | 4.9 | 32.2 | 70.6 |
| | % 4 hits | 0.4 | 0.3 | 0.4 | 0.6 | 0.9 | 20.5 |
| SSGb 200 μm thick | % 1 hit | 82.5 | 71.3 | 49.5 | 25.8 | | 0.6 |
| | % 2 hits | 15.9 | 27.1 | 48.2 | 71.4 | | 34.7 |
| | % 3 hits | 0.8 | 0.9 | 1.3 | 1.7 | | 62.1 |
| | % 4 hits | 0.4 | 0.4 | 0.5 | 0.6 | | 1.6 |
| SMD 250 μm thick $10^{15} \text{ n}_{\text{eq}}\text{cm}^{-2}$ | % 1 hit | 85.9 | 82.6 | 57.6 | 35.1 | 13.7 | 7.2 |
| | % 2 hits | 12.4 | 15.9 | 40.1 | 61.9 | 76.6 | 39.8 |
| | % 3 hits | 1.0 | 0.9 | 1.1 | 1.9 | 8.1 | 49.2 |
| | % 4 hits | 0.4 | 0.4 | 0.5 | 0.5 | 0.9 | 2.8 |

Table 7.1: Distribution of cluster sizes in the short pixel direction, as a function of incident particle track angle and for various sensor designs. The two most populated cluster sizes were enlightened with bold font for each sensor design and angle. Applied bias voltage was 150 V for unirradiated sensors, 600 V for irradiated ones. The SMD sensor was built with oxygenated silicon substrate, all the other sensors used standard silicon. No data were available for SSGb sensor at 20°.

In table 7.1 the cluster multiplicity (i.e. cluster size) distribution is reported for various sensor designs as a function of track incidence angle. This distribution is important for the spatial resolution because, as noted above, a poorer resolution is expected for the single pixel clusters for which no charge interpolation is possible. The following observations can be made about the values in the table:

- At any given angle the mean multiplicity was larger for the sensor with better charge collection (section 4.1). This is expected to result into a better spatial resolution.

The mean cluster size was smaller for the unirradiated 280 μm thick ST2 sensor than for the equivalent ST1 and SSG sensors which had not the charge collection problem. It was smaller for the 200 μm thick SSGb sensor because it was thinner. It was smaller for partially depleted irradiated sensors than for their unirradiated equivalents.

The SMD sensor had the same thickness (250 μm) the same design and the same type of substrate (oxygenated silicon) of the sensors which will be used in the ATLAS Pixel barrel layers 1 and 2 and in the disks. It was irradiated to $10^{15} \text{ n}_{\text{eq}}\text{cm}^{-2}$. It had a better charge collection than the thicker ST2 sensor irradiated to the same fluence, both because of the larger depletion depth provided by the use of oxygenated silicon and because of the absence of the charge loss problem. This resulted in a larger mean cluster size for the SMD sensor.

- The single hit clusters, for which no charge interpolation is possible, were the most populated class at normal incidence. However a significant fraction of double pixel clusters was also present. This ranged from 8% for the ST2 sensor irradiated to the higher fluence, up to the 30% for the 280 μm thick unirradiated SSG and ST1 sensors. Increasing the angle of incidence, the mean cluster size increased and the single pixel clusters gradually disappeared.
- For any given angle and sensor design there are two cluster sizes (enlightened with bold font) to which nearly all cluster belongs. Higher cluster sizes occurs because of δ -ray production, lower cluster sizes because of inefficiencies.

| | Barrel before radiation damage | Barrel after radiation damage | Disks |
|--|-----------------------------------|----------------------------------|-------|
| Average angle of incidence α ($^\circ$) | 20 | 20 | 0 |
| Assumed bias voltage | 150 | 600 | - |
| Lorentz angle Θ_L ($^\circ$) | 12 | 5 | 0 |
| $\alpha - \Theta_L$ ($^\circ$) | 8 | 15 | 0 |

Table 7.2: Average angle of incidence and Lorentz angle in the ATLAS Pixel detector. Resolution depends on the difference between the two. The Lorentz angle in the barrel depends on the assumed bias voltage (Fig. 6.13).

As the spatial resolution varies with the angle of incidence (section 7.5) it is important to keep in mind the average values of this angle in ATLAS (table 7.2). The incidence angle of the particles will have a spread of several degrees around the average value, due to the curvature of tracks in the magnetic field (at low transverse momenta) and the finite module size. The Lorentz angle depends on the bias voltage (Fig. 6.13) so that the difference between the average incident angle and the Lorentz angle also depends on the operating voltage.

7.2 Digital and analog reconstruction

The position of single pixel clusters is given by the pixel center position. Two different algorithms were used to reconstruct the spatial position of two pixels

clusters. A *digital* algorithm which uses the center position between the two pixels and an *analog* algorithm that corrects the digital position just described using an interpolation of the charge collected by the two pixels. The variable used for the correction was $\eta = Q_r/(Q_r + Q_l)$ where Q_r and Q_l are the charges collected by the right hand side and the left hand side pixels in the cluster respectively.

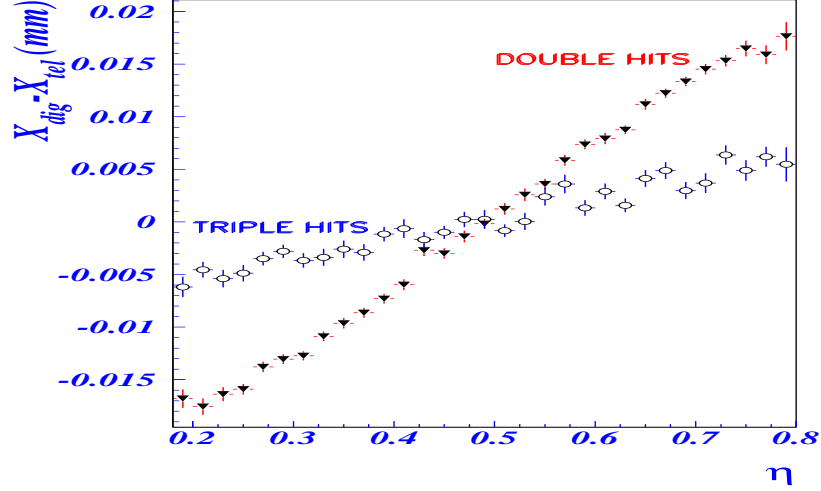


Figure 7.1: Difference between position measured by the telescope and by the pixel detector with digital information alone, plotted against the variable η (defined in the text). Data were taken with an ST1 device for an angle of incidence of 15° .

Fig. 7.1 shows the correlation between this variable and the digital residual (the difference between the position measured by the pixel detector and the track extrapolation provided by the telescope). The following interpolation was adopted [47]:

$$x_{\text{an}} = x_{\text{dig}} + 2\Delta \left(\frac{1}{N_0} \int_0^\eta \frac{dN}{d\eta} d\eta - \frac{1}{2} \right) \quad (7.1)$$

where x_{an} and x_{dig} are the spatial positions reconstructed by the analog and digital algorithms respectively. This formula corrects for the possible nonlinearities in the relation between η and the position, by using a position correction proportional to the integral of the event distribution $dN/d\eta$. This assumes that the N_0 particles are spread uniformly over an interval 2Δ . The uniformity is true because the pixel pitch is much smaller than the beam spot size.

The amplitude of the correction Δ must be chosen to optimize spatial resolution. This is obtained when the analog residual does not depend on η . The optimal value of Δ is the mean digital residual as η approaches its extremal values 0 and 1. It was evaluated from plots like the one in Fig. 7.1 and parametrized as a function of the angle for each tested sensor.

An equivalent procedure was adopted for multi-pixel clusters. These occur

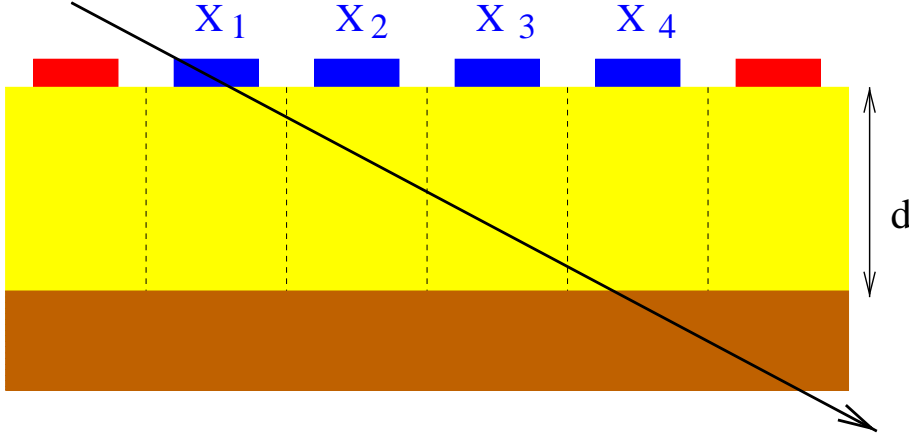


Figure 7.2: Sketch of a sensor traversed by a track at an angle. The sensor has been sketched as partially depleted, and the hatched zone correspond to the not depleted region.

when particles traverse the pixel sensor at an angle (Fig. 7.2). For inclined particle trajectories, the charge is collected over a region approximately given by $d \times \tan \phi$, where d is the sensor depletion depth. Charged particles with large incident angles produce signals on many pixels and the average charge per pixel decreases, despite the longer trajectory in the silicon. The digital position is computed as the mean position of the pixels in the cluster, $x_{\text{dig}} = \Sigma_i x_i / N$. For the analog position only the edge pixels in the cluster are considered. The signal amplitude on the central pixels does not carry information on the position of the passing particle because the pathlength under the pixel is $p / \sin \alpha$ and does not depend on position. Hence η is computed using the first and the last pixel in the clusters [49, 56].

Fig. 7.1 shows that the correction to be applied depends on the number of pixels in the cluster (i.e. the cluster multiplicity), so it is convenient to treat different cluster sizes separately. This means that there is a distribution $dN/d\eta$ and a value of Δ for every cluster multiplicity. The figure shows that the optimal value of Δ for data taken with ST1 sensors at 15° is $17 \mu\text{m}$ for two pixel clusters and $7 \mu\text{m}$ for three pixel clusters.

As the track length under a pixel is geometrically limited by $p / \sin \alpha$ charges on a pixel exceeding $Q_{\text{cut}} = \lambda p / \sin \alpha$ (where λ is the number of electrons generated per unit pathlength) are due to energy loss fluctuations. The impact of these fluctuations on spatial resolution was reduced by setting pulse heights exceeding Q_{cut} to Q_{cut} , when computing η .

Digital and analog spatial resolutions for one of the tested devices are shown in Fig. 7.3. The device was a $280 \mu\text{m}$ thick unirradiated SSG sensor. At normal incidence most of the clusters are single pixel clusters (table 7.1) so that there is little difference between digital and analog resolution. As the angle increased, the single pixel clusters disappear and analog reconstruction provides a strongly improved spatial resolution.

The resolution on the extrapolated track position (telescope resolution) has

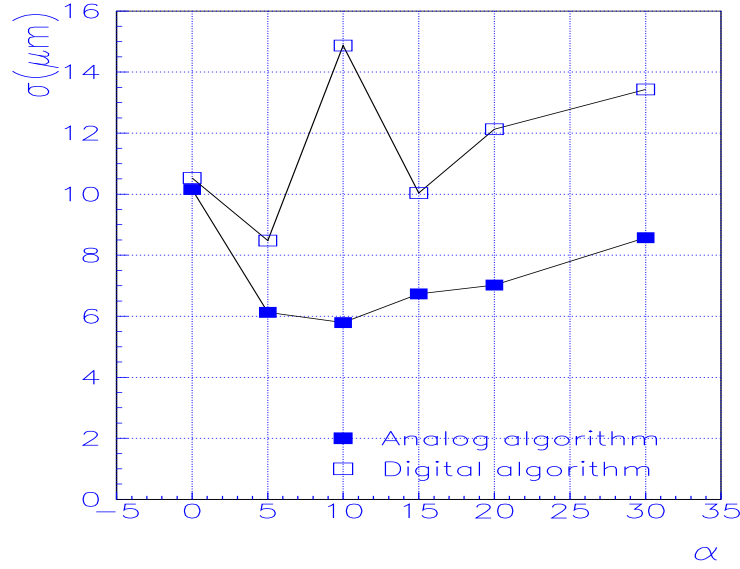


Figure 7.3: Spatial resolution with digital and analog reconstruction of pixel cluster position, for an unirradiated SSG device as a function of the angle of incidence. The telescope extrapolation uncertainty has not been subtracted.

not been subtracted from the pixel resolutions reported in Fig. 7.3. This is a conservative choice, due to the difficulty of precisely estimating the telescope resolution. The next section discusses how the telescope resolution was evaluated and improved. A detailed discussion of the spatial resolution of the various pixel sensor designs at normal incidence and as a function of the angle of incidence will follow.

7.3 Telescope resolution

Spatial resolution was determined by computing the residuals between the coordinate measured by the pixel detector and that predicted by the silicon microstrip telescope. The extrapolation uncertainty depends on many parameters, e.g. the position of the microstrip planes and of the pixel detector under study, the microstrip intrinsic resolution, the amount of material along the beam path etc. Telescope resolution was improved applying a tighter selection on track reconstruction χ^2 probability in the xz view. This operation allowed to improve the resolution of the microstrip telescope, but it decreased the available statistics and it increased the statistical error on the resolutions.

Keeping 20% of events, the measured detector resolution increased significantly (Fig. 7.4) showing that the measured value received indeed an important contribution from the telescope extrapolation uncertainty. The statistical errors on the measured detector resolutions after this selection were of the order of $0.3 \mu\text{m}$.

In order to study the telescope resolution, data taken at normal incidence

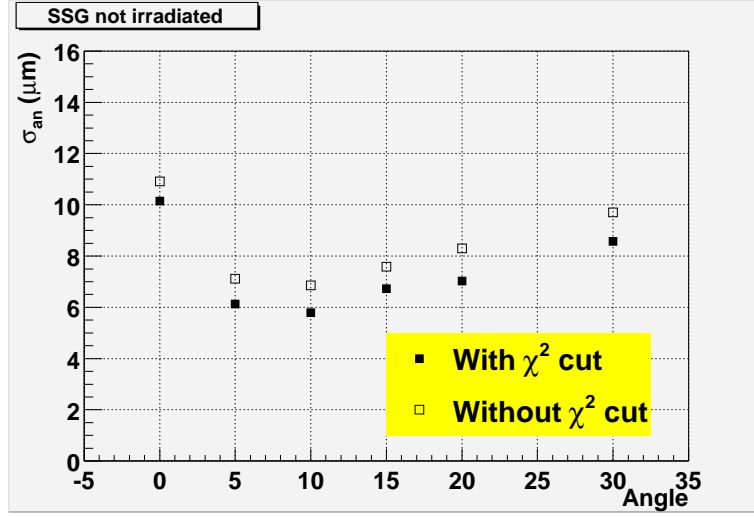


Figure 7.4: Measured analog spatial resolution for an unirradiated SSG device as a function of the angle of incidence, before and after the quality cut on the tracks reconstructed by the silicon microstrip telescope.

were used. At normal incidence mainly single pixel and double pixel clusters occur. The resolution is determined by their relative abundance. Single pixel and double pixel clusters were studied separately. Examples of such residuals distributions are shown for a modified SSGb 200 μm thick sensor in Fig. 7.5 and Fig. 7.6. The first figure has been produced with all the cuts used in the resolution analysis, while the second figure was made without the quality cut on telescope track described above - only the standard cuts described in section 3.2 were applied.

Single pixel clusters occur when incident particles cross the pixel central region of width $L = p - 2\Delta$ where Δ is the charge sharing region. Then for single pixel cluster the distribution is parametrized with a uniform distribution of width L , convoluted with a gaussian distribution of width $\sigma_{mbot\text{tel}}$ that takes into account the resolution of the silicon microstrip telescope, threshold effects and δ -rays. The result of this fit (Fig. 7.5c) was $\sigma_{\text{tel}} = 3.4 \pm 0.5 \mu\text{m}$ and $L = 44.0 \pm 0.4 \mu\text{m}$ for the extension of the region at the centre of the pixel where the charge is collected by a single pixel. The corresponding value for the extension of the charge-sharing region is $\pm 3 \mu\text{m}$ around the pixel border. σ_{tel} increases to $4.5 \pm 0.3 \mu\text{m}$ without the quality cut on the telescope tracks.

The residuals distribution of the double pixel clusters allows an independent measurement of the telescope resolution. Because of the very limited width of the region of charge sharing, those residuals allow a very precise determination of the crossing point of the beam particle. The residuals distribution for a digital algorithm is expected to be a uniform distribution of width $\pm 3 \mu\text{m}$ convoluted with a gaussian describing the telescope resolution: the resulting distribution is shown in Fig. 7.5a and Fig. 7.6a together with gaussian fits giving a sigma of $5.2 \mu\text{m}$ before the track quality cut and $3.2 \mu\text{m}$ after it. Since the r.m.s. of a uniform distribution of width ± 3 micron is only 1.7 micron, the telescope

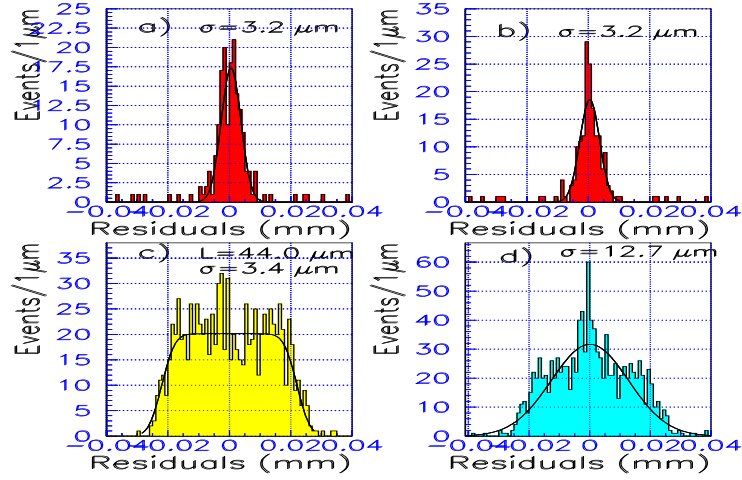


Figure 7.5: Residuals between position measured by the telescope and by pixel detector for a 200 μm thick SSGb sensor at 0° . The selection on telescope track quality described in the text has been applied. a) Double hits residuals (digital algorithm). b) Double hits residuals (analog algorithm). c) Single hits residuals. d) Total residuals distribution (analog algorithm).

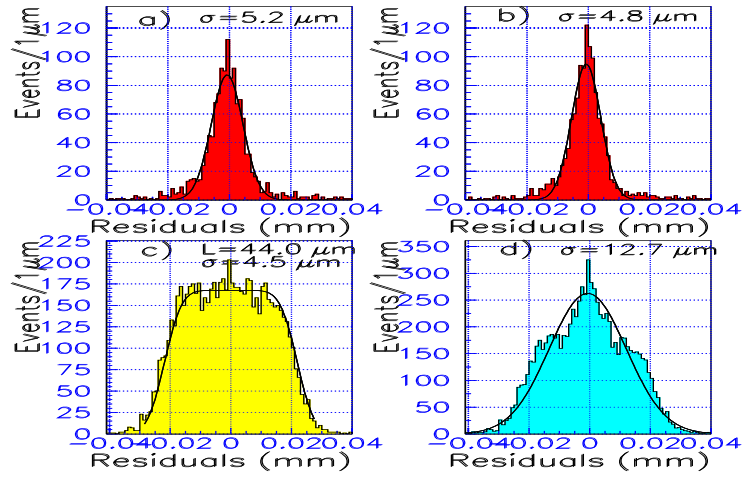


Figure 7.6: Same as above, but without the χ^2 cut on the track quality (only the standard cuts described in section 3.2 applied).

resolution is $4.9\text{ }\mu\text{m}$ before the track quality cut and $2.7\text{ }\mu\text{m}$ after the cut, with a statistical error of about $0.3\text{ }\mu\text{m}$. These numbers are in agreement within errors with the telescope resolution as evaluated from the single pixel clusters distribution.

Similarly, the residuals distribution for the analog algorithm produces a distribution dominated by the telescope resolution, particularly before the track quality cuts: Fig. 7.5b and Fig. 7.6b show such distributions with a gaussian fit giving $4.8\text{ }\mu\text{m}$ before the track quality cut and $3.2\text{ }\mu\text{m}$ after it.

The digital residuals distributions of single-pixel and two-pixel clusters have been used to measure extensively the telescope resolution for the various beam telescope setups used. Averaging the two determination of the telescope resolution, a value of 2.9 ± 0.3 is found for the run discussed in detail above after the track quality cuts. Two not irradiated $200\text{ }\mu\text{m}$ thick devices were under test and the 1999 telescope setup was in use. This is actually the best value measured in the test beam. The 1998 telescope setup had a worse resolution, and worse resolution are measured when thicker or irradiated devices are under test because of the additional material (irradiated devices were kept inside a cold box to maintain them at low temperature). At 0° telescope resolution values between 2.9 and $4.6\text{ }\mu\text{m}$ were measured (without the quality cut, values between $4.5\text{ }\mu\text{m}$ and $6.0\text{ }\mu\text{m}$ were found).

At higher angles slightly worse values were measured, due to the projection on the pixel detector plane (which yields a telescope resolution proportional to $1/\cos\alpha$) and the presence of more material along the beam when detectors were tilted.

The procedure described to evaluate the telescope resolution assumes that the smearing of the residual distributions introduced by the telescope extrapolation error is much larger than the smearing introduced by threshold fluctuations, noise, energy loss fluctuations etc. This assumption may lead to an overestimate of the telescope resolution. As these systematic effects (in particular the impact of energy loss fluctuations) are difficult to evaluate for any data taking configuration, the pixel resolution figures quoted in this thesis are not corrected for telescope extrapolation uncertainty. Hence, they are conservative upper limits for the pixel sensor spatial resolution.

The quoted values are the standard deviations evaluated by fitting the residual distributions with a Gaussian function.

7.4 x-spatial resolution at normal incidence

At 0° the resolution depends on the relative fraction of single and multi-hit clusters. Charge sharing occurs when the particles transverse the sensor within a distance Δ from the pixel border, while single hit clusters result from particle which transverse the sensor in a region of width $L = p - 2\Delta$ near the pixel centre. The widths of the digital residuals distributions of single-pixel and two-pixel clusters are L and 2Δ respectively (plus the contribution from the telescope resolution). The fraction of single-pixel and two-pixel clusters is L/p and $2\Delta/p$ respectively. At normal incidence $2\Delta < L$ and the wider and more populated single pixel residual distribution dominates the digital spatial resolution. The analog reconstruction of position makes the two-pixel cluster residuals distribution narrower, but it leaves unchanged the single-pixel clusters

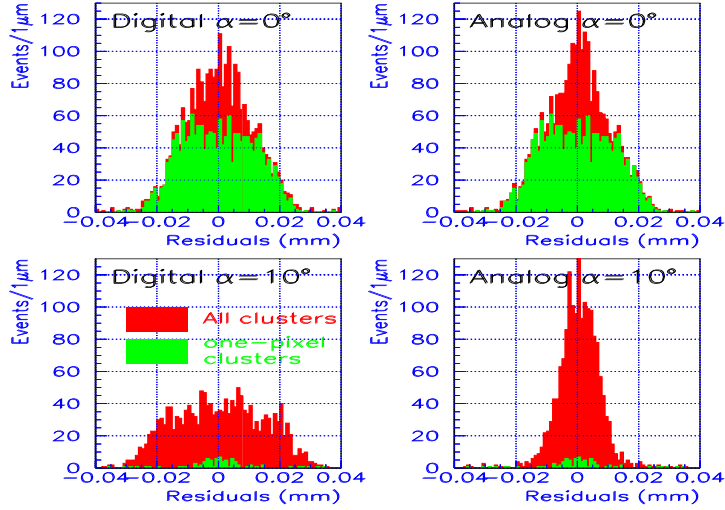


Figure 7.7: Spatial resolution residuals for a $280\ \mu\text{m}$ thick unirradiated SSG sensor, at 0° and 10° incidence angles. Analog and digital reconstruction residuals are shown. Single pixel cluster and double pixel cluster contributions to the residual distributions are distinguished by different colors.

distribution (Fig. 7.7). As a result, analog resolution is also mostly determined by the single hits and it is in fact not very different from digital resolution at normal incidence.

The combined distribution of single and double pixel clusters at normal incidence for the SSGb $200\ \mu\text{m}$ thick sensor is reported in Fig. 7.5d and has a standard deviation of $12.7\ \mu\text{m}$ (the rms is $14.0\ \mu\text{m}$). Fig. 7.7 reports the analog and digital residuals distributions for a $280\ \mu\text{m}$ thick SSG sensor. Double-pixel and single-pixel clusters contributions to the residuals distribution are distinguished by different colors. The single-pixel cluster residuals distribution at normal incidence is wider and more populated even for this sensor, which has the largest fraction of double hits (table 7.1).

The relative weight of single-pixel and double-pixel-clusters are listed in Table 7.1 for different sensor designs and irradiation levels. Table 7.3 reports the width of the charge sharing region digital and analog spatial resolution at normal incidence. As anticipated, there is not much difference between digital and analog resolutions at normal incidence, but differences appear between different sensor designs. Devices which collected more charge (either due to their larger thickness, or because they were fully depleted or since the design had negligible charge loss, as the ST1 and SSG layouts) produced less single pixel clusters, located in a narrower region (i.e. L was smaller) and therefore had better resolution. As a consequence unirradiated $280\ \mu\text{m}$ thick devices provided resolutions superior than the not fully depleted irradiated sensors or the $200\ \mu\text{m}$ thick sensors. The ST2 devices had worse resolution than SSG and ST1 sensors,

| Design isolation | ST2 p-spray | ST1 p-stop | SSG p-spray | ST2 p-spray | ST2 p-spray | SSGb p-spray | SMD ⁺ p-spray |
|------------------------------------|-------------|------------|-------------|-------------|---------------------|--------------|--------------------------|
| Fluence ($n_{eq}cm^{-2}$) | 0 | 0 | 0 | 10^{15} | $0.5 \cdot 10^{15}$ | 0 | 10^{15} |
| Bias (V) | 150 | 150 | 150 | 600 | 600 | 150 | 600 |
| Depletion depth (μm) | 280 | 280 | 280 | 190 | 260 | 200 | 230 |
| Thickness (μm) | 280 | 280 | 280 | 280 | 280 | 200 | 250 |
| Normal incidence: | | | | | | | |
| Charge sharing region (μm) | 9.2 | 13.6 | 14.0 | 3.5 | 5.8 | 6.2 | 4.3 |
| Digital resolution | 12.1 | 10.7 | 10.5 | 13.7 | 13.1 | 12.7 | 12.5 |
| Analog resolution | 12.0 | 10.4 | 10.1 | 13.7 | 12.9 | 12.6 | 12.4 |
| Best analog resolution (μm) | 6.5 | 5.3 | 5.8 | 9.0 | 7.3 | 6.2 | 7.4 |
| Corresponding angle | 10° | 10° | 10° | 15° | 10° | 15° | 15° |

⁺ Oxygenated silicon substrate and moderated p-spray isolation.

Table 7.3: Measurements of spatial resolution. Telescope extrapolation uncertainty not subtracted.

as a consequence of charge collection inefficiencies.

7.5 x-spatial resolution as a function of the angle of incidence

Finally, the dependence of the resolution on the angle α of the incident particle with respect to the sensor surface was studied. The standard deviations of the all-cluster residual distributions are shown in Fig. 7.8 (using a digital algorithm) and in Fig. 7.9 and 7.10 (analog algorithm). The data were not corrected for the silicon microstrip telescope extrapolation uncertainty.

7.5.1 Digital resolution

As the tilt angle is increased, the width 2Δ of the charge-sharing region increased. The single-pixel residuals distribution gets narrower and resolution improves. The best resolution is obtained when $L = 2\Delta = 25 \mu m$, that is, when the single-pixel and two-pixel distributions are equally populated and with the same width. In this situation the digital resolution is $25 \mu m / \sqrt{12} = 7.2 \mu m$. If a telescope resolution of $4 \mu m$ is added in quadrature, this number becomes $8.2 \mu m$. Such a resolution is measured for the SSG and ST1 sensors at 5° incidence angle (Fig. 7.8) which have indeed a similar number of single-pixel and two-pixel clusters (table 7.1). If the angle is further increased, the two-pixel clusters become dominant. For an SSG detector at 10° incidence angle 87% of the clusters are made of two pixels. The digital residuals distribution (Fig. 7.7) has a width of about $50 \mu m$ and the resolution is about $50 \mu m / \sqrt{12} = 14.4 \mu m$. If the telescope resolution is added this becomes $14.9 \mu m$ which is indeed very close to the measured value (Fig. 7.8).

At any given angle about 98 % of clusters are formed from only two cluster sizes (see Table 7.1). When they are equally populated a digital resolution of the order of $7.2 \mu m$ is expected. When the angle is such that nearly all of the events belong to one multiplicity only, the digital resolution is about $14.4 \mu m$. Then the digital resolution as a function of angle shows a structure of alternating minima and maxima. The angular position of minima and maxima depends on the charge collection properties of the device which influence the cluster multiplicity. For example, for $280 \mu m$ thick sensor devices with negligible

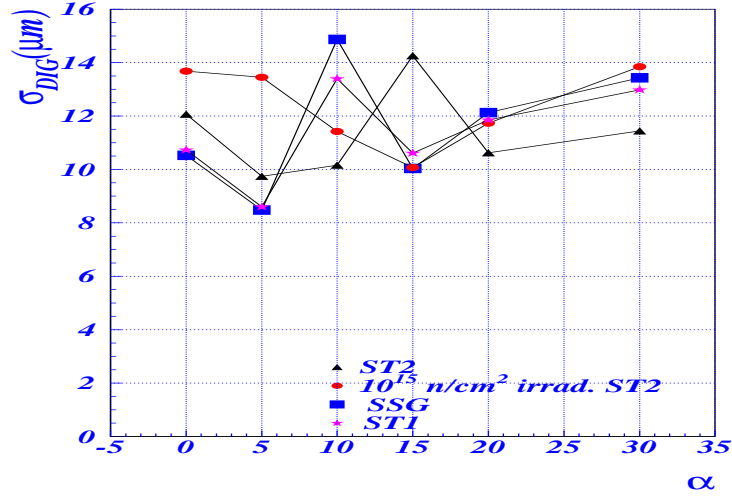


Figure 7.8: Measured digital resolution without subtraction of telescope extrapolation uncertainty.

charge loss (SSG and ST1), the position of first minimum was obtained at 5° . This angle is larger for the ST2 design, since it suffers from charge loss and even larger for an irradiated ST2 operating underdepleted. However the values of resolution at maxima and minima are determined by the pixel pitch only.

7.5.2 Analog resolution

The spatial resolution obtained with the analog algorithm (Fig. 7.9 and 7.10) was always better than the corresponding digital resolution once the incidence angles were larger than 0° . The best resolution value occurs when the proportion of single pixel clusters becomes negligible. This occurred at 10° for the unirradiated $280 \mu\text{m}$ thick devices and at 15° for partially depleted or thinned sensors. As the angle of incidence increases further, the charge collected by every pixel is reduced. Energy loss fluctuations affect the measurement of η and degrade the resolution. Such an angular dependence is observed for all the designs.

The best resolution for an unirradiated sensor is $5.3 \mu\text{m}$ ($3.2^{+0.8}_{-1.2} \mu\text{m}$ if telescope error is subtracted¹). The best resolution for a device irradiated to $10^{15} \text{ n}_{\text{eq}}\text{cm}^{-2}$ is $7.4 \mu\text{m}$, ($6.0^{+0.5}_{-0.6} \mu\text{m}$ after subtraction of telescope extrapolation error²).

The spatial resolution is related to the amount of collected charge. The devices with the best resolution are those with unirradiated $280 \mu\text{m}$ thick sensor (Fig. 7.9). The ST2 sensor, which has the problem of reduced charge collection efficiency near the pixel borders (Fig. 4.1), has a significantly worse resolution than the ST1 and SSG sensors. These use p-stop and p-spray isolation respec-

¹Statistical error only

²Statistical error only

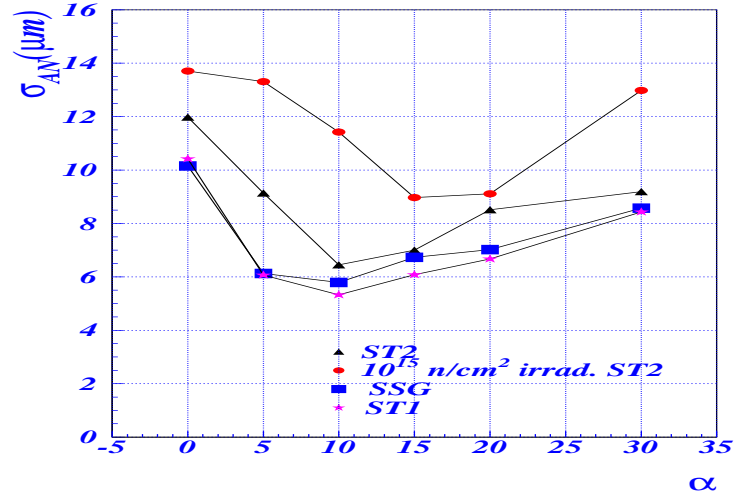


Figure 7.9: Measured analog resolution without subtraction of telescope extrapolation uncertainty (1998 data).

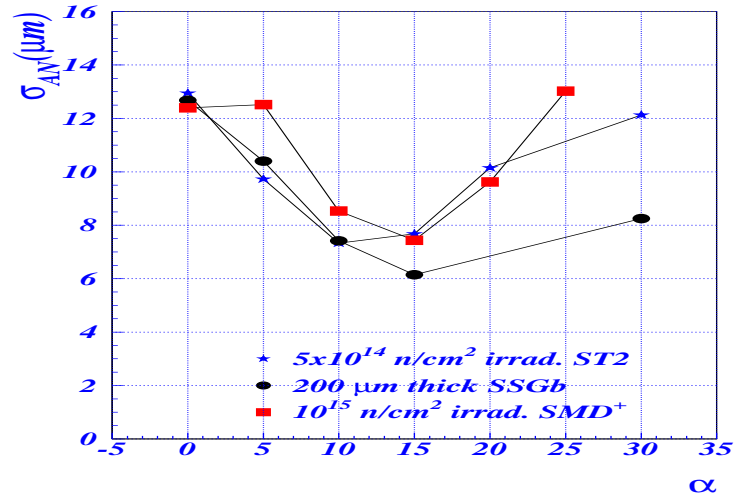


Figure 7.10: Measured analog resolution without subtraction of telescope extrapolation uncertainty (1999 and 2000 data).

tively and have both a good charge collection uniformity. Their resolution is similar.

The final design has an even better charge collection uniformity, but no sensor with 280 μm thickness has been produced with the new design. Instead, a 200 μm sensor has been studied (Fig. 7.10). The best resolution (without telescope subtraction) is 6.2 μm , to be compared to the 5.8 μm resolution of the thicker SSG sensor.

The spatial resolution is degraded by irradiation. This is true in particular for the ST2 sensor irradiated to $10^{15} \text{ n}_{\text{eq}}\text{cm}^{-2}$, which has a reduced charge collection after irradiation because of partial depletion. The ST2 sensor irradiated to $5 \times 10^{15} \text{ n}_{\text{eq}}\text{cm}^{-2}$, which is almost fully depleted, suffers only a modest resolution degradation relatively to the unirradiated sensor.

The SMD sensor irradiated to $10^{15} \text{ n}_{\text{eq}}\text{cm}^{-2}$ demonstrates the superiority of the new sensor design and of the oxygenated substrate; it has a significantly better resolution than its ST2 equivalent (7.4 μm instead of 9.0 μm the best value) because of the absence of charge losses and because it is fully depleted.

7.5.3 Analog resolution without ToT calibration

A preliminary study of the importance of the calibrations for the pixel spatial resolution was performed with the test beam data. The raw Time Over Threshold information was used to compute η for position reconstruction with the analog algorithm and the resulting resolution was compared to that obtained using calibrated data.

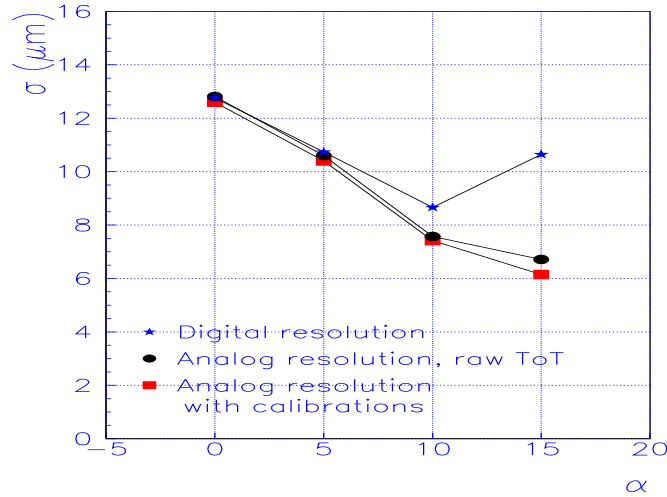


Figure 7.11: The plot compares digital resolution, analog resolution making use of calibrated charge and analog resolution making use of raw Time Over Threshold information, as a function of the beam incidence angle. Data were taken with a 200 μm thick unirradiated sensor with SSGb design.

The comparison is shown in Fig. 7.11. Data were taken with the 200 μm thick unirradiated SSGb sensor. At normal incidence resolution is dominated

by the single-pixel cluster residuals and there is no sensible difference between the three resolutions.

At 15° incidence angle there are almost no single-pixel clusters left and the analog resolution with calibrated charge is $6.2 \mu\text{m}$. This resolution is degraded to $6.7 \mu\text{m}$ when raw ToT is used instead of calibrated charge.

A relatively modest degradation of resolution in absence of calibration is observed because the differences between the response of nearby pixels, which are taken into account by the calibration, are small compared to the other effects that provide an intrinsic limit to the analog resolution even after calibrations (ToT digitization, energy loss fluctuations, threshold dispersion, noise, ...). The nonlinearities in the pixel response, which are removed by the calibration, do not affect the spatial resolution because the analog algorithm already takes them into account by using the integral distribution of η for the correction to the digital position.

7.5.4 Spatial resolution in the presence of a magnetic field

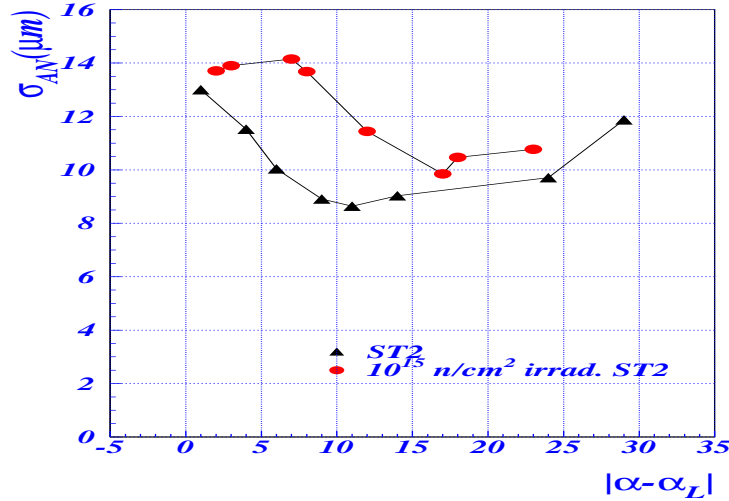


Figure 7.12: Measured analog resolution inside a magnetic field as a function of the difference between the beam incidence angle and the Lorentz angle. Telescope extrapolation uncertainty was not subtracted.

It is expected that the effect of a magnetic field on the resolution is to shift the angular dependence by a quantity equal to the Lorentz angle. In Fig. 7.12 the analog resolution for data taken with a magnetic field is shown as function of the absolute value of the difference between the incidence angle and the measured Lorentz angle. The pattern is the same of that in Fig. 7.9, but with worse values of resolution. The difference is consistent however with an observed increase in the telescope extrapolation error from $\sim 4 \mu\text{m}$ to $\sim 6 \mu\text{m}$. This is due to the fact that in the presence of a magnetic field the four track points provided by the strip planes are fitted with a parabola (three free parameters) while when data

are taken without a magnetic field the fit is made with a straight line (two free parameters). This results in a bigger uncertainty on the fit parameters when a magnetic field is present.

7.6 y-spatial resolution

For small incidence angles charge sharing has no influence on the spatial resolution in the $400\text{ }\mu\text{m}$ long direction of the pixel since it is restricted to a relatively small region. The corresponding y residuals have a flat distribution extending from $-200\text{ }\mu\text{m}$ to $+200\text{ }\mu\text{m}$ giving an rms of $115\text{ }\mu\text{m}$. In order to achieve enhanced y -resolution a bricked structure was designed and tested. The sensor had $400\text{ }\mu\text{m}$ long pixels in adjacent columns staggered by $200\text{ }\mu\text{m}$ in the long direction of the cell. With the bricked design the y -resolution for single hit clusters is the same as for non-bricked layout, while for clusters with charge sharing (in the x direction) the residuals should have a flat distribution extending for $200\text{ }\mu\text{m}$ with an rms of $58\text{ }\mu\text{m}$. The overall resolution thus depends on the fraction of clusters with two or more hits. The resolution was measured for angles (in the xz plane) ranging from 0° to 30° (Fig. 7.13). The fraction of clusters with ≥ 2 pixels varied from 46 % at 0° to 98 % at 30° , yielding values of $62 - 67\text{ }\mu\text{m}$ for resolution between 10° and 30° . No variation of the x resolution was observed with respect to the not bricked design.

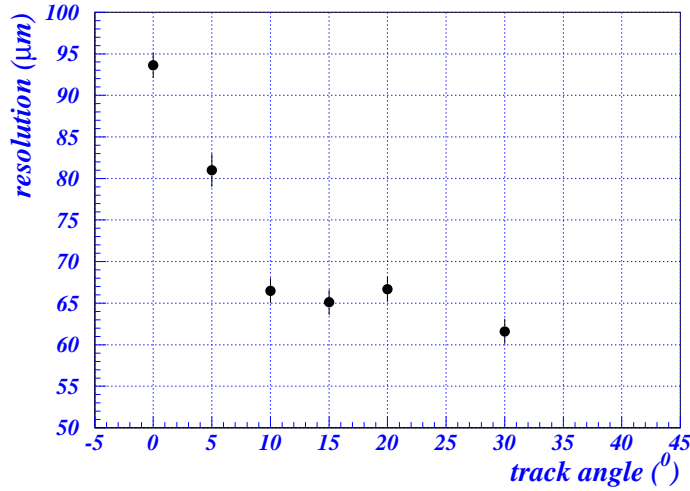


Figure 7.13: Resolution in the long direction of the pixel for a bricked design sensor as a function of the track angle with respect to the normal to sensor.

7.7 Conclusions

The test beam data have been used to study the spatial resolution as a function of the angle of incidence for unirradiated and irradiated sensors with different designs and thicknesses. Two strategies for the reconstruction of the cluster position were examined: one which makes use of the information on the charge collected by each pixel (analog reconstruction) and one which does not use it (digital reconstruction).

The dependence of both analog and digital resolution on the amount of charge sharing between pixels has been put in evidence. The analog reconstruction offers a much improved performance when multi-hit clusters dominate over single-pixel clusters. This occurs for not-normal incidence.

The importance of a good charge collection has also been put in evidence. Devices collecting more charge show better spatial resolution at all angles.

The pixel sensors developed for the ATLAS experiment are able to meet the desired spatial precision. Sensors with the designs (SSG,SSGb and SMD) close to the final one show resolutions better than $8\text{ }\mu\text{m}$ at the angles more relevant for the barrel part of the ATLAS detector. This holds for both the unirradiated sensors and the sensor irradiated to $10^{15}\text{ n}_{\text{eq}}\text{cm}^{-2}$ fluence. Resolutions between $10\text{ }\mu\text{m}$ and $12\text{ }\mu\text{m}$ have been obtained at normal incidence, which is relevant for the ATLAS Pixel disks, both before and after irradiation.

Chapter 8

ATLAS b -tagging and tracking performance

In the simulation of ATLAS detector performance the position of the track hits in the Pixels had always been reconstructed using the digital information only. This chapter investigates the effect of using an algorithm which makes use of the ToT information to determine the pixel clusters position. Test beam studies have proven that the pixel spatial resolution can be significantly improved for clusters with more than a pixel. The fraction of multi-pixel clusters depends on the track incidence angle and the Lorentz angle. The Lorentz angle depends on the bias voltage, so the Pixel detector spatial resolution for high energy muons has been investigated for various values of applied bias voltage (section 8.2). An improvement of analog resolution for larger bias voltages is observed. In section 8.3 the resolution on the parameters of reconstructed tracks is investigated. Finally, the impact of the improved impact parameter resolution on the b -tagging performance is discussed in section 8.4.

8.1 Simulation and reconstruction software

8.1.1 ATLAS detector simulation

The current ATLAS simulation program [6] makes use of the GEANT package (version 3.21) [57]. A FORTRAN-based macro language (AGE, Atlas GEant) is used to set up detector description banks, to implement the detector geometry and to define hits and digit structures associated with it. The detector description parameters can be overwritten interactively via datacards, allowing the user to change the default values.

A new version of the simulation program, based on object-oriented C++ software, is being produced; the FORTRAN-based package will be kept updated until the new version will be completed.

The ATLAS simulation program can be logically divided into three modules: event generation, detector simulation and digitization. These three parts communicate through a set of ZEBRA banks and can be run separately or in sequence.

The **event generation** phase is often run separately in order to have a

consistent input stream which can be used many times. Various event generators can be used and interfaced with GEANT.

The detector **simulation** part is the most time-consuming. Most of the CPU is spent in simulating the showers in the calorimeters. It can be run with different initial conditions (*e.g.* geometrical setup) on the same set of physics events in order to understand the impact of a change in the detector on the physics performance. The particle four-vectors are tracked through the various detector systems. For those parts of the detector which have been declared sensitive, informations on the energy deposition (*hits*) are recorded. The information collected in the hits banks, although dependent on the geometry used by GEANT for event tracking, is nevertheless very general and does not contain any assumption on the detector readout structure. It generally consists of hits positions and energy losses and provides the basis for the simulation of the detector response, which takes place at the digitization step.

| Parameter | B-Layer | Layers 1,2 | Disks |
|---|---------|------------|----------|
| pitch long direction (μm) | 300 | 400 | 400 |
| pitch short direction (μm) | 50 | 50 | 50 |
| Temperature ($^{\circ}\text{C}$) | -6 | -6 | not used |
| Bias Voltage (V) | 77 | 98 | not used |
| Lorentz angle ($^{\circ}$) | -15.6 | -15.6 | 0 |
| Cross talk (within columns) | 9% | 9% | 9% |
| Cross talk (within rows) | 1.5% | 1.5% | 1.5% |
| Pixel efficiency | 97% | 97% | 97% |
| Threshold (e^{-}) | 3000 | 3750 | 3750 |
| Threshold dispersion (e^{-}) | 200 | 200 | 200 |
| Noise (e^{-}) | 200 | 200 | 200 |

Table 8.1: Some of the default values for the parameters used in the pixel digitization (June 2001 software release).

The **digitization** simulates the readout. The segmentation of the detectors, the drift of the charge liberated in the active volumes and its collection on the electrodes are simulated in this phase. The output from the digitization is obtained in a form similar to that which might be expected from the readout electronics in the actual experiment.

In the Pixel detector, the charge associated with an hit located at a depth z in the silicon is transported to the surface of the sensor, where it is collected by the pixels, taking into account diffusion and the Lorentz effect. The diffusion is computed as $\sigma = \sigma_0 \sqrt{z/300 \mu\text{m}}$. The default value of σ_0 is $7 \mu\text{m}$. In the old versions of the code the Lorentz effect was simulated as a constant drift angle, with default value 15.6° in the barrel and 0° in the disks. In the most recent versions the results presented in chapter 6 have been taken into account and the Lorentz angle is computed from temperature, bias voltage and sensor thickness according to the parametrisations given in chapter 6. The bias voltage default values (table 8.1) are 77 V for the B-Layer and 98 V for Layers 1,2 and they are quite low (but not unrealistic, as the depletion voltage of unirradiated sensors should be of the order of 50 V). They have been chosen for reason of stability of the software, as they give a Lorentz angle equal to the previous default value of 15.6° for all barrel layers.

The segmentation of the sensor in pixels includes the ganged and long pixels on the chip border. The collection of the charge on the pixels simulates the

noise, the threshold and threshold dispersion, and the cross talk between pixels. The default values for these parameters are listed in table 8.1. An inefficiency of 3% is added (that is, the pixel hit is lost with 3% probability). This is the value indicated in the specifications and takes into account both sensor and electronics inefficiencies. The final front-end electronics is not yet ready. Hence the default values of the parameters related to the electronics (noise, cross talk, threshold dispersion, efficiency) are conservative estimates. The user can change the default values of all parameters.

Pile-up can be simulated by adding minimum bias events. The results presented in this chapter do not include simulation of pile-up. They are suited for low-luminosity operation. They also assume a uniform magnetic field in the Inner Detector. The use of a detailed magnetic field map has only minor effects [6], mainly on the track momentum resolution.

8.1.2 Reconstruction

The event reconstruction is performed by a program called ATRECON. It is mostly written in Fortran77, although some parts have already been rewritten in C++. It will be substituted in coming years by object-oriented software.

In a first phase, data from each subdetector is reconstructed in a stand-alone mode. Then the information from all subdetectors is combined. The complete reconstruction is seldom needed for any particular analysis. The various items are split into different packages that can be activated or not to save CPU time.

In the stand-alone reconstruction, matrices containing the energies in all calorimeter cells are filled. The position and energy of jets and electromagnetic clusters is found. The vector E_T^{miss} is computed. Muon tracks are reconstructed in the muon spectrometer.

Hit coordinates are reconstructed in the precision tracker and the TRT. The pixel cluster position is determined with a digital algorithm, and a (geometry version dependent) error is associated. The error is derived from pixel point resolution simulation studies. This is the part of the code that has been modified to implement analog reconstruction of position.

Three algorithms (iPatRec, PixlRec and xKalman) have been developed to reconstruct tracks in the Inner Detector [20]. They start the search for track candidates with different strategies, but as they all use pattern recognition in the silicon layers to resolve ambiguities, they have comparable performances. A C++ package for track reconstruction also exists and it can be used within ATRECON. It is called xKalman++ and it is the one used for the studies of this chapter. Nonlinear Kalman filtering techniques [58, 59, 60] are used to extrapolate tracks and remove wrong hits.

In a second phase, if requested, the informations from several detectors can be combined. Combined reconstruction includes matching Muon System and Inner Detector tracks, tagging photon conversions and K_s^0 decays by pairing Inner Detector tracks, discriminate electrons and photons using Inner Detector tracks, TRT hits, and electromagnetic calorimetry.

8.2 Pixel point resolution

The resolution on the position of the Pixel Detector hits (point resolution) was studied using events with a single high- p_T (200 GeV/ c) muon. The muon was generated with a flat distribution in pseudorapidity within an interval covering the full geometrical acceptance of the Pixel Detector, and with the standard vertex spread (15 μm in $x - y$, 5.6 cm in z). Only clusters not including the pixels on chip border (big and ganged pixels) have been considered for the study of resolution.

The geometry of the *Lund release* (June 2001) was used for the detector. Some of the parameters of the Lund pixel geometry are reported in table 8.2 (digitization default parameters are in table 8.1).

| Parameter | B-Layer | Layers 1,2 | Disks |
|------------------------------------|---------|-------------|--------------|
| Sensor thickness (μm) | 200 | 250 | 250 |
| Tilt angle barrel ($^\circ$) | -20 | -20 | - |
| Radius barrel (cm) | 5.05 | 8.85, 12.25 | - |
| Z position disks (cm) | | | 49.5, 58, 65 |

Table 8.2: Some of the parameters of the Lund geometry layout (June 2001).

The difference between analog and digital reconstruction of cluster position depends critically on the number of pixels in the cluster. Hence a discussion of the incidence angles and the resulting cluster sizes in the ATLAS Pixel detector will be made before presenting the spatial resolution obtained with the simulated data.

8.2.1 Angles of incidence and cluster sizes

The tilt angle of the barrel modules (table 8.2) is the angle between the radial direction and the normal to the module surface. It is 20° for all three layers in the Lund layout. High- p_t particles traversing a barrel module near its centre have an angle of incidence in the $R\phi$ plane which is equal to the module tilt angle. The short direction of the pixels lays in the $R\phi$ plane, hence in the pixel reference frame used in test beam data this angle corresponds to the incidence angle in the zx plane. The resolution studies with test beam data were made as a function of it. Modules are flat and a significant spread of incidence angles is introduced by the finite module size. The spread is maximum for the B-layer (of the order of 10°), because the module size is the same for all the layers and the B-layer is the nearest to the interaction point, hence it has the largest solid angle.

The sign of the tilt angle is equal to the Lorentz angle sign then the Lorentz effect partially compensate for the tilt. The default value of the difference between Lorentz angle and tilt angle is small (4.4°) so that limited charge sharing between pixels is expected. Increasing the bias voltage, the Lorentz angle decreases (fig. 6.13) increasing charge sharing. Two scenarios have been studied in detail: one with a bias voltage of 100 V and one with a bias voltage of 300 V. The same value was chosen for all the barrel layers. The corresponding values for the difference between the tilt angle and the Lorentz angle are listed in table 8.3.

| Bias voltage | Θ_L | Θ_T | $ \Theta_L - \Theta_T $ |
|------------------|------------|------------|-------------------------|
| B-Layer 77 V | -15.6 | -20 | 4.4 |
| Layers 1,2 98 V | -15.6 | -20 | 4.4 |
| B-Layer 100 V | -14.1 | -20 | 5.9 |
| Layers 1,2 100 V | -15.4 | -20 | 4.6 |
| B-Layer 300 V | -7.4 | -20 | 12.6 |
| Layers 1,2 300 V | -8.6 | -20 | 11.4 |

Table 8.3: Values of the Lorentz angle Θ_L (signed according to the ATLAS reference frame conventions) and of the difference between the Lorentz angle and the tilt angle Θ_T for the default bias voltage values and for bias voltages of 100 V and 300 V.

The angle of incidence in the zR plane depends on the pseudorapidity η^1 . The relation between η and the angle with the beam axis θ is given by eq. 1.1; the angle of incidence in the zR plane is

$$\alpha = \pi/2 - \theta = \pi/2 - 2 * \arctan[e^{-\eta}] \quad (8.1)$$

and it is 0 for $\eta = 0$ and 82° for $\eta = 2.7$.

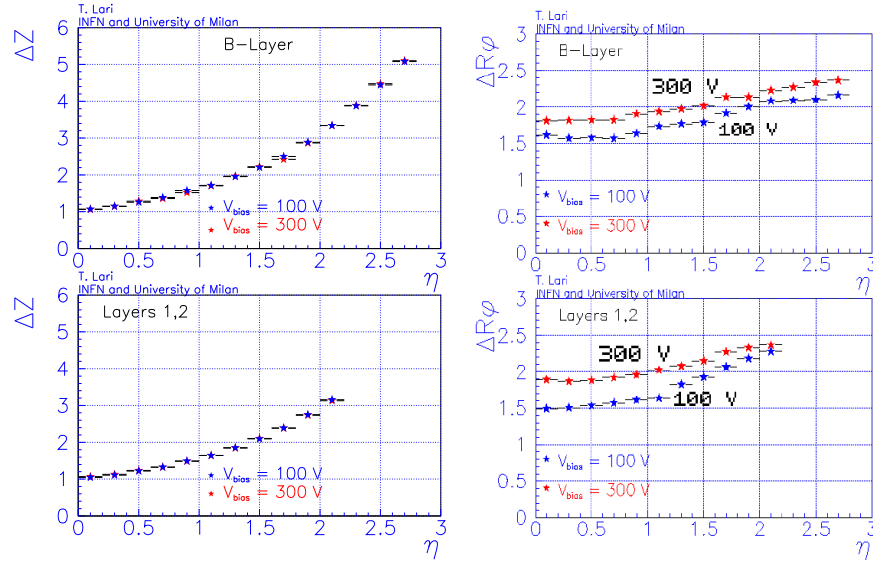


Figure 8.1: Mean cluster width in the z direction (left plots) and in the $R\phi$ direction (right plots) as a function of pseudorapidity. Pixels on chip borders are excluded.

The cluster width is a very important parameter for the spatial resolution. If the cluster width along a direction ($R\phi$ or z) is only one pixel, charge inter-

¹In this chapter pseudorapidity is indicated, as is standard, with the letter η . It should not be confused with the η variable defined in chapter 7

polution cannot be used and the only possible estimate for the cluster position is the centre of the pixel. The analog reconstruction offers an improvement over the digital algorithm only when at least two pixels are over threshold.

Fig. 8.1 shows the mean cluster widths in the barrel in the z and $R\phi$ direction as a function of pseudorapidity. The increase of the z cluster multiplicity with pseudorapidity, i.e. the angle of incidence in Rz plane, is easy to understand. An analog algorithm is expected to improve significantly the resolution for $\eta > 1.2$, when the mean cluster size is ≥ 2 columns. There is no dependence on the bias voltage, as Lorentz effects occur in the $R\phi$ direction. At $\eta = 0$ the $R\phi$ cluster width is about 1.5 at 100 V, which is good for digital resolution (section 7.5) but it is not enough for optimal analog resolution. Raising the voltage to 300 V, the cluster width approaches the ideal value of 2.

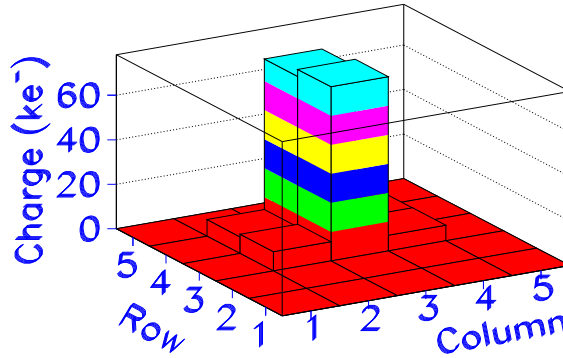


Figure 8.2: Collected charge of the pixels of a typical cluster at intermediate η .

The increase of cluster mean size with pseudorapidity is not obvious to understand, as the incidence angle in the $R\phi$ plane does not depend on η . Fig. 8.2 shows a typical cluster at intermediate η . The two pixels on the central row collect most of the charge. This is quite large (70 000 electrons per pixel) due to the large track pathlength under a pixel for tracks tilted in the long pitch direction. The pixels of adjacent rows also fire, but collect only about 9% of the charge of the central row pixels. This is the cross talk value (table 8.1). Hence the $R\phi$ multiplicity increases with η because as the charge on the pixels crossed by the track increases, the pixels of adjacent rows come over threshold due to crosstalk. This effect however does not improve analog resolution. If no charge sharing occurs because of Lorentz and diffusion effects, but only because of cross-talk, the charge of the external pixels is merely proportional to that of the central row pixels and it is not correlated to the particle position.

In the disks the incidence direction of the particles is nearly normal to the sensor surface (in both views), and the Lorentz angle is zero because the electric field in the sensors is parallel to the magnetic field. Therefore the single-pixel clusters are dominant (Fig. 8.3).

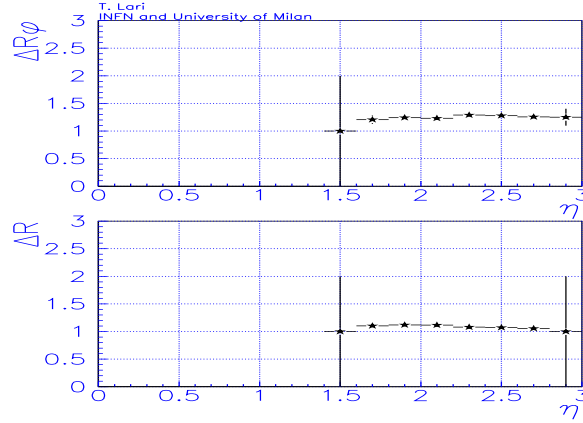


Figure 8.3: Mean cluster sizes for the disks, without pixels on chip borders, as a function of pseudorapidity.

8.2.2 Barrel $R\phi$ spatial resolution

Cluster position was reconstructed using a digital and an analog algorithm. The latter was used only for the barrel and it was simpler than the algorithm used for test beam studies. It is a center of gravity algorithm (each pixel position was weighted with its charge). It has been used to evaluate the potential for ATLAS physics performance of the analog reconstruction of pixel cluster position. The implementation of a more sophisticated reconstruction algorithm, similar to the one used for the test beam studies, will require the optimization of the amplitude Δ of the correction to digital position (section 7.4). This should be parametrized as a function of $R\phi$ and z cluster sizes, pseudorapidity, position in the module reference frame (because the angle of incidence depends on it) and bias voltage (because the Lorentz angle depends on it).

The $R\phi$ residuals between reconstructed and true hit positions in the barrel layers 1 and 2 are reported in Fig. 8.4 for a bias voltage of 100 V and Fig. 8.5 for a bias voltage of 300 V. The upper plot in each figure is for the digital algorithm and the lower one is for the analog one. The red histograms include all clusters (without pixels on chip borders) while the green ones include only the single-row clusters (that is, the clusters with width one in the $R\phi$ direction).

With a bias voltage of 100 V, there is a sizeable fraction of single-row clusters. Many of the multi-row clusters are due to crosstalk and not to genuine charge sharing. Consequently, only a limited advantage is provided by the center-of-gravity algorithm. The *r.m.s.* of the residual distribution is $9.4 \mu\text{m}$ with digital reconstruction and $8.4 \mu\text{m}$ with analog reconstruction. The widths of the gaussian fits show a similar difference.

If the bias voltage is raised to 300 V, the difference between mean incidence angle and Lorentz angle increases, and the single-row clusters reduce to a small fraction of the total. The digital residuals width is slightly worse while the analog residuals greatly improve. The *r.m.s.* of the residuals is now $10.9 \mu\text{m}$ with the digital reconstruction and $6.4 \mu\text{m}$ with the analog reconstruction. The

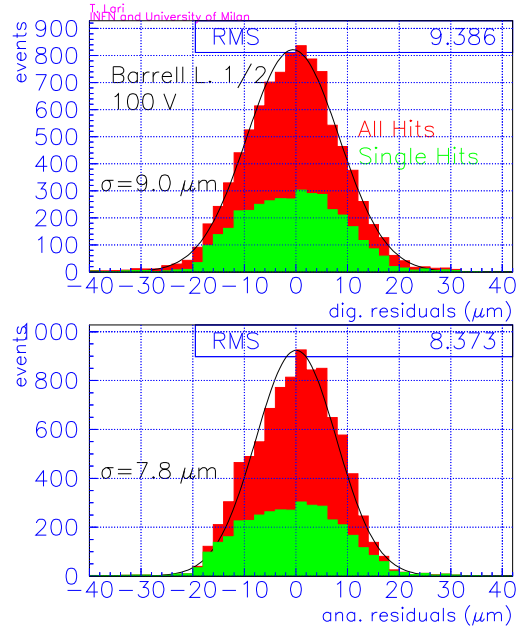


Figure 8.4: Residuals between true and reconstructed cluster position in pixel barrel layers 1 and 2, operated at 100 V bias voltage. The upper plot is for digital reconstructed position, the lower one for the analog one. Cluster with pixels on chip borders are excluded. The red histogram includes only single pixel clusters.

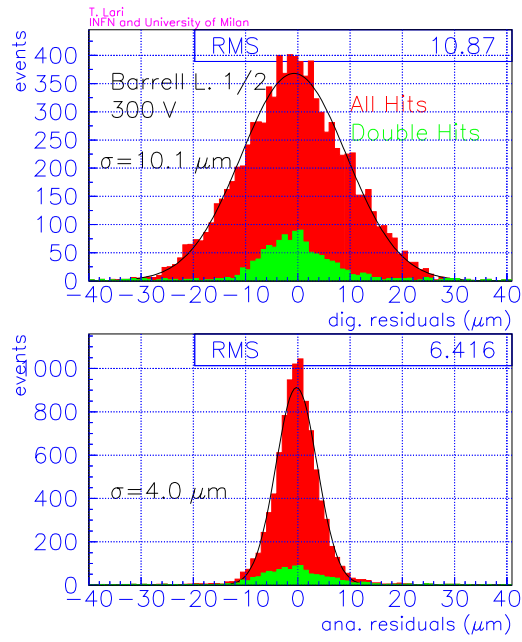


Figure 8.5: Residuals between true and reconstructed cluster position in pixel barrel layers 1 and 2, operated at 300 V bias voltage. The upper plot is for digital reconstructed position, the lower one for the analog one. Cluster with pixels on chip borders are excluded. The red histogram includes only single pixel clusters.

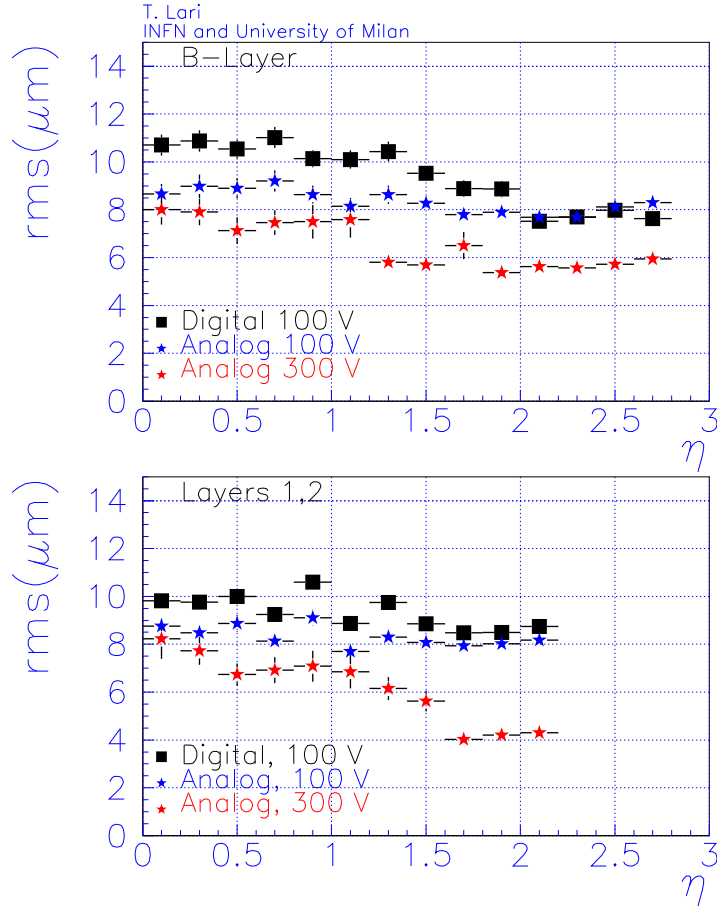


Figure 8.6: Point resolution of the barrel of the pixel detector in the $R\phi$ direction, as a function of pseudorapidity. Clusters with pixels on chip borders are excluded.

widths of the gaussian fits show an even larger difference between digital and analog reconstruction, being $10.1 \mu\text{m}$ with the former and $4.0 \mu\text{m}$ with the latter.

Fig. 8.6 reports the digital (at 100 V) and analog (at 100 V and 300 V) resolutions² as a function of pseudorapidity. The upper plot is for the B-Layer, the lower one for layers 1,2. The improvement from the use of analog reconstruction is seen at all pseudorapidities. The resolution is not a flat function of pseudorapidity, as it may be expected since the incidence angle and the Lorentz angle in the $R\phi$ plane do not change with pseudorapidity. A significant improvement is

²In the chapter 7 resolutions are expressed as the width of the gaussian fit, while in this chapter the *rms* of residual distributions are reported. These are slightly larger than the gaussian fit widths, but they are more representative for highly not-gaussian residual distributions, such as the z residuals.

observed for large values of η . This is related to the fact that when the angle of incidence in the long direction of the pixels is very large, the clusters extend over more than a column, and each column provides a separate measurement of the $R\phi$ coordinate.

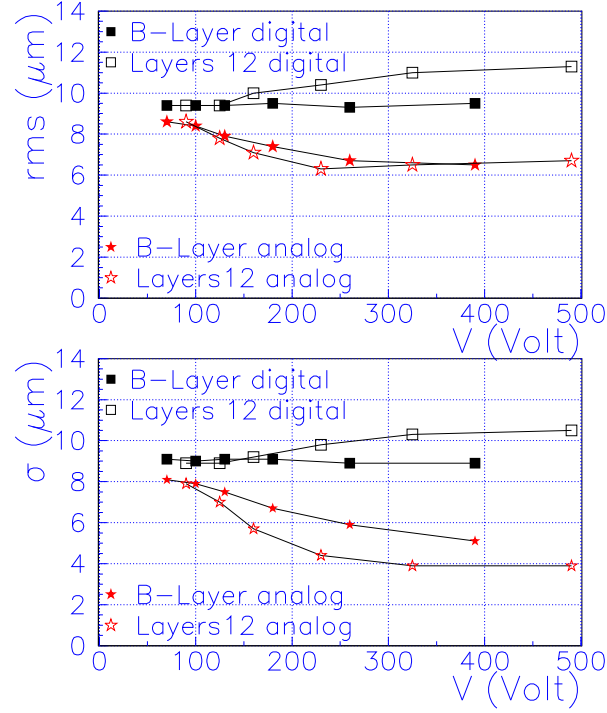


Figure 8.7: Point resolution of the barrel of the pixel detector in the $R\phi$ direction, averaged over a flat distribution of pseudorapidities, as a function of bias voltage. The upper plot reports the root mean square of residuals distributions, the lower one the width of the gaussian fits.

Finally, Fig. 8.7 shows the $R\phi$ resolution (averaged over a flat distribution of pseudorapidities) as function of bias voltage. The upper plot uses the root mean square of the residuals. The lower one uses the width of the gaussian fits. Most of the improvement in the resolution is already reached with a bias voltage of 200 V. The analog resolution is not much affected by a further increase in the bias voltage, both because the dependence of the Lorentz angle on the bias flattens (Fig. 6.13) and because the fraction of single-column clusters is already low at 200 V.

8.2.3 Barrel z resolution

Fig. 8.8 shows the pixel point resolution for the z direction as a function of η . As η is related to the angle of incidence in the zR plane (eq. 1.1) the z resolution

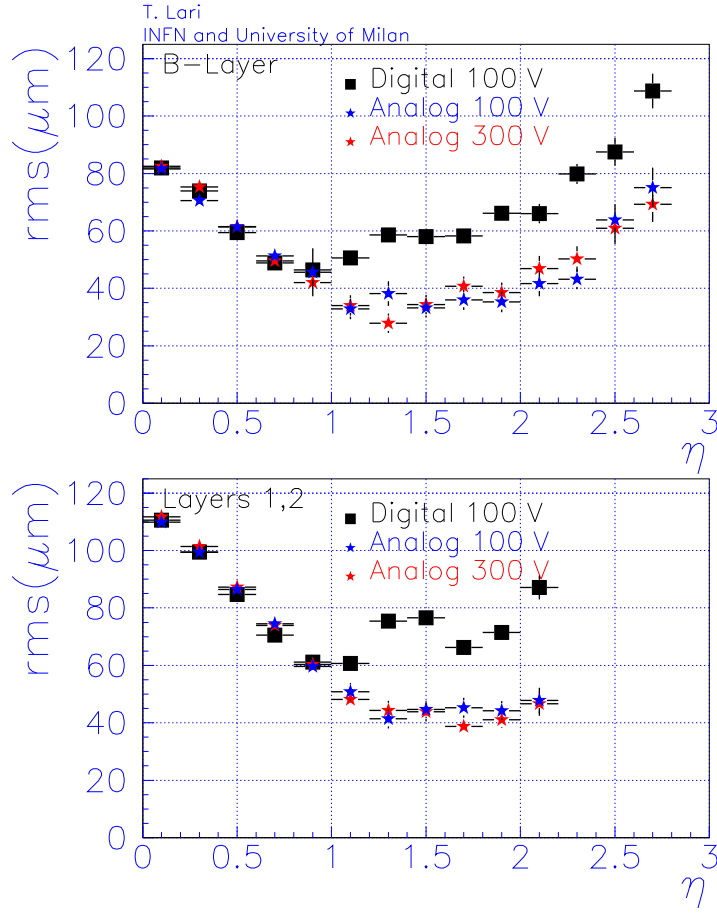


Figure 8.8: Point resolution of the barrel of the pixel detector in the z direction, as a function of pseudorapidity. Clusters with pixels on chip borders are excluded.

as a function of η has some features which are similar to the resolution as a function of the angle of incidence studied in the test beam (Fig. 7.3). There are also some differences because the test beam study was made for the other coordinate, along the short dimension of the pixel cell and because the other incidence angle was zero, resulting in one-dimensional clusters.

At normal incidence in the zR plane ($\eta = 0$) the fraction of two-column clusters is very small (Fig. 8.1). The resolution is determined by the distribution of residuals for single-column clusters, for which no charge interpolation is possible; hence there is no difference between analog and digital resolution. Single-column clusters have a flat residuals distribution extending between $-p/2$ and $p/2$, where p is the long dimension of the pixels. The *r.m.s.* of this distribution is $p/\sqrt{12}$ which is $115 \mu\text{m}$ for the outer layers and $87 \mu\text{m}$ for the B-Layer,

in agreement with the results of Fig. 8.8.

Increasing the pseudorapidity, the mean cluster size increases and the resolution improves. As discussed in section 7.5 the best digital resolution is achieved when the fraction of single-column clusters is equal to the fraction of two-column clusters; when this occurs, at $\eta \simeq 0.8$ (Fig. 8.1) the resolution is about $(p/2)/\sqrt{12}$, half of the $\eta = 0$ value. This is also observed in Fig. 8.8.

For $1 < |\eta| < 2$ the mean cluster width is about 2. Charge interpolation is now possible and the analog resolution reaches the best value. For the B-Layer digital and analog resolutions are about $60 \mu\text{m}$ and $35 \mu\text{m}$ respectively. For layers 1,2 they are $70 \mu\text{m}$ and $40 \mu\text{m}$ respectively.

At very large values of $|\eta|$, reached by the B-Layer, both resolutions get worse, but the analog reconstruction provides always a better position than the digital reconstruction. A value of pseudorapidity of 2.7 corresponds to an angle of incidence of 82° .

8.2.4 Disk resolution

The purpose of the study of this chapter is to evaluate the difference between analog and digital reconstruction and the dependence on the bias voltage of the ATLAS performances. In the disk little improvement in the spatial resolution is possible with the use of charge interpolation, because most of the hits are single-pixel clusters, and there is no dependence of the response on the bias voltage, because the magnetic and electric field are parallel and there is no Lorentz force acting on the charge carriers in the silicon.

Fig. 8.9 show the analog and digital resolution as a function of pseudorapidity for the disks. The disks are located between absolute pseudorapidities 1.5 and 3. The resolution is constant and it is $11 \mu\text{m}$ in the $R\phi$ direction and $100 \mu\text{m}$ in the radial direction³.

8.3 Tracking performance

The reconstruction routines which compute the coordinates and the errors on the coordinates of the pixel clusters in the barrel were modified to implement the analog center-of-gravity algorithm. The errors on cluster coordinates are read from values tabulated as a function of η and cluster $R\phi$ and z widths; the new values for the analog algorithm, found from the pixel point resolution study were inserted.

Tracks were reconstructed using the xKalman++ package. The same set of events used for the pixel point resolution study was used. The following quality selections on tracks were made:

³It can be observed that the resolution is in fact slightly worse with analog reconstruction. This occurs because the two-pixel clusters occur only when the track is located near the edge between two pixels. However when one of the two pixels collects much more charge than the other the centre of gravity algorithm reconstructs the track position near the centre of the pixel with the larger pulse height. Hence the very narrow two-pixel digital residual distribution is wider with the analog algorithm, while the single-pixel residuals (which give by far the greater contribution to the resolution) are the same. The test beam results at normal incidence show that a tuned analog algorithm can do better than the digital reconstruction, but the difference is only a few tenths of micron (table 7.3). In the following, the analog reconstruction is used only for the barrel hits, while the disk clusters position is always reconstructed with the digital algorithm.

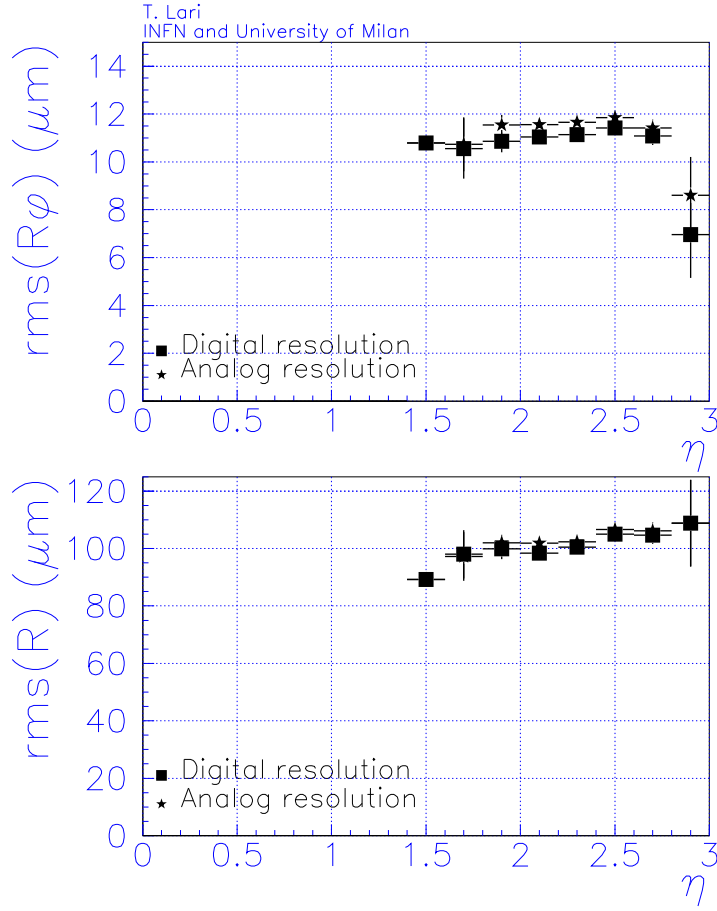


Figure 8.9: Point resolution of the disks of the pixel detector in the $R\phi$ direction (above) and in the radial direction (below) as a function of pseudorapidity and with digital and analog reconstruction. Clusters with pixels on chip borders are excluded.

- A minimum of 9 hits in the pixels + SCT (out of a maximum of 11, ignoring overlaps).
- A minimum of 2 pixel hits (out of a maximum of 3, ignoring overlaps).
- At least one associated hit in the B-layer.
- Transverse impact parameter less than 1 mm.

Fig. 8.10 shows the transverse impact parameter residuals distributions, for a flat distribution of pseudorapidities. The upper plot is obtained with digital reconstruction and a bias voltage of 100 V. The root mean square of the distribution is 11.0 μm and the width of the gaussian fit is 10.2 μm . The central

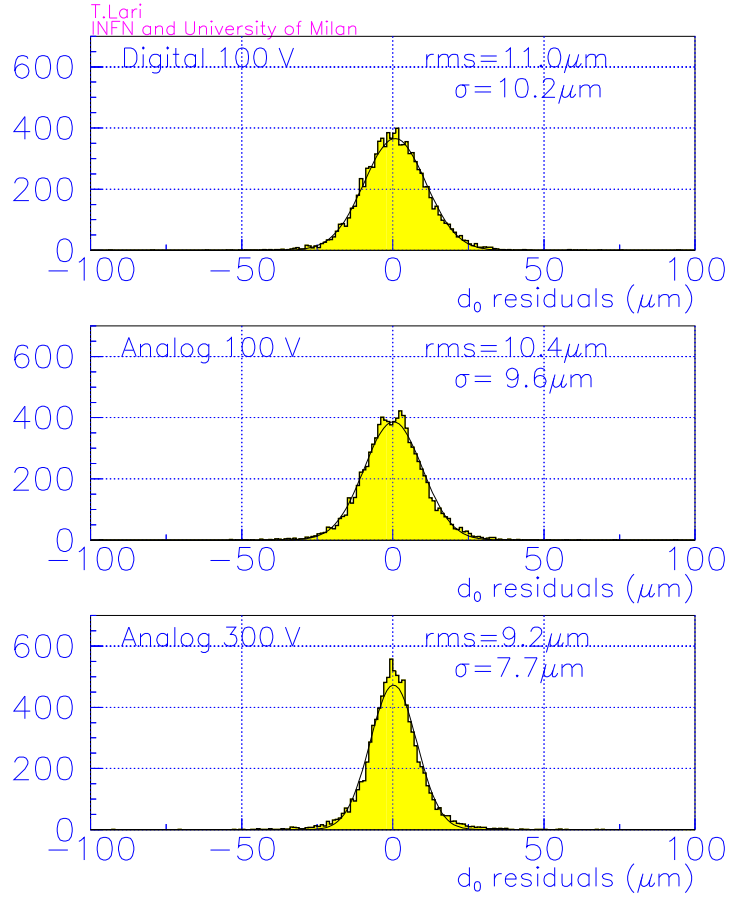


Figure 8.10: Transversal impact parameter residuals with digital reconstruction of pixel barrel clusters position and 100 V bias voltage (upper plot), with analog reconstruction and 100 V bias voltage (central plot), with analog reconstruction and 300 V bias voltage (lower plot).

plot shows the same with the analog reconstruction of the pixel barrel clusters position, and with the same bias voltage of 100 V. Both the *r.m.s.* and the width of the gaussian fit shows a 6% improvement over the impact parameter determination with digital reconstruction. The lower plot shows the transverse impact parameter residuals distribution with the analog reconstruction and a bias voltage of 300 V. An additional improvement of the 12% in the *r.m.s.* and of the 20% in the width of the gaussian fit is observed with the change in the bias voltage.

Fig. 8.11 shows the *r.m.s.* of the transverse impact parameter residuals distributions as a function of pseudorapidity. The resolution is almost constant up to $|\eta| = 2$. Little difference is found between analog and digital reconstruction

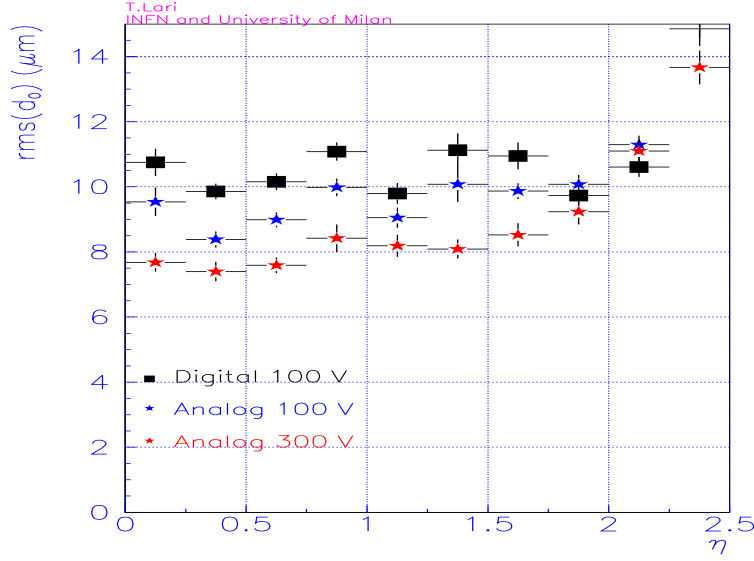


Figure 8.11: Transversal impact parameter resolution as a function of pseudorapidity.

for $|\eta| > 1.7$ because the analog reconstruction is used only for the barrel part of the pixel detector and at large η a significant contribution to the determination of the impact parameter comes from the disks (see Fig. 2.6 for a plot of the number of barrel and disk hits as a function of pseudorapidity). For $|\eta| < 1.7$ the difference between the analog and the digital reconstruction and between 100 V and 300 V is almost flat in pseudorapidity. Resolution is about $10.5 \mu\text{m}$ with digital reconstruction and 100 V bias voltage, $9.5 \mu\text{m}$ with analog reconstruction and 100 V bias voltage, $8.0 \mu\text{m}$ with analog reconstruction and 300 V bias voltage.

Fig. 8.12 shows the longitudinal impact parameter resolution as a function of η . Some improvement, which slightly increases with bias voltage, is observed for $1 < |\eta| < 2$. For lower value of pseudorapidity the impact parameter resolution does not depend on the reconstruction strategy because the pixel point resolution is determined by the single-column clusters residuals which does not benefit from charge interpolation. For $|\eta| > 2$ the resolution receives an important contribution from the disks which also do not benefit from the use of analog reconstruction, and again there is little difference between the three sets of results.

The efficiency of a reconstruction routine is an important issue. There is little value in a reconstruction which improves resolution, if it has also a much poorer efficiency. A low tracking efficiency affects most physics analyses. Fig. 8.13 shows the track efficiency as a function of pseudorapidity. It does not depend either on the reconstruction strategy or on the bias voltage value. There are other three track parameters: the reconstructed momentum, the azimuthal angle and the pseudorapidity. The contribution of the pixel detector resolution to the

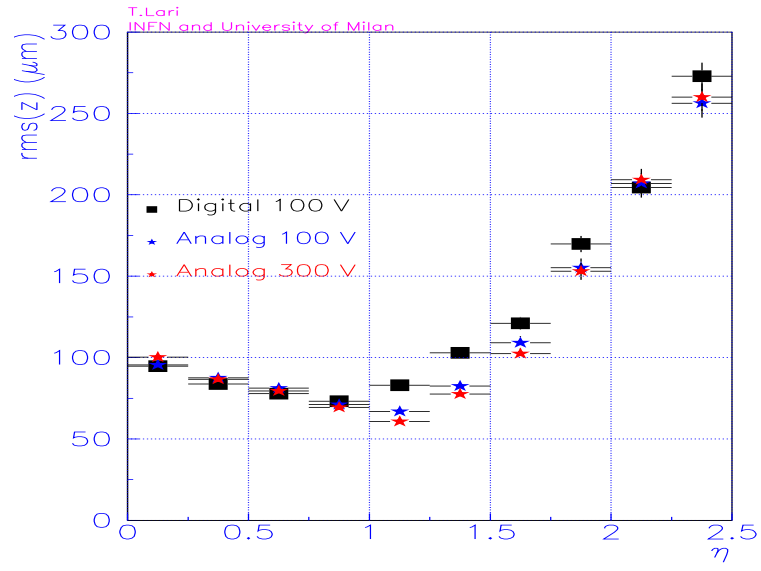


Figure 8.12: Longitudinal impact parameter resolution as a function of pseudorapidity.

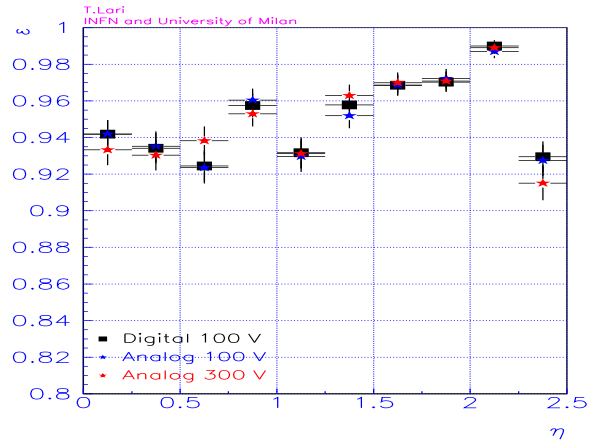


Figure 8.13: Tracking efficiency as a function of pseudorapidity.

determination of these parameters is less important, and no sensible dependence on the pixel cluster reconstruction algorithm or on the bias voltage has been found.

8.4 b -tagging performance

The discrimination of beauty jets against those originating from lighter flavor quark is an essential tool for accomplishing many of ATLAS physics goals. As an example, the detection a Standard Model Higgs boson of the mass suggested by LEP searches and the detection of the lightest SUSY Higgs boson over most of the MSSM parameter space (section 1.2) rely on a good flavor tagging performance.

The most powerful b -tagging method is based on the fact that for jets originating from lighter quarks most of the particles reconstructed by the Inner Detector derive from the decay of very short-lived objects and hence appear to originate from the primary vertex. In jets produced by b -quark some particles come from the decay of B hadrons, which have a lifetime of the order of 1 ps. This gives rise to tracks with a significant impact parameter. As the b -tagging relies on a good impact parameter measurement, it is sensible to the pixel performance. Then b -tagging was used to evaluate the impact of the use of pixel charge information on ATLAS physics performance.

8.4.1 Jets used for b -tagging studies

The study of u -jets rejection against b -jets was performed using a sample of 2500 $H \rightarrow b\bar{b}$ and 10 000 $H \rightarrow u\bar{u}$ decays. The Higgs had a mass of 400 GeV and was produced in association with a $W \rightarrow \mu\nu$ or a $Z \rightarrow \mu^+\mu^-$. The PYTHIA generator [61] was used. Such events are not a realistic channel to search for an Higgs boson of this mass; however they are usually used as a factory of b -jets and u -jets for evaluating the b -tagging performance over a broad jet kinematic range. b -tagging performance using jets from lighter Higgs decays or from top decays has been proven to be similar or better [6].

| Parameter | B-Layer | Layer 1 | Layer 2 | Disks |
|------------------------------------|---------|---------|---------|--------------|
| Sensor thickness (μm) | 200 | 250 | 250 | 250 |
| Tilt angle barrel ($^\circ$) | -21 | -17.5 | -19 | - |
| Radius barrel (cm) | 5.05 | 8.75 | 12.25 | - |
| Z position disks (cm) | | | | 49.5, 58, 65 |

Table 8.4: Some of the parameters of the old insertable geometry layout (December 2000).

Only the Inner Detector has been simulated, as the simulation of the calorimeter requires a much larger CPU time. The pixels are described according to the December 2000 layout (*old insertable* layout). The parameters of this layout are reported in table 8.4. The other components of the Inner Detector are described by an older layout, the same used for the Physics TDR studies [6].

The impact parameter resolutions with this geometry description are similar to those obtained for the Lund layout and described in the previous section. The simulation of an high statistic data sample for b -tagging studies with the Lund layout is under way.

The b -tagging performance without charge interpolation in the pixels has been studied for the default value of Lorentz angle (table 8.1), while the performance using charge interpolation has been studied for the default Lorentz angle and for a Lorentz angle equal to 8 degrees. Such an angle is expected in the

B-Layer for a bias voltage of 270 V and in layers 1,2 for a bias of 340 V. We will refer to the results obtained with the default value of the Lorentz angle as low-voltage results, and to the results obtained with a Lorentz angle of 8° as high-voltage results.

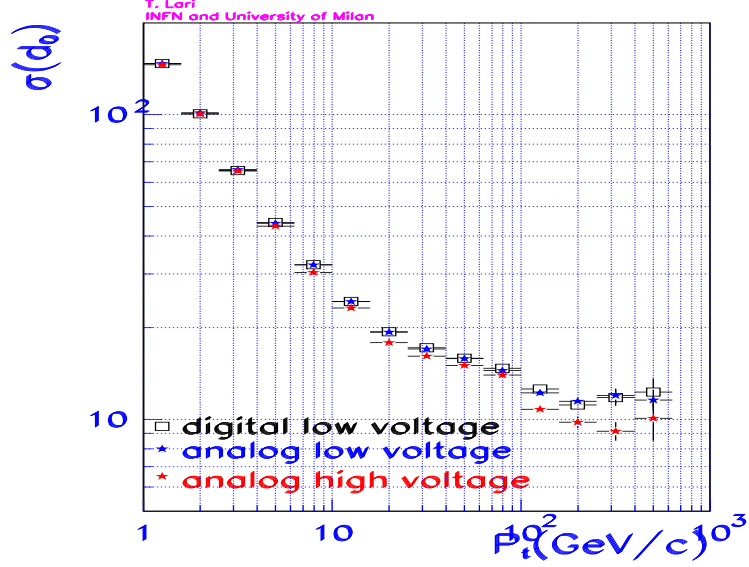


Figure 8.14: Transversal impact parameter resolution as a function of transverse momentum, for the tracks of $H \rightarrow u\bar{u}$ events which come from the primary vertex.

Fig. 8.14 shows the resolution on the transverse impact parameter for the tracks of the $H \rightarrow u\bar{u}$ events which come from the primary vertex. The resolution is the *r.m.s.* of the residual distribution and it has been plotted as a function of the transverse momentum of tracks. The standard quality cuts described in the previous section have been applied. For high transverse momentum tracks the resolution is about $12 \mu\text{m}$ with the default value of the Lorentz angle and $10 \mu\text{m}$ with analog pixel cluster reconstruction and at high-voltage. These resolutions were worse than those obtained for $p_t = 200 \text{ GeV}/c$ muons, because

- Muon tracks are easier to reconstruct than those of other particles. Electrons present a particularly difficult task for the tracking algorithms, as they lose a significant fraction of their energy through bremsstrahlung and consequently change their transverse momentum and radius of curvature. Hadrons may suffer elastic hadronic scattering.
- Near the jet axis there is a high density of tracks, which give rise to ambiguities and to merged hits. A few tracks badly tracked (but not so badly reconstructed to be rejected by the track quality cuts) can give a significant contribution to the *r.m.s.* of distributions.

- The pseudorapidity of the charged particles coming from the decay of the Higgs is not flat. Fig. 8.15 shows the pseudorapidity distribution for the particles coming from the decay of a 400 GeV Higgs and those in minimum bias events. The minimum bias distribution is almost flat in the range of $|\eta|$ covered by the pixel detector, while the distribution of particles in the Higgs decay is peaked at low values of $|\eta|$.

The resolution on the transverse impact parameter of tracks is far worse at low p_t where it is dominated by multiple scattering rather than by the intrinsic resolution of pixels. Consequently, little difference is found at low p_T between analog and digital reconstruction strategies or between low-voltage or high-voltage operation. Unfortunately the distribution of transverse momentum of the tracks in the jets is peaked at low p_T (Fig. 8.16). This limits the expected advantage from the use of charge interpolation in the pixels. The degradation of the impact parameter resolution at low p_T is less severe in the zR view (Fig. 8.17).

As calorimeter information is not available, the jets were defined using MonteCarlo truth information. The quarks coming from the Higgs decay which after final state radiation have $|\eta| < 2.5$ and $p_t > 10$ GeV/c are selected. The tracks within the cone $|\Delta\phi \times \Delta\eta| < 0.4$ centered on the quark direction are used to tag the jet flavor.

The effect of selecting jets using MonteCarlo truth information instead of the calorimeters information was evaluated by performing the analysis of simulated data produced for the Physics TDR studies [6]. These data have the entire detector simulated with an old (1998) geometry layout⁴. A sample of 14 000 $H \rightarrow u\bar{u}$ and 8 000 $H \rightarrow b\bar{b}$ has been used. Table 8.5 shows that the use of MonteCarlo truth information increases the background rejection at fixed tagged efficiency by a small amount.

| $\epsilon_b(\%)$ | 50 | 60 |
|-----------------------|--------------|-------------|
| Jets from calorimeter | 208 ± 23 | 87 ± 6 |
| Jets from MC truth | 255 ± 29 | 111 ± 8 |

Table 8.5: Effect of using MC truth information instead of calorimeter data on the b -tagging performance. The values of u -jets rejections for a b -jet efficiency of 50% and 60% are reported. The comparison is made using data simulated with the 1998 geometry.

The aim of the b -tagging study was to study the *relative* performances of the tracking algorithms at different bias voltages, hence the use of MonteCarlo rather than calorimeter information was considered acceptable.

8.4.2 b -tagging methodology

The discrimination of b -jets against u -jets is made using the impact parameter of tracks which pass a number of quality cuts:

- the standard quality cuts described in the previous section;

⁴This layout cannot be used for a reliable comparison between analog and digital pixel clusters reconstruction, as the thickness of the silicon sensors and the tilt angle are quite different from those of the last designs, resulting in very different charge collection properties.

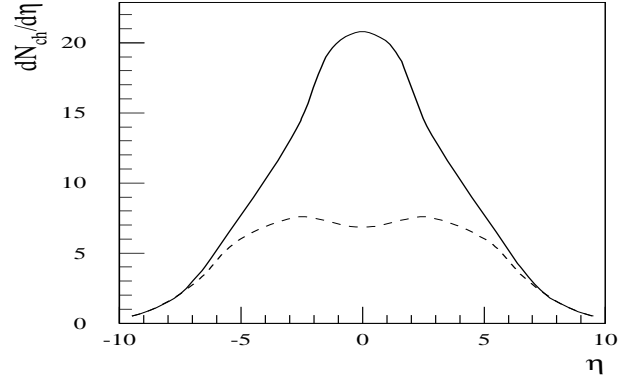


Figure 8.15: Pseudorapidity distribution of charged particles (no p_T cut). The solid line corresponds to all particles in events containing the decay of a 400 GeV Higgs to b -jets, the dashed line to all particles in minimum bias events

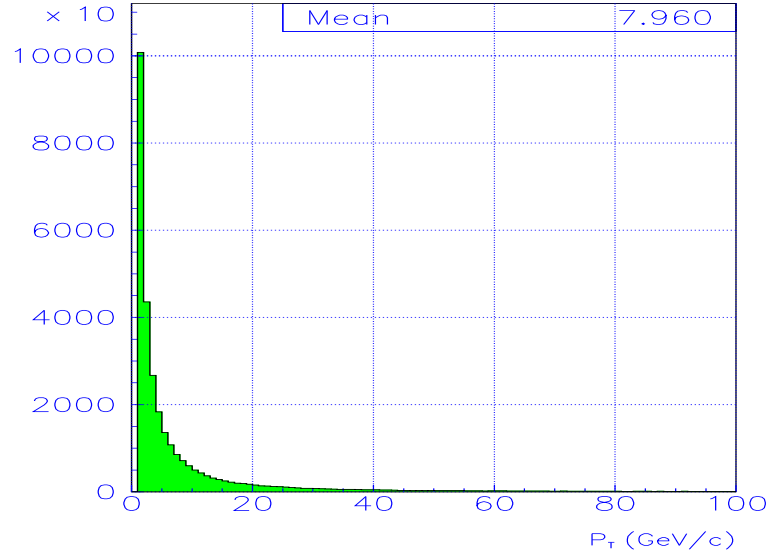


Figure 8.16: Transverse momentum distribution for the tracks of $H \rightarrow u\bar{u}$ events.

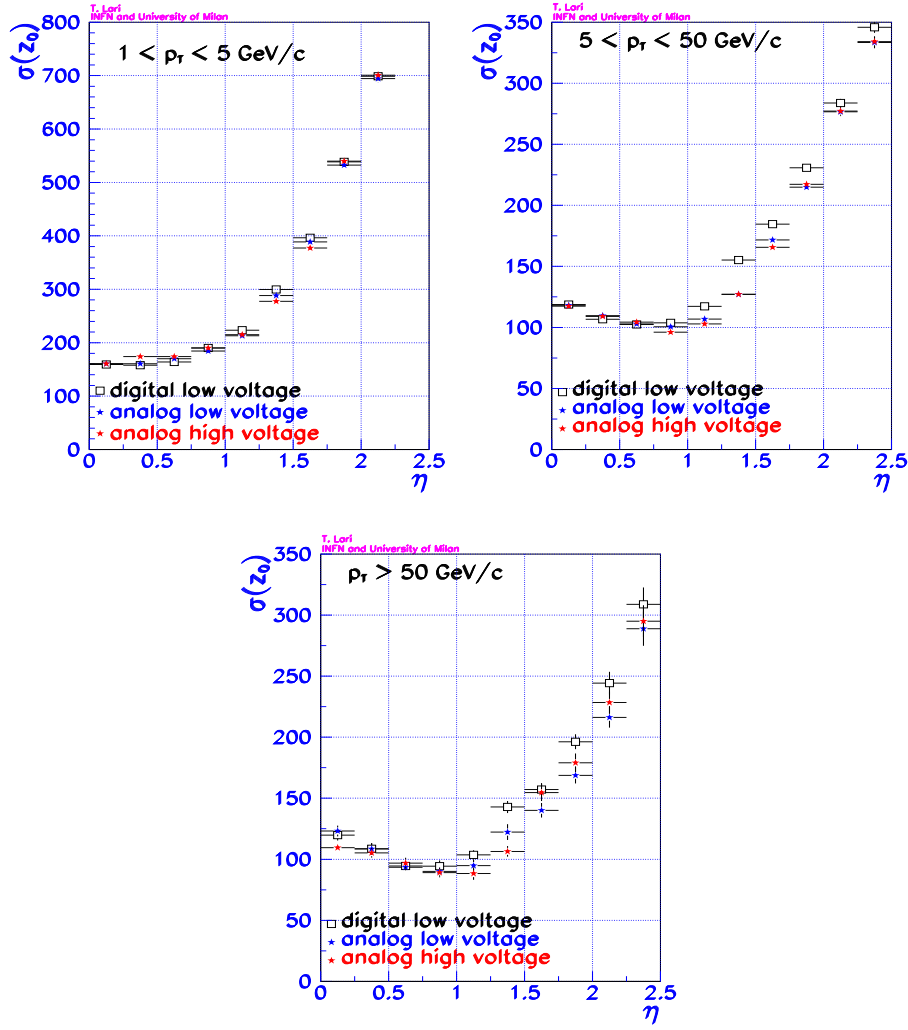


Figure 8.17: Longitudinal impact parameter resolution as a function of pseudo-rapidity for the tracks of $H \rightarrow u\bar{u}$ events which come from the primary vertex. The three plots correspond to different bins of transverse momentum.

- impact parameter in the Rz plane relative to the reconstructed primary interaction point $< 1.5/\sin(\theta)$ mm;
- track fit $\chi^2/n.o.f. < 3$;
- at least seven hits in the precision layer not shared with any other track

The cuts which are made in addition to the standard quality cuts are intended to remove secondary tracks, *i.e.* tracks originating from interactions of primary tracks with the detector material. These are the main limitation to the b -tagging performance.

The second cut requires the reconstruction of the z coordinate of the primary interaction vertex. This is made taking the weighted average of the longitudinal impact parameters of all well-reconstructed tracks in the event which have a transverse impact parameter $d_0 < 2\sigma(d_0)$ (to exclude tracks from decays of long-lived particles). The resolution achieved with this method is shown in Fig. 8.18. It can be seen that the analog algorithm allows a 10% improvement in resolution at low bias voltages. A bias voltage of order 300 V allows a further 3% gain.

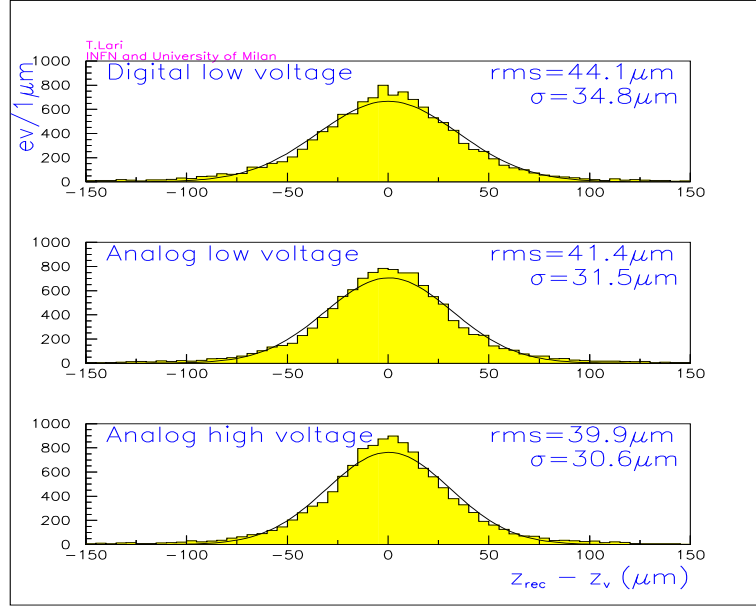


Figure 8.18: z-vertex resolution

The $R\phi$ coordinate of jets is not reconstructed. The transverse impact parameter has been computed with respect to the nominal beam position ($x = 0, y = 0$ in this simulation) which is anticipated to be measured with high accuracy as a function of time. Therefore the uncertainty on the impact parameter is given by the measurement error and the spread of the beam spot ($15 \mu\text{m}$) taken in quadrature. The effect of this is small since the spread of the beam spot is small compared to the resolution on the impact parameter of most tracks (Fig. 8.14). The results obtained will be conservative, an explicit reconstruction of the primary vertex may allow to put in evidence a greater difference between the two reconstruction strategies because the use of analog pixel position should allow a better reconstruction of the primary vertex also in the transverse plane.

A last cut is introduced to remove electrons from photon conversions. Tracks were rejected if they had at least 5% high-threshold hits in the TRT (or no TRT hits at all, which happens in case of hard bremsstrahlung) and formed a good conversion candidate with an other track in the same jet.

Fig. 8.19 shows the distribution of the significance S (impact parameter divided by its error) for b -jets and u -jets in the transverse plane. The significance is positive if the track crosses the jet axis in front of the primary vertex, it is

negative if it appears to originate from behind the primary vertex. Both distributions have significant cores which represent correctly reconstructed tracks coming from the primary vertex. These cores can be described by gaussians of width close to one. The b -jets have tracks with large positive significance, corresponding to a genuine lifetime content. By contrast u -jets have only a small excess of tracks which appear to contain lifetime content; they are due either to the decay of neutral strange particles or to interactions with material. There are also tails on the negative side of the significance distribution. For the b -jets, these come mainly from an incorrect determination of the sign or to the decay of charmed states. For the u -jets, the tail is dominated by secondaries from interactions.

Fig. 8.20 shows the same plot for the longitudinal impact parameter. The sign is the sign of the impact parameter (z position of the track at the point of closest approach) which has no reason to be positive rather than negative, so the distributions are symmetric.

The method used to decide if a jet is more b -like or u -like is the likelihood ratio method:

1. For each selected track i in a jet, the significance S_i was calculated.
2. The ratio of the values of the significance probability distribution functions for b -jets and u -jets was computed: $r_i = f_b(S_i)/f_u(S_i)$.
3. A jet weight was constructed from the sum of the logarithms of the ratios: $W = \sum \log r_i$.
4. By keeping jets above some value of W (a value which can be varied), the efficiency for different jet samples can be obtained.

By varying the cut on the jet weights (Fig. 8.21) it is possible to draw a curve of u -jet rejection (the reciprocal of efficiency) against b -jet efficiency. By using the significance distribution $f_u(S_i)$ for u -jets, the method was optimized for the rejection of u -jets. In the case of real data, since the jet type will not be *a priori* known, the rejection will have to be optimized for each specific background under study.

8.4.3 Results

The curves of rejection against efficiency for the different algorithms and bias voltages used in the simulation are shown in Fig. 8.22 for the b -tagging in the transverse plane, and in Fig. 8.23 for the less powerful b -tagging in the Zr plane. The u -jet rejection for b -tagging efficiencies of 0.5 and 0.6 (values which are suitable for an Higgs search in the $b\bar{b}$ channel [6]) are reported also in table 8.6.

No statistically significant improvement⁵ in the transversal b -tagging is seen from the use of the charge interpolation algorithm. However statistical errors are quite large; at 90% confidence level an improvement of up to 40% is possible for the analog b -tagging at high bias voltage over the digital b -tagging at low

⁵The numbers of u -jets surviving b -tagging cuts in the three scenarios are expected to be correlated, as the data are the same. A correlation analysis may increase the statistical significance of the difference found between the analog performance at high bias voltages and the other two scenarios, which is slightly more than a standard deviation assuming no correlation.

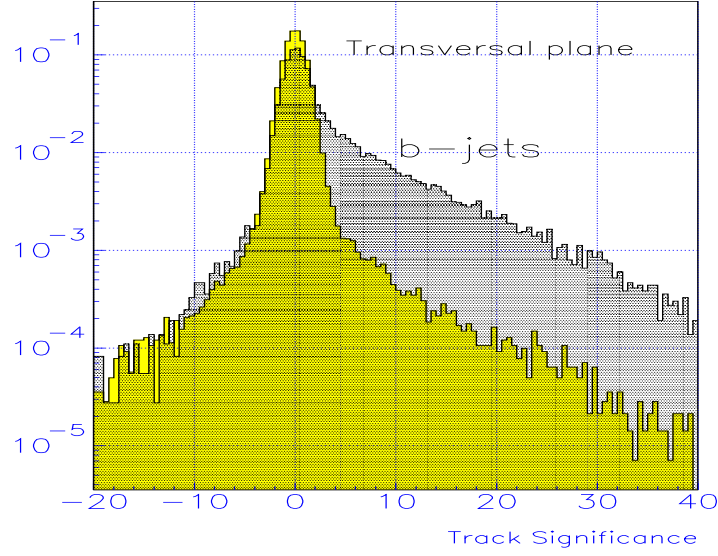


Figure 8.19: Significance distribution: signed transverse impact parameter divided by its error (digital algorithm). Histograms for u -jets (yellow) and b -jets (dotted) are normalized to the same area.

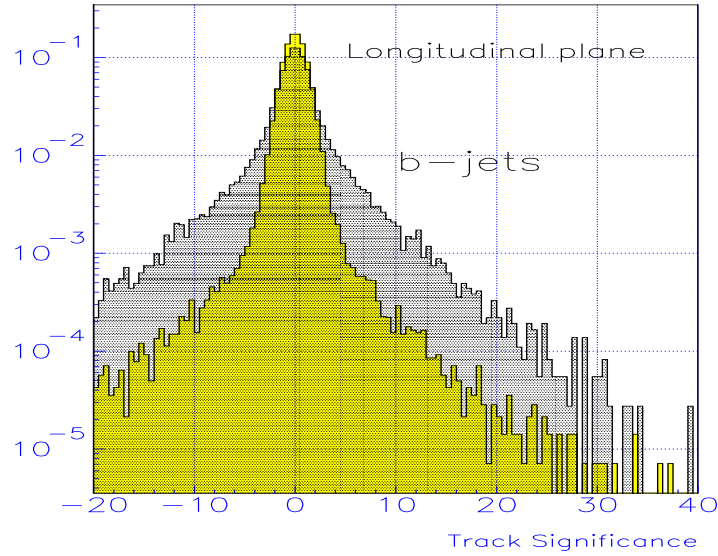


Figure 8.20: Significance distribution: longitudinal impact parameter divided by its error (digital algorithm). Histograms for u -jets (yellow) and b -jets (dotted) are normalized to the same area.

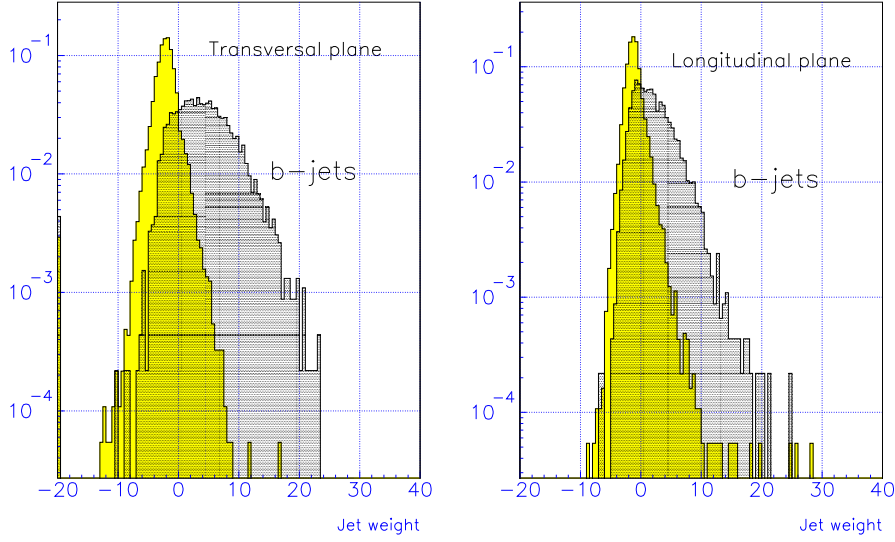


Figure 8.21: Weights from likelihood ratio for u -jets (yellow) and b -jets (dotted), in the transversal plane (left plot) and in the longitudinal one (right plot). The plots are for the digital algorithm.

| | | | |
|---|----------------|----------------|----------------|
| pixel cluster position | digital | analog | analog |
| pixel B-Layer bias voltage | 77 V | 77 V | 270 V |
| pixel layers 1,2 bias voltage | 98 V | 98 V | 340 V |
| R_u ($R\phi$ plane, $\epsilon_b = 0.5$) | 147 ± 13 | 142 ± 13 | 173 ± 17 |
| R_u ($R\phi$ plane, $\epsilon_b = 0.6$) | 67 ± 4 | 62 ± 4 | 76 ± 5 |
| R_u (zR plane, $\epsilon_b = 0.5$) | 20.6 ± 0.7 | 22.1 ± 0.8 | 25.8 ± 1.0 |
| R_u (zR plane, $\epsilon_b = 0.6$) | 11.0 ± 0.3 | 12.4 ± 0.3 | 13.5 ± 0.4 |

Table 8.6: u -jet rejection values R_u reported for two selected b -tagging efficiencies (0.5 and 0.6).

bias voltage. More simulated data for b -tagging are being generated with the Lund layout, and they will allow to reduce the statistical errors.

In the Zr view the rejections are smaller, due to the poorer precision on the longitudinal impact parameter. This means that the vertex b -tagging in this view gives a smaller contribution to the overall discrimination power of the detector. It also means that the statistical errors are smaller. A significant improvement, which increases with bias voltage, is seen with the use of charge interpolation.

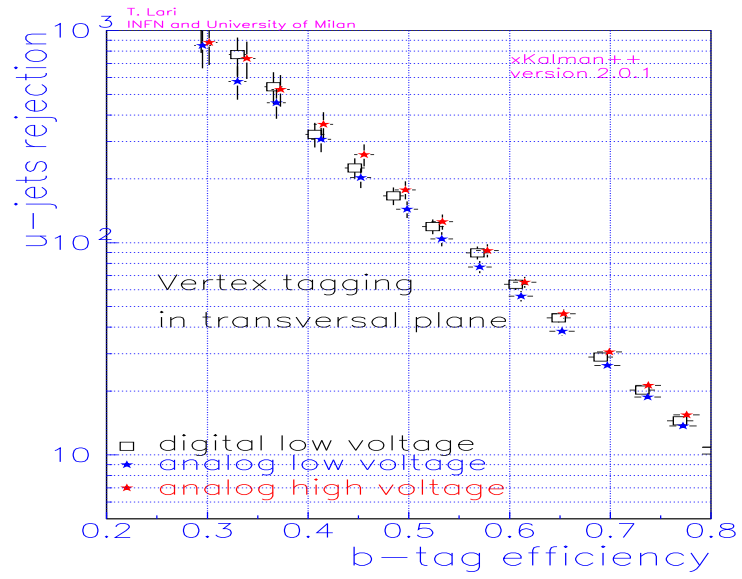


Figure 8.22: u -jet rejection against b -jet efficiency in the transversal plane.

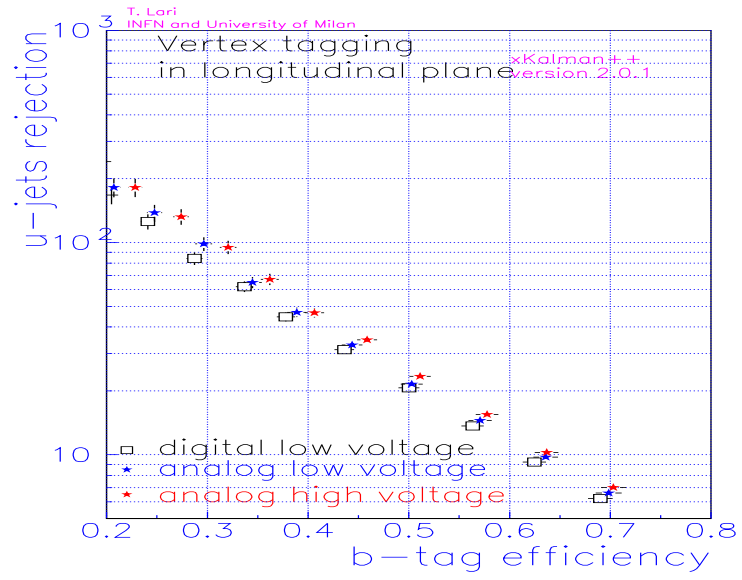


Figure 8.23: u -jet rejection against b -jet efficiency in the longitudinal plane.

Conclusions

Test beam data have been used to characterize silicon pixel sensors developed to meet ATLAS Pixel detector specifications. The tested devices implemented different designs options; some were irradiated to the radiation fluences expected at the LHC.

The charge collection efficiency as a function of the impact point of incident particles on the sensor surface, the spatial resolution as a function of incidence angle and the detection efficiency were measured. Spatial resolution was studied using different algorithms to reconstruct pixel clusters position. An optimal algorithm which makes use of charge interpolation was developed. ATLAS specifications are a 97% detection efficiency for high energy particles in a time window of 25 ns, and a spatial resolution better than $15\text{ }\mu\text{m}$ in the short pixel direction. These performances must be obtained also after irradiation. The measurement of charge collection efficiency is important to optimize the sensor design, as a poor charge collection results in a bad detection efficiency and spatial resolution.

Sensor designs, based on *p-spray* and *p-stop* isolation techniques respectively, were tested in 1998. The *p-stop* sensors were found to have good performances before irradiation, but they produced too an high noise after being exposed to high radiation fluences, so they were not suited for ATLAS operating conditions. The *p-spray* sensors were radiation-hard but the baseline design showed a significant suppression of charge collection efficiency at the border between pixels. This resulted in a too low detection efficiency, and in a spatial resolution slightly worse than the *p-stop* one. The design of the *p-spray* sensor was consequently modified. The new sensors were tested in 1999-2001 showing performances similar to those of the *p-stops* before irradiation, with a spatial resolution between $6\text{ }\mu\text{m}$ and $13\text{ }\mu\text{m}$ and an efficiency in excess of 99%. After irradiation they had a spatial resolution between $7\text{ }\mu\text{m}$ and $13\text{ }\mu\text{m}$, depending on the incidence angle. The detection efficiency after irradiation, could not be measured, due to readout electronics problems. An efficiency in excess of 98% was measured after irradiation for the old *p-spray* sensors excluding the region with charge collection inefficiencies; a similar performance is expected for the new sensors in the 2002 test beam, when the final electronics will be available.

After irradiation the active depth of the sensors (*depletion depth*) may be smaller than the full thickness even at the maximum operating voltage of 600 V. A method to measure the depletion depth from test-beam data was developed. A value of about $200\text{ }\mu\text{m}$, out of a full thickness of $280\text{ }\mu\text{m}$, was found for standard substrate sensors irradiated to $10^{15}\text{ n}_{\text{eq}}\text{cm}^{-2}$ fluence and operated at 600 V. $250\text{ }\mu\text{m}$ thick oxygen-enriched sensors, exposed to the same fluence, were found to be completely depleted for bias voltages larger than 400 V confirming

the superior radiation hardness of oxygen-enriched silicon.

In ATLAS the pixel detector will operate in a magnetic field of 2 T. This will alter the charge collection properties. The electron drift in silicon will occur along a direction which forms an angle $\Theta_L \neq 0$ with the normal to the sensor surface, due to the Lorentz force $e\vec{E} \times \vec{B}$. The Lorentz angle Θ_L was measured and found to be a function of the operating voltage. This was explained as due to the dependence of electron mobility in silicon on the electric field. From silicon electric properties, the Lorentz angle is expected to vary in ATLAS conditions from about 15° at 100 V voltage to 5° at 600 V. This will make ATLAS Pixel performance voltage-dependent.

To evaluate the effect of pixel operating voltage and different pixel cluster position reconstruction strategies on the ATLAS performance, a study with ATLAS GEANT3 simulation was made. Two position reconstruction strategies were examined: one which uses only the position of the pixels which give a signal (digital algorithm) and one which makes use also of the information on the charge collected by each pixel (analog algorithm).

The resolution on the impact parameter in the $R\phi$ plane of muons with 200 GeV/c transverse momentum was found to be $11.0 \mu\text{m}$ with digital reconstruction, $10.4 \mu\text{m}$ with analog reconstruction and 100 V pixel voltage, $9.2 \mu\text{m}$ with analog reconstruction and 300 V voltage.

The resolution on the longitudinal position of the primary interaction vertex for all particles in jets with a track mean transverse momentum of 8 GeV/c was found to be $44.1 \mu\text{m}$ with digital reconstruction, $41.4 \mu\text{m}$ with analog reconstruction and 100 V pixel voltage, $39.9 \mu\text{m}$ with analog reconstruction and 300 V voltage.

The discrimination of b -quark jets against u -quark jets improves with analog reconstruction by 10% and 20% at low voltage and high voltage respectively, when the longitudinal impact parameter of tracks is used to tag the jet flavor. No difference is observed using the transverse impact parameter. However differences of order 20% are possible within the statistical uncertainties. Larger statistics samples of simulated data will be available in the near future to reduce such uncertainties.

Bibliography

- [1] I. Gorelov et al., *A measurement of Lorentz angle and spatial resolution of radiation hard silicon pixel sensors*, CERN-EP/2001-032, to be published in Nucl. Instr. and Meth. A.
- [2] T. Lari, *Alignment of irradiated and not irradiated pixel sensors in test-beam operation*, ATL-INDET-2001-002.
- [3] T. Lari, *Lorentz angle variation with electric field for ATLAS silicon detectors*, ATL-INDET-2001-004.
- [4] T. Lari, Nucl. Instr. and Meth. **A465** (2001) 112.
- [5] *LHC white book*, CERN/AC/93-03; *LHC conceptual design report*, CERN/AC/95-05.
- [6] The ATLAS Collaboration, *ATLAS detector and physics performance Technical Design Report*, CERN/LHCC 99-14.
- [7] D. E. Groom et al., Eur. Phys. Journal **C15** (2000) 1.
- [8] T. Hambye and K. Riesselmann, Phys. Rev. **D55** (1997) 7255.
- [9] C. Quigg, B.W. Lee and H. Thacker, Phys. Rev. **D16** (1977) 1519.
- [10] M. Veltman, Acta Phys. Polon. **B70** (1977) 475.
- [11] The LEP collaborations ALEPH, DELPHI, L3, OPAL and the LEP Higgs working group, *Search for the Standard Model Higgs boson at LEP*, hep-ex/0107029 and LHWG-Note-2001-03 (2001).
- [12] P. Abreu et al. (DELPHI collaboration), Phys. Lett. **B499** (2001) 23.
- [13] G. Abbiendi et al. (OPAL collaboration), Phys. Lett. **B499** (2001) 38.
- [14] R. Barate et al. (ALEPH collaboration), Phys. Lett. **B499** (2001) 53.
- [15] P. Achard et al. (L3 collaboration), Phys. Lett. **B517** (2001) 319.
- [16] The LEP collaborations ALEPH, DELPHI, L3, OPAL, the LEP Electroweak Working Group and the Heavy Flavor and Electroweak Groups, CERN-EP/99-15.
- [17] J. Wess and B. Zumino, Nucl. Phys. **B70** (1974) 39.
- [18] K. Lane, *Technicolor 2000*, hep-ph/0007304 (2000).
- [19] P.M. Dirac, Proc. Roy. Soc. Lon., **A133** (1931) 60.

- [20] The ATLAS Collaboration, *Inner Detector Technical Design Report*, CERN/LHCC 97-16 (Vol. I) and CERN/LHCC 97-17 (Vol. II).
- [21] The ATLAS Pixel Collaboration, *Pixel Detector Technical Design Report*, CERN/LHCC 98-13.
- [22] S. Haywood, *Offline alignment & calibration of the Inner Detector*, ATL-INDET-2000-005.
- [23] S. M. Sze, *Physics of semiconductor devices*, 2nd Edition, Wiley-interscience, New York (1981).
- [24] R. Wunstorf, IEEE Trans. on Nucl. Sci. **44** (1997) 806.
- [25] H. Feick, *Radiation tolerance of silicon particle detectors for high-energy physics experiments*, Ph.D. thesis University Hamburg, Internal Report DESY F35D-97-08 (1997).
- [26] G. Lindström, M. Moll and E. Fretwurst, Nucl. Instr. and Meth. **A426** (1999) 1.
- [27] E. Fretwurst et al., Nucl. Instr. and Meth. **A342** (1994) 119.
- [28] R. Wunstorf, *Systematische Untersuchungen zur Strahlenresistenz von Silizium-Detektoren für die Verwendung in Hochenergiephysik-Experimenten*, Ph.D. Thesis, Universität Hamburg, DESY-FH1K-92-01 (1992).
- [29] S. Bates et al., Nucl. Instr. and Meth. **A379** (1996) 116.
- [30] H. Feick et al., Nucl. Instr. and Meth. **A377** (1996) 217.
- [31] G. Lindström et al. (ROSE collaboration), *Radiation hard silicon detectors - developments by the RD48 (ROSE) collaboration*, Nucl. Instr. and Meth. **A466** (2001) 308.
- [32] M. Moll, *Radiation Damage in Silicon Particle Detectors Microscopic Defects and Macroscopic Properties*, Ph.D. Thesis, Hamburg University (1999) DESY-THESIS-1999-040, ISSN-1435-8085.
- [33] H. Feick, *Temperaturabhängigkeit der Langzeitausheilung neutronengeschädigter Silizium-Detektoren*, diploma thesis, Universität Hamburg (1993).
- [34] T. Schulz et al., IEEE Trans. on Nucl. Sci. **41** (1994) 791.
- [35] The ROSE collaboration, *RD48 3rd status report*, CERN/LHCC 2000-009 (2000).
- [36] A. Bishoff et al., Nucl. Instr. and Meth. **A326** (1993) 27.
- [37] G. Batignani et al., Nucl. Instr. and Meth. **A277** (1989) 147.
- [38] R.H. Richter et al., Nucl. Instr. and Meth. **A377** (1996) 412.
- [39] M. S. Alam et al., Nucl. Instr. and Meth. **A456** (2001) 217.
- [40] I. Gorelov et al., *Electrical characteristics of silicon pixel sensors*, ATL-COM-INDET-2001-015.
- [41] T. Rohe, Ph.D. thesis, Ludwig Maximilians Universität, Munich 1999.

- [42] M. Ackers et al., IEEE on Nucl. Sci. **46** (1999) 2033.
- [43] L. Blanquart et al., Nucl. Instr. and Meth. **A439** (2000) 403.
- [44] K. Einsweiler et al., IEEE Trans. on Nuclear Science **46** (1999) 166 and 792.
- [45] S. Stapnes and V. Tikhomirov, private communication.
- [46] H8 reconstruction package, developed by M. Aleppo and F. Ragusa, available from <http://troncon.home.cern.ch/troncon/testbeamhome.html>
- [47] E. Belau et al., Nucl. Instr. and Meth. **A214** (1983) 253.
- [48] <http://troncon.home.cern.ch/troncon/testbeamhome.html> , page maintained by C. Troncon.
- [49] C. Troncon, IEEE Trans. on Nucl. Sci. **47** (2000) 125.
- [50] F. Ragusa, Nucl. Instr. and Meth. **A447** (2000) 184.
- [51] W. Shockley, *Electrons and holes in semiconductors*, Van Nostrand, Princeton, N.J. (1950).
- [52] C. Jacoboni et al., Solid State Electronics **20** (1977) 77.
- [53] Landolt-Börnstein, *Semiconductors: Physics of group IV elements and III-V compounds*, Vol. III/17a of *Numerical data and functional relationships in science and technology*, Springer Verlag, Berlin (1982).
- [54] P. Blood and J. Worton, Rep. Prog. Phys. **41** (1978) 157.
- [55] V. Radeka, Ann. Rev. Nucl. Part. Sci. **38** (1988) 217.
- [56] R. Turchetta, Nucl. Instr. and Meth. **A335** (1993) 44.
- [57] R. Brun et al., *GEANT3*, CERN-DD/EE/84-1 (1987).
- [58] P. Billoir et al., Nucl. Instr. and Meth. **A241** (1985) 115.
- [59] R. Fruhwirth et al., Comp. Phys. Com. **96** (1996) 189.
- [60] R.K. Bock and M. Regler, *Data analysis techniques for high-energy physics experiments*, Cambridge University Press, Cambridge (1990).
- [61] T. Sjostrand, Comp. Phys. Com. **82** (1994) 74.

Acknowledgements

I would like to express my gratitude to all the members of the Milan ATLAS Pixel group, for their support of my work and the pleasant environment they have created for it. I am especially grateful to Francesco Ragusa and Clara Troncon for supervising this thesis and for their tireless assistance. I would like to remember also Chiara Meroni and Attilio Andreazza for their fruitful comments and help, Mario Aleppo for having shared his office with me and tolerated me for more than an year, Massimo Caccia for not having killed me when I have scratched a test sensor chip.

I also thank Alexander Rozanov, Jean-Baptiste Devivie and Dario Barberis for their help about the simulation software, and all the members of the ATLAS Pixel collaboration for stimulating discussions and ideas.